

# ALGEBRAIC FILTERS FOR FILTERED BACKPROJECTION

Proefschrift

ter verkrijging van  
de graad van Doctor aan de Universiteit Leiden,  
op gezag van Rector Magnificus prof.mr. C.J.J.M. Stolker,  
volgens besluit van het College voor Promoties  
te verdedigen op donderdag 13 april 2017  
klokke 13:45 uur

door

Linda Plantagie

geboren te Nieuwegein  
in 1986

Promotor: Prof. dr. Kees Joost Batenburg

Samenstelling van de promotiecommissie:

Voorzitter: Prof. dr. A. W. van der Vaart

Secretaris: Prof. dr. B. de Smit

Overige leden: Prof. dr. R. H. Bisseling (Universiteit Utrecht)  
Prof. dr. J. Sijbers (Universiteit Antwerpen)  
Dr. E. Van de Castele (AZ Monica, Antwerpen)

# **ALGEBRAIC FILTERS FOR FILTERED BACKPROJECTION**

ISBN: 978-94-6299-548-2

© Linda Plantagie, Leiden 2017

Cover design by Ridderprint BV, Ridderkerk  
Printed by Ridderprint BV, Ridderkerk

The research in this thesis has been financially supported by the Netherlands Organisation for Scientific Research (NWO), project 639.072.005.



---

# CONTENTS

---

<b>1</b>	<b>Introduction</b>	<b>1</b>
1.1	X-ray Transmission Computed Tomography . . . . .	1
1.2	FBP . . . . .	4
1.3	Algebraic reconstruction methods . . . . .	6
1.4	Preview . . . . .	8
<b>2</b>	<b>Fast Approximation of Algebraic Reconstruction Methods for Tomography</b>	<b>13</b>
2.1	Introduction . . . . .	14
2.2	The Filtered Backprojection algorithm . . . . .	16
2.3	Algebraic reconstruction algorithms . . . . .	19
2.4	Algebraic filters . . . . .	21
2.5	Experiments . . . . .	23
2.6	Results . . . . .	27
2.7	Conclusions . . . . .	42
<b>3</b>	<b>Spatial Variations in Reconstruction Methods for CT</b>	<b>47</b>
3.1	Introduction . . . . .	48
3.2	Method . . . . .	49
3.3	Experiments . . . . .	51
3.4	Results . . . . .	53
3.5	Discussion and Conclusions . . . . .	57
<b>4</b>	<b>Approximating Algebraic Tomography Methods by Filtered Backprojection: a Local Filter Approach</b>	<b>59</b>
4.1	Introduction . . . . .	60
4.2	Introduction to AF-FBP . . . . .	62
4.3	AF-FBP with multiple filters . . . . .	64
4.4	Experiments . . . . .	65
4.5	Results . . . . .	69
4.6	Discussion . . . . .	80
4.7	Conclusions . . . . .	81

---

<b>5 Algebraic Filter Approach for Fast Approximation of Non-linear Tomographic Reconstruction Methods</b>	<b>85</b>
5.1 Introduction . . . . .	86
5.2 Preliminaries . . . . .	89
5.3 Algebraic Filters for FBP . . . . .	94
5.4 Experiments . . . . .	97
5.5 Discussion and Conclusions . . . . .	109
<b>6 Filtered Backprojection using Algebraic Filters; Application to Biomedical Micro-CT Data</b>	<b>115</b>
6.1 Introduction . . . . .	116
6.2 The AF-FBP method . . . . .	118
6.3 Experiments . . . . .	119
6.4 Results . . . . .	121
6.5 Conclusions and discussion . . . . .	123
<b>7 The accuracy of FBP with recently introduced filters: a comparison</b>	<b>125</b>
7.1 Introduction . . . . .	125
7.2 Methods . . . . .	127
7.3 Experiments . . . . .	138
7.4 Results . . . . .	141
7.5 Discussion and Conclusions . . . . .	149
<b>Samenvatting</b>	<b>153</b>
<b>Curriculum Vitae</b>	<b>159</b>
<b>Acknowledgement</b>	<b>161</b>

---

## INTRODUCTION

---

### 1.1 X-RAY TRANSMISSION COMPUTED TOMOGRAPHY

Computed tomography is a technique that is used to reconstruct an object from a set of projections. It is applied in a broad range of fields, for example electron tomography, (bio)medical imaging, industrial imaging (such as quality inspection for materials science), and seismic tomography. The resolution depends upon the object to be scanned and can vary from nanometers to kilometers [1–5].

For X-ray transmission computed tomography, the projections are obtained by sending X-ray beams under varying angles through the object and measuring the intensity profile of the X-ray beam at a detector after it has traversed the object. The difference in intensity of the beam before and after intersecting the object, i.e. the *attenuation*, is used as input for various algorithms that can compute an image of the interior of the object. The attenuation of the beam is related to the type and thickness of the materials that lie on the ray paths between the X-ray source and the detector, and also on the energy of the X-ray photons that are used. This will be made more precise in the following.

We now consider a two-dimensional object, i.e. a slice. Let  $\mu(x, y, E)$  denote the attenuation coefficient of the material at position  $(x, y) \in \mathbb{R}^2$  for energy level  $E$ . Let  $L$  be a line from the source to the detector that is parameterized by  $L(l)$ , i.e., the variable  $l$  denotes the position on the line  $L$ . Let  $I_{\text{in}}(E)$  denote the intensity of the beam at energy  $E$  before it intersects with the object. The total intensity  $I$  of the beam at position  $l_1$  is then given by Eq. (1.1) [6].

$$I(l_1) = \int_0^{E_{\text{max}}} I_{\text{in}}(E) e^{-\int_0^{l_1} \mu(L(l), E) dl} dE, \quad (1.1)$$

where  $I_{\text{in}}(E)$  is the intensity of the incident beam.

In this work we mainly focus on monochromatic X-ray beams, i.e. beams with only one energy level  $E_0$ . In this case, there is a single attenuation for each position  $(x, y)$  in the object, which we denote by  $f(x, y) = \mu(x, y, E_0)$ . Then Eq. (1.1) simplifies to Eq. (1.2), which is known as the *Lambert-Beer law* [6, 7].

$$I(l_1) = I_{\text{in}} e^{-\int_0^{l_1} f(L(l)) dl}. \quad (1.2)$$

Let  $I_{\text{out}}$  be the intensity of the beam after traversing the object. We then define the *projection* of the object along the line  $L$  by Eq. (1.3).

$$p_L = -\ln\left(\frac{I_{\text{out}}}{I_{\text{in}}}\right) = \int_L f(L(l)) dl, \quad (1.3)$$

where  $\ln$  denotes the natural logarithm.

We conclude that by recording the intensities of both the attenuated beam and the unattenuated beam (without an object in the scanner), the integral of the attenuation along lines through the object can be obtained.

For a line  $L$  given in Eq. (1.4), the line integral along  $L$  is given by Eq. (1.5). This transform has been introduced by Johann Radon in 1917 [8] and is now known as the Radon transform [6, 9, 10].

$$L : x \cos \theta + y \sin \theta = t, \text{ for some } t \in \mathbb{R}, \quad (1.4)$$

$$(\mathcal{R}f)(\theta, t) = \int_{-\infty}^{\infty} f(t \cos \theta - s \sin \theta, t \sin \theta + s \cos \theta) ds, \quad (1.5)$$

for  $t \in \mathbb{R}$  and  $\theta \in [0, 2\pi)$ .

The Radon transform is of great importance in Computed Tomography. In 2D parallel beam scanning techniques, a detector is located opposite an X-ray source. In this work, we assume the detector is situated along a straight line perpendicular to a parallel beam of X-ray as shown in Fig. 1.1a. This figure also illustrates the concept of the line integrals for the Shepp-Logan phantom. The Shepp-Logan phantom is an image that consists of ellipses with different gray levels. It resembles a cross-section of a human head.

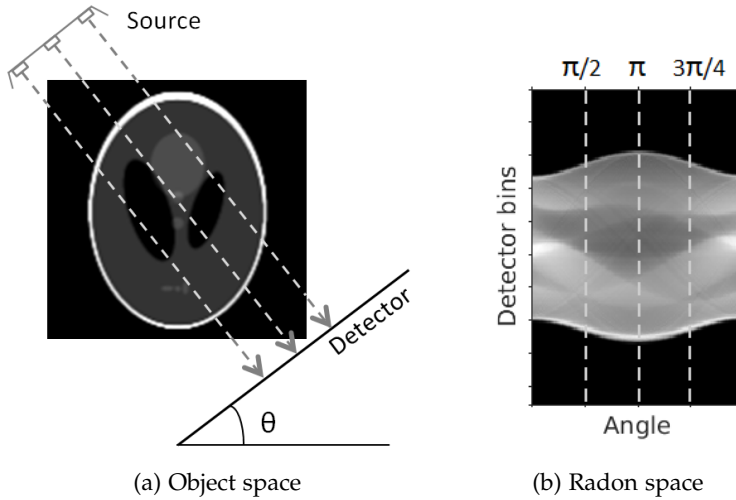


Figure 1.1: (a) 2D Parallel beam scanning geometry, (b) Projection data in Radon space.

The measured projection data can now be written as a set of line integrals depending on the projection angle  $\theta \in [0, \pi)$  and position  $t$  on the detector (see Eq. (1.6)).

$$p(\theta, t) = (\mathcal{R}f)(\theta, t). \quad (1.6)$$

The projection data for the phantom in Fig. 1.1a is shown in Fig. 1.1b. The gray level corresponds to the attenuation, where black refers to no attenuation and white to high attenuation.

There exist exact inversion formulas for the Radon Transform, such as the inverse Radon Transform [8] and the Fourier Slice theorem [6, 7, 9, 11]. However, these inversion formulas are based on the assumption that projections are available for all angles  $\theta$  and for all detector coordinates  $t$ . Since in practice only a finite set of projection angles  $\Theta$  can be measured for a finite set of detector bins  $T$ , such inversion formulas cannot be used directly as a reconstruction algorithm. Therefore, reconstruction methods have been developed that *approximate* the object. These methods can roughly be divided into two categories: *analytical* reconstruction methods and *algebraic* reconstruction methods (ARMs). A well-known reconstruction method in the analytical group is *Filtered*

*Backprojection* (FBP). We will now consider both FBP and the algebraic reconstruction methods in more detail.

## 1.2 FBP

An intuitive way to approximate the unknown function  $f$  is to take each element of the projection data and backproject it along its corresponding line through the object. Pixels that are contained in the support of the function  $f$  receive positive contributions from the corresponding backprojected lines for all projection angles. Pixels outside  $f$  receive in general only contributions for a smaller set of projection angles and their value in the reconstruction is less than that of pixels inside  $f$ . As attenuation coefficients are always positive values, the reconstruction of this backprojection method is a nonnegative image.

A major drawback of this method is that the reconstructed image is blurred and does not correctly invert the Radon transform. The Fourier Slice Theorem provides a more accurate inversion formula, which combines the backprojection operation with a *filtering* step [6, 7, 9, 11]. Let  $P(\theta, \nu) = \int_{-\infty}^{\infty} p(\theta, t)e^{-2\pi i\nu t} dt$ , the one-dimensional Fourier transform of  $p$ , taken separately for each angle  $\theta$ . According to the Fourier Slice Theorem, we can calculate  $f$  from  $P$  as shown in Eq. (1.7).

$$f(x, y) = \int_0^\pi \int_{-\infty}^{\infty} P(\theta, \nu) |\nu| e^{i2\pi\nu t} d\nu d\theta, \quad (1.7)$$

$$= \int_0^\pi q(\theta, t) dt, \quad (1.8)$$

where  $t = x \cos \theta + y \sin \theta$  and  $q(\theta, t) = \int_{-\infty}^{\infty} P(\theta, \nu) |\nu| e^{i2\pi\nu t} d\nu$ .

The term  $|\nu|$  is the important difference between the backprojection method described above and the formula in Eq. (1.7). The formula in Eq. (1.8) is a backprojection of the *filtered* projection data  $q$ , which is obtained by applying the so-called ramp-filter to the original projection data  $p$ . Note that for  $G(\theta, \nu) = |\nu|$  the function  $q$  is defined as  $q(\theta, t) = \int_{-\infty}^{\infty} P(\theta, \nu) G(\theta, \nu) e^{i2\pi\nu t} d\nu$ . If we denote the inverse Fourier transform of  $G(\theta, \cdot)$  by  $g(\theta, \cdot)$ , then Eq. (1.9) follows from the properties of the Fourier transform.

$$q(\theta, t) = \int_{-\infty}^{\infty} p(\theta, \tau) g(\theta, t - \tau) d\tau. \quad (1.9)$$

Hence  $q(\theta, \cdot)$  equals the convolution of  $p(\theta, \cdot)$  with the *filter*  $g(\theta, \cdot)$ .

Combining Eq. (1.8) and Eq. (1.9) and discretizing this formula results in Eq. (1.10), where  $\mathbf{u}(x, y)$  denotes the value of the reconstructed image at coordinate  $(x, y)$ . This formula is known as Filtered Backprojection.

$$\mathbf{u}(x, y) = \sum_{\theta \in \Theta} \sum_{t \in T} p(\theta, \tau) \tilde{g}(\theta, t - x \cos \theta - y \sin \theta), \quad (1.10)$$

where  $\tilde{g}(\theta, t) = \frac{\pi}{|\Theta|} g(\theta, t)$ .

Due to the limited number of projection data that can be measured, FBP can only compute an approximation of the unknown object  $f$ . The reconstruction quality of this approximation highly depends on the choice for the filter  $g$ . In 1971, Ramachandran and Lakshminarayanan have proposed to use a windowed filter for FBP [12]. We will refer to it as the Ram-Lak filter Eq. (1.11).

$$\text{(Ram - Lak)} \quad G(\theta, v) = |v| \text{rect}(v), \quad (1.11)$$

where  $\text{rect}(v)$  equals 1 for  $v \in [-\epsilon, \epsilon]$  for some  $\epsilon > 0$  and 0 otherwise. This windowed function reduces the effects of noise in the high frequency domain, which would otherwise be amplified due to the multiplication with  $|v|$ . To further reduce the effects of amplifying the high frequencies, other windowed filters have been proposed in literature. For example the Shepp-Logan filter, Hann filter, Cosine filter, and Hamming filter, see Eq. (1.12)-Eq. (1.15) respectively [6].

$$\text{(Shepp - Logan)} \quad G(\theta, v) = |v| \text{rect}(v) \text{sinc}(v), \quad (1.12)$$

$$\text{(Hann)} \quad G(\theta, v) = |v| \text{rect}(v) (0.5 - 0.5 \cos(2\pi v)), \quad (1.13)$$

$$\text{(Cosine)} \quad G(\theta, v) = |v| \text{rect}(v) \cos(\pi v), \quad (1.14)$$

$$\text{(Hamming)} \quad G(\theta, v) = |v| \text{rect}(v) (0.54 - 0.46 \cos(2\pi v)), \quad (1.15)$$

The main advantage of the Filtered Backprojection is its computational efficiency. It is also easy to implement and known for its high accuracy for low-noise projection data with a substantial number of equiangularly distributed projection angles. The reconstruction accuracy degrades in case of a limited angular range, few projection angles or a low signal-to-noise ratio. Fig. 1.2 contains reconstructions of

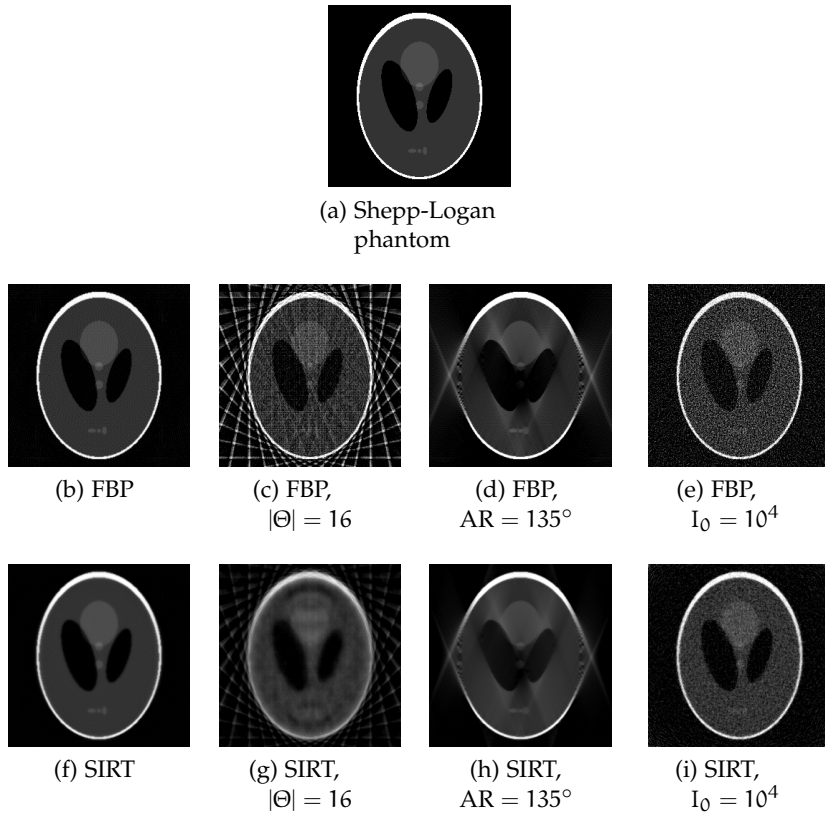


Figure 1.2: Reconstructions for SIRT with 100 iterations and FBP with the Ram-Lak filter; unless stated differently, the parameters are  $n = 255$ ,  $|\Theta| = 128$ , angular range ( $AR$ ) =  $180^\circ$  and noiseless projections.

the well-known Shepp-Logan phantom of both FBP and the algebraic reconstruction method SIRT (which will be discussed in Section 1.3) for varying parameters. The Shepp-Logan phantom consists of  $n \times n$  pixels. The variable  $I_0$  indicates the noise level. It represents the number of counts per detector element without an object.

### 1.3 ALGEBRAIC RECONSTRUCTION METHODS

Algebraic reconstruction methods offer an alternative approach to solving the reconstruction problem. Since the tomographic reconstruction problem can often not be solved exactly, the reconstruction problem



is discretized such that we obtain a system of linear equations. The unknown object is represented on a grid, which we here assume to be a square, consisting of  $n \times n$  pixels. The object is characterized by the vector  $\mathbf{x} \in \mathbb{R}^{n^2}$ , such that  $x_i$  corresponds to the density of the object on pixel  $i \in \{1, 2, \dots, n^2\}$ . The contribution of every image pixel to a line integral is given by the *projection matrix*  $\mathbf{W}$ . The number of rows of  $\mathbf{W}$  equals the number of projection angles  $|\Theta|$  multiplied by the number of detector bins  $|T|$ . Hence the discrete reconstruction problem can be written as Eq. (1.16).

$$\mathbf{W}\mathbf{x} = \mathbf{p}, \quad (1.16)$$

where  $\mathbf{p} \in \mathbb{R}^{N_{T\Theta}}$  is the projection data and  $N_{T\Theta} = |T||\Theta|$ .

The number of unknowns in this discrete reconstruction problem is typically very large and a solution cannot be calculated in reasonable time by explicit matrix inversion. Therefore, iterative algorithms have been proposed that solve for a least squares solution. Examples of such methods are ART/Kaczmarz method, SIRT and CGLS. We will now discuss SIRT in more detail.

The *Simultaneous Iterative Reconstruction Method* (SIRT) is an iterative linear reconstruction method. It updates the current solution based on the difference between the current forward projection and the measured projection data for all projection angles simultaneously. The  $k$ th iteration step of SIRT can be written as Eq. (1.17) [13, 14]. SIRT converges to a weighted least squares solution of the reconstruction problem.

$$\mathbf{u}^{(k+1)} = \mathbf{u}^{(k)} + \omega \mathbf{W}^T(\mathbf{p} - \mathbf{W}\mathbf{u}^{(k)}), \quad (1.17)$$

where  $\mathbf{u}^{(k)} \in \mathbb{R}^{n^2}$  is the resulting image of the  $k$ -th iteration and  $\omega \in \mathbb{R}$  is a relaxation parameter.

A disadvantage of many algebraic reconstruction methods including SIRT is that they require a long computation time. By parallelizing the computations of SIRT and using GPUs, the reconstruction time can be substantially reduced [15–17]. However, for large reconstruction problems the reconstruction time required for SIRT is still much larger than for FBP, which is an important disadvantage of this method. Advantages of SIRT are the possibility to incorporate prior knowledge, the robustness with respect to noise, and the higher accuracy compa-

red to FBP for limited-data problems and projection angles that are not equiangularly distributed. The bottom row of Fig. 1.2 contains reconstructions of SIRT for varying parameters.

#### 1.4 PREVIEW

Substantial research efforts have been made to improve the reconstruction accuracy of the computationally efficient FBP method. This can be done for example by various pre- and postprocessing steps, or by using different filters. We will focus in this work on the filtering step for two-dimensional reconstruction problems in X-ray computed tomography.

In Chapter 2 '*Fast Approximation of Algebraic Reconstruction Methods for Tomography*', we introduce a new algorithm to create filters for FBP which are based on a linear algebraic reconstruction method. This method is called *Algebraic filter-Filtered Backprojection* (AF-FBP). The filters that are created can be used in FBP in the same way as for example the Ram-Lak filter. The image characteristics of the reconstructions of AF-FBP are similar to those of the linear Algebraic Reconstruction Method (ARM) that was used to create the filters. The main benefit of this method is that, once the filters have been created, reconstructions are created with the computational efficiency of FBP, while the favorable reconstruction accuracy of the linear ARM is largely preserved.

By design, the reconstruction of an ARM does not only depend on the projection data, but also on the size and shape of the reconstruction grid. Also the position of the object within the reconstruction grid has an effect on the reconstruction. Both these effects and the discretization effects in FBP are examined in Chapter 3 '*Spatial Variations in Reconstruction Methods for CT*'.

The method AF-FBP uses by design a single pixel of the reconstruction grid for the creation of the filters. In the experiments in Chapter 2, the central pixel of the reconstruction grid is chosen for reasons that are explained there. As a consequence of the results in Chapter 3, choosing a different pixel will lead to different filters. We have therefore investigated the idea to use several pixels in the reconstruction grid to create multiple filters which can be applied to smaller areas of the reconstruction grid. The implementation and results for applying

these *local* filters is presented in Chapter 4 '*Approximating Algebraic Tomography Methods by Filtered Backprojection: a Local Filter Approach*'.

The AF-FBP algorithm presented in Chapter 2 is applicable for linear ARMs. It is not applicable for nonlinear ARMs such as the Conjugate Gradient Least Squares (CGLS) method or the Expectation Maximization (EM) method. Since also these methods are computationally inefficient compared to FBP, we would like to be able to approximate these methods with a fast algorithm that is similar to AF-FBP. In Chapter 5 '*Algebraic Filter Approach for Fast Approximation of Nonlinear Tomographic Reconstruction Methods*', the method AF-FBP is extended such that it can also be used for certain types of nonlinear algebraic reconstruction methods.

Computed tomography is used in various application fields, for example in industrial and (bio)medical imaging. In the experiments conducted in the previously announced chapters, the projection data were either simulated by computer models or obtained for industrial imaging applications. In biomedical imaging, bone structures and soft tissues with various gray levels are reconstructed. Especially for soft tissues, the difference in gray levels between neighboring tissues can be small and the boundaries can be highly irregular. In Chapter 6 '*Filtered Backprojection using Algebraic Filters; Application to Biomedical Micro-CT Data*', we compare reconstruction results of AF-FBP and FBP with a selection of standard filters for two experimentally obtained projection data sets of small animals.

We conclude this thesis with a comparison of several recently proposed methods to create and apply filters for FBP. The algorithms in Chapter 7 '*The accuracy of FBP with recently introduced filters: a comparison*' can all be applied to two-dimensional parallel beam geometries. We provide a short description of these methods and give an overview of their characteristics including the computational efficiency. We also comment on the reconstruction quality based on experimental results.

## BIBLIOGRAPHY

- [1] S. Van Aert et al. Three-dimensional atomic imaging of crystalline nanoparticles. *Nature* 2011; 470(7334): 374–377.
- [2] H. Sipila. Moving object computer-tomography for luggage inspection. *Applications of Signal and Image Processing in Explosives Detection Systems*. Ed. by M. C. Connelly and S. M. Cheung. Proc. SPIE, 1993; 1824: 39–40.
- [3] P. Targowski et al. The Application of Optical Coherence Tomography to Non-Destructive Examination of Museum Objects. *Studies in Conservation* 2004; 49(2): 107–114.
- [4] M. Defrise and G. T. Gullberg. Image reconstruction. *Phys. Med. Biol.* 2006; 51(13): 139–154.
- [5] W. A. Kalender. X-ray computed tomography. *Phys. Med. Biol.* 2006; 51(13): 29–43.
- [6] T. M. Buzug. *Computed Tomography: From Photon Statistics to Modern Cone-Beam CT*. Berlin: Springer, 2008.
- [7] A. Markoe. *Analytic Tomography*. New York: Cambridge University Press, 2006.
- [8] J. Radon. Über die Bestimmung von Funktionen durch ihre Integralwerte längs gewisser Mannigfaltigkeiten. *Berichte Sächsische Akademie der Wissenschaften* 1917; 69: 262–277.
- [9] F. Natterer. *Mathematical methods in image reconstruction*. Philadelphia: SIAM, 2001.
- [10] A. C. Kak and M. Slaney. *Principles of Computerized Tomographic Imaging*. Philadelphia: SIAM, 2001.
- [11] G. T. Herman and A. Kuba, eds. *Discrete Tomography: Foundations, Algorithms and Applications*. Birkhäuser, Boston, 1999.
- [12] G. N. Ramachandran and A. V. Lakshminarayanan. Three-dimensional Reconstruction from Radiographs and Electron Micrographs: Application of Convolutions instead of Fourier Transforms. *Proc. Nat. Acad. Sci. USA* 1971; 68(9): 2236–2240.
- [13] G. T. Herman. *Fundamentals of Computerized Tomography: Image Reconstruction from Projections*. Berlin: Springer, 2009.

- [14] A. van der Sluis and H. A. van der Vorst. SIRT- and CG-type methods for the iterative solution of sparse linear least-squares problems. *Linear Algebra and its Applications* 1990; 130: 257–302.
- [15] D. Castano-Diez, H. Mueller, and A.S. Frangakis. Implementation and performance evaluation of reconstruction algorithms on graphics processors. *Journal of Structural Biology* 2007; 157(1): 288–295.
- [16] F. Xu and K. Mueller. Accelerating Popular Tomographic Reconstruction Algorithms On Commodity PC Graphics Hardware. *IEEE Trans. Nucl. Science* 2005; 52(3): 654–663.
- [17] W.J. Palenstijn, K.J. Batenburg, and J. Sijbers. Performance improvements for iterative electron tomography reconstruction using graphics processing units (GPUs). *J. Struct. Biol.* 2011; 176(2): 250–253.



---

## FAST APPROXIMATION OF ALGEBRAIC RECONSTRUCTION METHODS FOR TOMOGRAPHY

---

**Abstract** – Most reconstruction algorithms for transmission tomography can be subdivided in two classes: variants of Filtered Back-projection (FBP) and iterative algebraic methods. FBP is very fast and yields accurate results when a large number of projections are available, with high signal-to-noise ratio and a full angular range. Algebraic methods require much more computation time, yet they are more flexible in dealing with limited data problems and noise. In this chapter we propose an algorithm that combines the best of these two approaches: for a given linear algebraic method, a filter is computed that can be used within the FBP algorithm. The FBP reconstructions that result from using this filter strongly resemble the algebraic reconstructions and have many of their favorable properties, while the required reconstruction time is similar to standard-FBP. Based on a series of experiments, for both simulation data and experimental data, we demonstrate the merits of the proposed algorithm.

## 2.1 INTRODUCTION

Transmission tomography is a mature imaging technique, for which both the engineering aspects of image acquisition and the mathematical and computational aspects of image reconstruction are well understood [1–4]. Although tomography is nowadays often used as an off-the-shelf technique, it is important to realize that the resulting image depends quite strongly on the employed reconstruction algorithm. When comparing reconstruction methods, various aspects must be balanced, such as the quality of the reconstructed image, the required reconstruction time, and robustness to noise.

During the past decades, reconstruction algorithms for transmission tomography have been developed among different chains [5]. The derivation of *analytical algorithms* departs from an idealized continuous representation of the image reconstruction problem, for which analytical solutions can be obtained. The resulting inversion formulas are then discretized and transformed into a reconstruction algorithm. On the other hand, *algebraic algorithms* depart from a discretized model of the tomographic imaging setup, which is represented by a system of linear equations. Although a least-squares solution of this system could in principle be calculated directly, this is impractical due to the enormous size of the corresponding matrix. Instead, iterative methods are used, as they can deal effectively with such large sparse systems.

The *Filtered Backprojection* algorithm (FBP) is among the most popular analytical reconstruction methods. It is capable of computing accurate reconstructions with high computational efficiency, provided that high quality projections have been acquired for a sufficiently large number of angles, distributed evenly between  $0^\circ$  and  $180^\circ$ . For this reason, variants of FBP have dominated clinical CT practice for many years. In particular, the related Feldkamp, Davis, and Kress (FDK) algorithm for cone-beam reconstruction [6] has demonstrated the ability to combine fully 3-D image acquisition with accurate and efficient reconstruction.

The limitations of FBP become apparent when only a small number of projection images can be acquired, when the angular range of the projections is limited or irregular, or when the measured data is noisy. In such cases, the reconstruction quality of FBP degrades and artefacts hamper subsequent image processing tasks, such as segmentation.



Compared to FBP, iterative algebraic methods have several key advantages: 1) limited data problems (i.e., small number of projection angles, limited angular range) can be modeled accurately by adjusting the system of equations, whereas in FBP the underlying analytical model is based on the assumption of having projections available from all angles; 2) noise in the projections can be effectively averaged, by seeking a least-squares solution of the equation system; 3) certain types of prior knowledge, such as nonnegativity of the attenuation coefficients, can be incorporated in the reconstruction algorithm; and 4) physical properties of the imaging system, such as a spatially varying point-spread function can be modeled by adjusting the system of equations.

Although the analytical (continuous) formula that is the basis of the FBP algorithm is exact, interpolation errors are introduced if the assumptions made in this formula (an infinite number of projections must be available across a full angular range) are not satisfied. Therefore, the discretized version of the formula does not yield an exact solution of the reconstruction problem, not even if the projection data is noiseless. In contrast, iterative methods minimize the residual projection error by departing from a discretized model that only incorporates the data that is really available.

Despite these advantages, the high computational cost of iterative methods, which can easily be one or two orders of magnitude larger than the computational load of FBP, is a major obstacle toward widespread practical use of such algorithms. The reconstruction time for iterative algebraic methods can be strongly reduced by parallelizing the computations, in particular when combined with the massive parallelism of modern graphic processing units (GPUs) [7, 8]. Still, the reconstruction of large volumes by iterative methods takes a long time when compared with FBP, which can be accelerated similarly by parallel computation.

Connections between algebraic and analytical reconstruction methods have been explored by several authors. In [9], it was shown that a least-squares matrix formulation of the discretized FBP operator provides a connection between the analytic and algebraic reconstruction approach. Any linear, shift invariant reconstruction algorithm is equivalent to FBP with a particular filter, which was demonstrated in [10]. In [11], a formula was derived for a filter kernel that can be used to express the image quality of SIRT.

In this chapter, we propose an actual reconstruction *algorithm* that combines the favorable properties of iterative algebraic methods with the computational advantages of FBP: for a given linear algebraic method, an angle-dependent filter is computed that can be used within the FBP algorithm. The FBP reconstructions that result from using this filter strongly resemble the algebraic reconstructions, while the required reconstruction time is similar to that of standard-FBP. In particular, for one selected image pixel, the reconstruction result of the algebraic method is identical to the result of applying FBP with the proposed filter, independently of the projection data.

The filter computation has a high computational cost, which is much larger than the cost of reconstructing a single image by an algebraic method. However, as long as the imaging geometry (i.e., projection angles, detector size, etc.) is fixed, the same filter can be used for all subsequent reconstructions, as the filter does not depend in any way on the scanned object. In the vast majority of commercial CT-scanners, only a few different acquisition schemes are used for a particular scanner. The filters for these schemes can be computed once, using a separate computer system, or even a large cluster. Subsequently, reconstructions can be computed from an arbitrary number of tomography datasets at the same speed as standard-FBP. The computed filters can be directly incorporated in existing FBP implementations.

This chapter is structured as follows. In Section 2.2, we briefly revisit the analytical model behind the FBP algorithm and its discretization. Section 2.3 introduces a general model for linear algebraic reconstruction algorithms. The key contribution of this article is made in Section 2.4, where an expression is derived for *algebraic filters* (AFs): filters for the FBP algorithm that are extracted from a linear algebraic method. We also discuss how such filters can be computed. In Section 2.5, we describe a set of experiments that have been performed to compare the reconstruction quality of our approach with alternative reconstruction algorithms. The results of these experiments are presented in Section 2.6. Section 2.7 concludes this chapter.

## 2.2 THE FILTERED BACKPROJECTION ALGORITHM

In this chapter, we focus on a *parallel beam* scanning geometry, using a single rotation axis. For several other scanning geometries, including

the fan-beam geometry and the circular cone-beam geometry with small cone angle, the approach presented here can also be applied, after rebinning of the projection data.

We start by revisiting the Radon transform and its analytical inversion. Let  $f : \mathbb{R}^2 \rightarrow \mathbb{R}$  be a finite and integrable function with bounded support for which the Radon transform

$$\begin{aligned} p(\theta, t) &= (\mathcal{R}f)(\theta, t) \\ &= \int_{-\infty}^{\infty} f(t \cos \theta - s \sin \theta, t \sin \theta + s \cos \theta) ds \end{aligned} \quad (2.1)$$

is defined almost everywhere in  $\theta \in [0, \pi)$ ,  $t \in \mathbb{R}$ . We refer to [12] for details on the analytical properties of the Radon transform. The variables  $\theta$  and  $t$  denote the angle with the vertical axis and the signed distance between the projected line and the origin of the coordinate system, respectively. We refer to  $p(\theta, \cdot)$  as the *projection* of  $f$  for angle  $\theta$ . For  $\theta \in [0, \pi)$ , define  $P(\theta, u) = \int_{-\infty}^{\infty} p(\theta, t) e^{-2\pi i u t} dt$  and  $q(\theta, t) = \int_{-\infty}^{\infty} P(\theta, u) G(\theta, u) e^{2\pi i u t} du$ , where  $G$  represents a *filter*. Thus,  $q(\theta, \cdot)$  is obtained from  $p(\theta, \cdot)$  by applying the filter  $G(\theta, \cdot)$  in the Fourier domain. Alternatively, the filtering of the projection data can be formulated as a convolution in real space as  $q(\theta, t) = \int_{-\infty}^{\infty} p(\theta, \tau) g(\theta, t - \tau) d\tau$ , where  $g(\theta, \cdot)$  denotes the inverse Fourier Transform of  $G(\theta, \cdot)$ .

For the choice  $G(\theta, u) = |u|$ , known as the *Ramp filter*, the filtered projections can be used to obtain an exact inversion formula for the Radon transform

$$f(x, y) = \int_0^{\pi} q(\theta, x \cos \theta + y \sin \theta) d\theta. \quad (2.2)$$

In practice, the function  $p(\theta, t)$  can only be measured for a finite set  $\Theta = \{\theta_1, \dots, \theta_d\}$  of projection angles, and at a finite set  $T = \{t_1, \dots, t_\ell\}$  of *detector positions*. Algorithms that require evaluation of  $p(\theta, t)$  at other detector positions, such as the FBP algorithm, typically employ some form of interpolation to approximate these projection values. For the sake of clarity, we will assume that  $T = \{-R, -R + 1, \dots, R - 1, R\}$  with  $R$  a positive integer, which corresponds to an array of  $2R + 1$  contiguous detectors with unit spacing, centered around  $t = 0$ .

The Filtered Backprojection algorithm is obtained by discretizing Eq. (2.2)

$$\begin{aligned}
 f(x, y) &\approx \frac{\pi}{d} \sum_{\theta \in \Theta} \int_{-\infty}^{\infty} p(\theta, \tau) g(\theta, x \cos \theta + y \sin \theta - \tau) d\tau \\
 &\approx \frac{\pi}{d} \sum_{\theta \in \Theta} \sum_{\tau \in T} p(\theta, \tau) g(\theta, x \cos \theta + y \sin \theta - \tau) \\
 &= \sum_{\theta \in \Theta} \sum_{\tau \in T} p(\theta, \tau) \tilde{g}(\theta, \tau - x \cos \theta - y \sin \theta), \quad (2.3)
 \end{aligned}$$

where  $\tilde{g}(\theta, t) = (\pi/d)g(\theta, -t)$ .

Various discrete approximations of the ideal Ramp filter  $G(\theta, u) = |u|$  are used in practice. The Ram-Lak filter, for example, is a windowed Ramp-filter (see Fig. 2.1). Although the Ram-Lak filter can result in accurate reconstructions if high quality projection data are available, its amplification of high frequencies results in low reconstruction quality for noisy data. This effect can be reduced by applying a smooth window-function to the original filter. Several common filters, such as the Shepp-Logan and Cosine filter, are based on this principle. Still, their design is intrinsically heuristic, aimed at optimizing the visual quality of the reconstructed image.

Instead of designing filters in the Fourier domain as described above, the filters can also be designed in the spatial domain (i.e., the *detector* domain). In [13], new filters are created based on approximations of the Ramp filter in the spatial domain. In [14], the method of approximate inverse is applied to obtain filters in the spatial domain that are not derived from the Ramp filter. In [15] and [16], a method is described to create filters for tomosynthesis based on iterative reconstructions of certain test objects.

The effect of applying a particular filter to the projection data can be studied both in the Fourier domain and in the spatial domain, by considering the functions  $G$  and  $g$ , respectively. In this chapter, we mainly focus on the spatial domain, where the filter operation can be interpreted according to Eq. (2.3) as follows: the value of the reconstructed image at point  $(x, y)$  is formed by taking the dot-product of the discretized projection data with a *weight vector* that is formed by evaluating the function  $\tilde{g}$  at consecutive discrete detector points. Therefore, the filter  $\tilde{g}$  determines the weight of the contribution of each detector position to the reconstructed value.

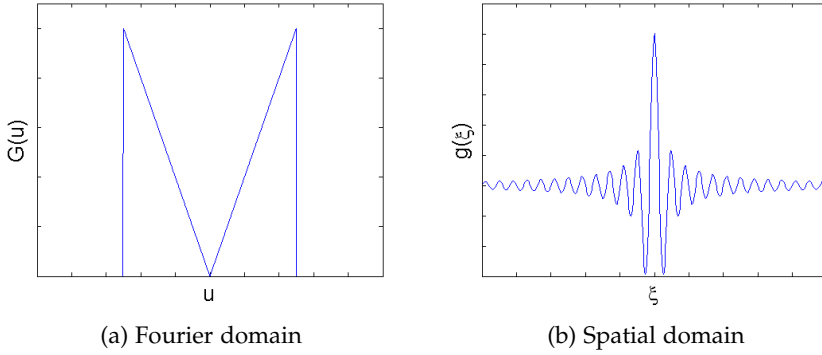


Figure 2.1: Filter formed by multiplying  $G(\theta, u) = |u|$  with a window function.

### 2.3 ALGEBRAIC RECONSTRUCTION ALGORITHMS

In *algebraic* reconstruction algorithms, the reconstruction problem is represented by a system of linear equations. The reconstructed image is represented on a grid consisting of  $n$  pixels. Let  $\mathbf{p} = (p_i) \in \mathbb{R}^m$  denote the measured data elements for all projections, collapsed into a single vector, where  $m = d\ell$ . Every entry  $p_i$  ( $i = 1, \dots, m$ ) corresponds to a pair  $(\theta, t) \in \Theta \times T$ , denoting the angle and detector position for that particular measurement. As an alternative notation, we refer to this entry as  $p_{\theta t}$ .

In the case of noiseless projection data, the projection process in tomography can be modeled as a finite linear transformation  $\mathbf{W}$  that maps the image  $\mathbf{v} = (v_i) \in \mathbb{R}^n$  (representing the object) to the vector  $\mathbf{p}$  of measured data

$$\mathbf{W}\mathbf{v} = \mathbf{p}. \quad (2.4)$$

The  $m \times n$  matrix  $\mathbf{W} = (w_{ij})$  is called the *projection matrix* and the product  $\mathbf{W}\mathbf{v}$  is referred to as the *forward projection* of  $\mathbf{v}$ . The entries of  $\mathbf{v}$  correspond to the pixel values of the reconstruction. The entry  $w_{ij}$  determines the weight of the contribution of pixel  $j$  to measurement  $i$ , which usually represents the length of the intersection between the pixel and the projected line.

Several algebraic reconstruction algorithms, including the well-known ART, SART and SIRT algorithms [2], belong to the class of *linear reconstruction methods*. This means that their application to given projection data  $\mathbf{p} \in \mathbb{R}^m$ , yielding a reconstructed image  $\mathbf{u} \in \mathbb{R}^n$ , can be modeled as a linear transformation  $S : \mathbb{R}^m \rightarrow \mathbb{R}^n$ . We identify this transformation with the corresponding matrix  $\mathbf{S} \in \mathbb{R}^{n \times m}$ , called the *reconstruction matrix*, yielding the following expression describing the input-output relation of the reconstruction algorithm

$$\mathbf{u} = \mathbf{S}\mathbf{p}. \quad (2.5)$$

**Example 1.** For given projection data  $\mathbf{p}$ , one can apply a range of SIRT-like reconstruction algorithms to obtain a solution of Eq. (2.4). Taking  $\mathbf{u}^{(0)} = \mathbf{0}$  as the start solution and denoting the reconstruction after  $k$  iterations by  $\mathbf{u}^{(k)}$ , the iteration step of this family of algorithms can be described by

$$\mathbf{u}^{(k+1)} = (\mathbf{I}_n - \omega \mathbf{C}\mathbf{W}^T \mathbf{R}\mathbf{W})\mathbf{u}^{(k)} + \omega \mathbf{C}\mathbf{W}^T \mathbf{R}\mathbf{p}, \quad (2.6)$$

where  $\mathbf{C} = (c_{ij}) \in \mathbb{R}^{n \times n}$  is a diagonal matrix such that  $c_{jj} = \alpha(\sum_{i=1}^n |w_{ij}|)$  for a certain scalar function  $\alpha$ ,  $\mathbf{R} = (r_{ij}) \in \mathbb{R}^{m \times m}$  is a diagonal matrix such that  $r_{ii} = \beta(\sum_{j=1}^m |w_{ij}|)$  for a certain scalar function  $\beta$ ,  $\mathbf{I}_n \in \mathbb{R}^{n \times n}$  denotes the identity matrix, and  $\omega$  is a relaxation parameter [17].

Let  $\mathbf{M} \in \mathbb{R}^{(m+n) \times (m+n)}$  be the *iteration-matrix* given by

$$\mathbf{M} = \begin{pmatrix} (\mathbf{I}_n - \omega \mathbf{C}\mathbf{W}^T \mathbf{R}\mathbf{W}) & \omega \mathbf{C}\mathbf{W}^T \mathbf{R} \\ \emptyset & \mathbf{I}_m \end{pmatrix}, \quad (2.7)$$

and define

$$\mathbf{S}_K = \begin{pmatrix} \mathbf{I}_n & \emptyset \end{pmatrix} \mathbf{M}^K \begin{pmatrix} \emptyset \\ \mathbf{I}_m \end{pmatrix}. \quad (2.8)$$

Then choosing  $\mathbf{S} := \mathbf{S}_K$  gives the reconstruction matrix corresponding to  $K$  iterations of the SIRT algorithm.

## 2.4 ALGEBRAIC FILTERS

In this section, we will demonstrate how the reconstruction of a single pixel by a linear algebraic method can be interpreted as reconstruction of that same pixel by FBP, using a particular filter that is determined by the reconstruction matrix of the algebraic method. By using this filter within FBP to reconstruct the *entire* image, a reconstruction algorithm is obtained, which yields reconstructed images that are very similar to the results of the algebraic method.

Let  $\mathbf{S}$  be a reconstruction matrix for a certain linear algebraic method  $S$ . We will now focus on a single pixel  $c \in \{1, \dots, n\}$  of the reconstructed image. Let  $(x_c, y_c) \in \mathbb{R} \times \mathbb{R}$  denote the coordinates of the center of this pixel.

Denote the  $c$ th row of  $\mathbf{S}$  by  $\mathbf{s}^{(c)}$ . Each entry of  $\mathbf{s}^{(c)}$  corresponds to an entry in the right hand side of Eq. (2.5), and therefore to a pair  $(\theta, \tau) \in \Theta \times T$ , which we denote by  $s_{\theta\tau}^{(c)}$ . Substituting this notation in Eq. (2.5) yields

$$u_c = \sum_{\theta \in \Theta} \sum_{\tau \in T} p_{\theta\tau} s_{\theta\tau}^{(c)}. \quad (2.9)$$

For  $\theta \in \Theta$ , put  $t_c^{(\theta)} = x_c \cos \theta + y_c \sin \theta$ . We now introduce a function  $h^{(c)}$ , which is defined for  $\tau \in T - t_c^{(\theta)}$ , where the minus sign denotes element-wise subtraction

$$h^{(c)}(\theta, \tau) = s_{\theta(\tau+t_c^{(\theta)})}^{(c)}. \quad (2.10)$$

Substituting Eq. (2.10) into Eq. (2.9) yields

$$u_c = \sum_{\theta \in \Theta} \sum_{\tau \in T} p_{\theta\tau} h^{(c)}(\theta, \tau - x_c \cos \theta - y_c \sin \theta). \quad (2.11)$$

All required evaluations of  $h^{(c)}$  in this expression are defined according to Eq. (2.10). Comparing Eqs. (2.3) and (2.11), we see that for the selected pixel  $c$ , the result of applying the linear algebraic method  $S$  is equivalent to applying the FBP algorithm with the angle-dependent filter  $\tilde{g} = h^{(c)}$ . We refer to such a filter as an *algebraic filter* (AF).

Just as in FBP, the AF determines the weight of the contribution of each detector position to the reconstructed value. This brings up the

question if, similar to FBP, the same filter  $h^{(c)}$  can also be used to reconstruct pixels other than  $c$ . Note that as  $h^{(c)}(\theta, \tau)$  is only defined for  $\tau \in T - t_c^{(\theta)}$ , this will require the domain of  $h^{(c)}(\theta, \cdot)$  to be extended by interpolation.

One may expect that at least for pixels  $j$  that are near  $c$ , we have

$$u_j \approx \sum_{\theta \in \Theta} \sum_{\tau \in T} p_{\theta\tau} h^{(c)}(\theta, \tau - x_j \cos \theta - y_j \sin \theta). \quad (2.12)$$

This approximation can be interpreted as follows: suppose that both the reconstruction region and the detector (for all angles) are shifted such that their relative position with respect to pixel  $j$  is the same as the relative position of the original geometry with respect to pixel  $c$ . Then Eq. (2.12) is an exact equality.

We point out that the filter  $h^{(c)}$  depends on the particular pixel  $c$ , and may vary throughout the image domain, which may offer an advantage for the algebraic method compared to the approximation given in Eq. (2.12), based on a single filter. In particular, algebraic methods have the capability (by their very definition) to confine all the intensity of the object within the reconstruction grid, which cannot be accomplished by FBP methods. Still, as will be demonstrated in Section 2.5, even a single filter can already approximate the reconstruction properties of the underlying algebraic method quite accurately.

To compute the AF for a given linear algebraic method  $S$  for a particular pixel  $c$ , the  $c$ th row of the reconstruction matrix  $S$  must be computed, which comes down to determining the impulse response of pixel  $c$  for all detector positions. Let  $e_{\theta\tau} \in \mathbb{R}^m$  denote the unit vector which has a value of 1 for the entry corresponding to  $(\theta, \tau)$ . Then  $s_{\theta\tau}^{(c)}$  is given by

$$s_{\theta\tau}^{(c)} = [S(e_{\theta\tau})]_c. \quad (2.13)$$

Therefore, the method  $S$  must be applied separately for each  $(\theta, \tau) \in \Theta \times T$  to compute all filter coefficients  $s_{\theta\tau}^{(c)}$ .

In the experiments that will be presented in the next section, we will focus on the AF for the *central pixel* of the reconstruction grid, i.e., a



pixel centered at the origin. For this pixel  $c$ , we have  $t_{\theta}^{(c)} = 0$  for all  $\theta$  and therefore

$$h^{(c)}(\theta, \tau) = s_{\theta\tau}^{(c)} \quad \text{for all } \theta \in \Theta, \tau \in T. \quad (2.14)$$

To use this filter for projection angle  $\theta$  in an FBP implementation, the discrete representation of  $h^{(c)}(\theta, \cdot)$  must first be zero-padded, after which the Discrete Fourier Transform is applied. The resulting filter in the Fourier domain  $H^{(c)}(\theta, \cdot)$  can then be applied to the Fourier representation of the projection data in exactly the same way as the Ramp filter, or other common filters. Note that the AF is different for each projection angle, while most common filters do not depend on the angle. This property does not have a significant impact on the running time of the filtering operation.

When computing the AF for a single pixel  $c$ , the required (sequential) computation time is  $mV$ , where  $V$  is the computation time of a single run of the algebraic method. For large image sizes, with many projections, the computational cost of computing a single filter can be substantial and several orders of magnitude larger than the cost of computing a single algebraic reconstruction. However, the resulting filter does not depend in any way on the scanned object. If the geometrical parameters (projection angles, detector size and position) of the scanning device are fixed, the same filter can be used for reconstructing an arbitrarily large number of datasets. In the vast majority of commercial CT-scanners, only a few different acquisition schemes are used for a particular scanner. The filters for these schemes can be computed once, using a separate computer system, or even a large cluster. Subsequently, reconstructions can be computed at the same speed as standard-FBP.

## 2.5 EXPERIMENTS

A set of experiments has been performed to compare the accuracy of reconstructions computed by AF-FBP, using an algebraic filter based on the iterative SIRT algorithm, with FBP using a standard filter and with SIRT. Note that no priors are used for the SIRT reconstructions or for the derivation of the SIRT-based filters. In this section we will describe the setup of the experiments.

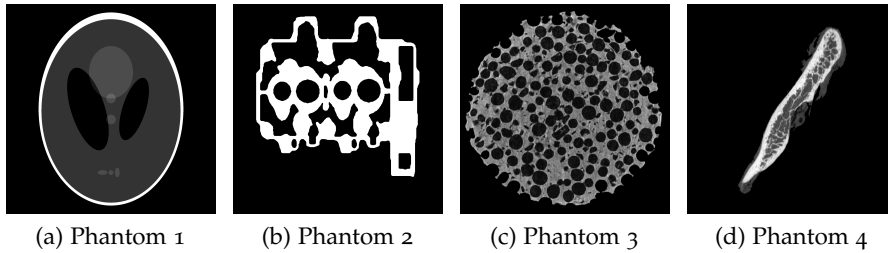


Figure 2.2: Phantom images of size  $2044 \times 2044$  used for the experiments.

### 2.5.1 General Design of the Experiments

Four phantom images have been used for the experiments; see Fig. 2.2. The first phantom is the well-known Shepp-Logan phantom. Phantom 2 represents a cross-section of a cylinder head in a combustion engine. Phantom 3 represents a metal foam, and Phantom 4 is a part of a human mandible. Phantoms 3 and 4 are slightly adjusted reconstructions of experimental  $\mu$ CT data sets. The size of all phantoms is  $2044 \times 2044$  pixels. Note that the phantom size is a multiple of four. In fact, the reconstructions are computed using a pixel size that is four times as large as the phantom pixel size, in both directions. The features of the phantoms are not aligned with the coarse reconstruction grid, such that partial volume effects can be observed in the reconstructions. The detector consists of 511 bins, each having a width of four image pixels. The size of the detector therefore equals the width of the phantom images. Parallel beam projections are simulated using a ray-driven projector based on the Joseph kernel to determine the contribution of an image pixel to each ray [18]. Per detector bin four rays are traced, thereby ensuring that each image pixel participates with strictly positive weight. Unless stated otherwise, the projection angles of the parallel beam projections are regularly distributed between  $0^\circ$  and  $180^\circ$ . The number of projection angles, denoted by  $d$ , may vary during the experiments.

### 2.5.2 Quantitative Evaluation of the Reconstruction Algorithms

The four phantoms are reconstructed using three different reconstruction algorithms. Several series of experiments are performed

to examine the relative reconstruction accuracy of different reconstruction algorithms. The following three reconstruction methods are compared.

1. FBP-RL: FBP with the standard Ram-Lak filter; see Section 2.2.
2. SIRT: The reconstruction method described by Eq. (2.6), with  $\omega = 1$ ,  $K = 200$ , and  $\alpha(\cdot)$  and  $\beta(\cdot)$  given by  $\alpha(x) = \beta(x) = 1/x$  for  $x \in \mathbb{R}$ . It converges to a weighted least-squares solution of the system  $\mathbf{W}\mathbf{v} = \mathbf{p}$  of minimal norm. We used the version of SIRT that is described in [17].
3. SIRT-FBP: Filtered Backprojection with an angle-dependent algebraic filter based on SIRT. For every projection angle, the filter coefficients for the central pixel are obtained using Eq. (2.13), where the reconstruction algorithm S corresponds with 200 SIRT iterations.

A square reconstruction grid of  $z \times z$  pixels is used during the experiments, where each pixel has the same width and height as a detector bin. Preliminary experiments have shown that in some cases the reconstruction accuracy of SIRT-FBP improves if the filters are created using a reconstruction grid with a size  $z$  that is larger than the number of bins of the detector. We denote the number of detector bins by  $z_0$ .

The quality of the reconstructed images is computed in the image domain by comparing the reconstruction with the phantom image, and in the projection domain by comparing the projections of the reconstructed image with the projections of the phantom. For a reconstruction  $\mathbf{u} \in \mathbb{R}^{z^2}$  of size  $z \times z$  (with  $z \geq z_0$ ), let  $\tilde{\mathbf{u}} \in \mathbb{R}^{z_0^2}$  denote the subimage of  $\mathbf{u}$  of size  $z_0 \times z_0$  with the same central pixel as  $\mathbf{u}$ . Furthermore, let  $\hat{\mathbf{u}}$  be a high resolution version of  $\tilde{\mathbf{u}}$ , obtained by replacing every pixel in  $\tilde{\mathbf{u}}$  by  $4 \times 4$  small pixels with the same intensity. Note that the image  $\hat{\mathbf{u}} = (\hat{u}_{ij})$  has the same pixel resolution as the phantom image  $\mathbf{v} = (v_{ij})$ . Define the *mean reconstruction error*  $E_r$  by

$$E_r = \frac{\sum_{i,j} |\hat{u}_{ij} - v_{ij}|}{\sum_{i,j} v_{ij}}. \quad (2.15)$$

Denote the forward projection of  $\mathbf{u}$  by  $\mathbf{q} = (q_{\theta t})$ . Then the *mean projection error*  $E_p$  is defined by

$$E_p = \frac{\sum_{\theta \in \Theta} \sum_{t \in T} |q_{\theta t} - p_{\theta t}|}{\sum_{\theta \in \Theta} \sum_{t \in T} p_{\theta t}}. \quad (2.16)$$

When comparing FBP-RL with SIRT and SIRT-FBP, the FBP-RL and SIRT-FBP reconstruction are always computed on a grid of size  $z_0 \times z_0$ , whereas the grid size  $z \times z$  for SIRT can vary. When computing the projection error, the full  $z \times z$  reconstruction is used to determine the forward projection of the SIRT reconstructions.

In the first series of experiments, the effect of the size of the reconstruction grid on the reconstruction accuracy of the algorithms is examined. In the second series of experiments the size of the reconstruction grid is kept fixed and the accuracy of the reconstructions from the three methods is examined as a function of the number of projection angles  $d$ , where the angles are regularly distributed between  $0^\circ$  and  $180^\circ$ .

In certain tomography applications, notably electron tomography, the angular range of the projections is limited. Contrary to standard FBP, algebraic methods can easily be adapted to such limited-angle geometries by adjusting the projection matrix. In the third series of experiments, the dependence of the reconstruction accuracy on the angular range is examined for the three methods. In these experiments, the step between consecutive angles is kept fixed at  $0.5^\circ$  and an angular range of  $180^\circ$  corresponds to full angular range with  $d = 360$ . This means that the angular range and the *number* of projection angles vary simultaneously.

The experiments described above are based on noiseless projection data. In the fourth series of experiments the robustness of the reconstruction algorithms with respect to noise is examined. First, noiseless projection data are computed. Poisson distributed noise with varying  $I_0$  (number of counts per detector element, measured without an object) is applied to this data. The reconstruction quality of FBP with the standard Ram-Lak is known to degrade for high noise levels. Various alternative filters have been described in the literature that are more robust to noise, including the Shepp-Logan (SL), Cosine (Cos), Hamming (Ham), and Hann (Hann) filters [4, 19]. The reconstruction

results for SIRT and SIRT-FBP are compared with the results for FBP using this range of filters.

The AFs used in the previous experiments can vary throughout the projection angles. In the fifth set of experiments, we consider an *angle independent* filter, computed by taking the average of the filters for all projection angles. This way of filtering the projection data enables an implementation very similar to FBP with a standard filter. The corresponding reconstruction algorithm will be denoted by av-SIRT-FBP and it is compared with SIRT, SIRT-FBP and with FBP for several standard filters.

Finally, we examine the accuracy of the three reconstruction methods when reconstructing an experimental  $\mu$ CT data set. A diamond was scanned using a Skyscan 1172 cone-beam  $\mu$ CT scanner. From the experimental data, 200 parallel beam projections of the central slice were determined by rebinning the corresponding fan-beam projection data. Reconstructions computed from these projections using FBP-RL, SIRT and SIRT-FBP are compared.

As noted before, computing an AF is highly computationally intensive. An optimized GPU implementation of the SIRT algorithm was used to generate the filters, running on a Tesla S1070 quad-GPU system. As an example of the running time, we mention computing a filter for an image of size  $511 \times 511$ , using 64 angles and a detector of size 511. The running time for 200 iterations of the SIRT algorithm on a single GPU is around 0.5 s. To compute the AF for all angles, this computation must be carried out  $64 \times 511$  times, resulting in a total running time of 4.5 h.

## 2.6 RESULTS

In this section we provide an overview of the results of the experiments. In addition to the quantitative results concerning the reconstruction and projection errors, a selection of the reconstructed images is shown, which is chosen such that it illustrates the behavior of the reconstruction methods.

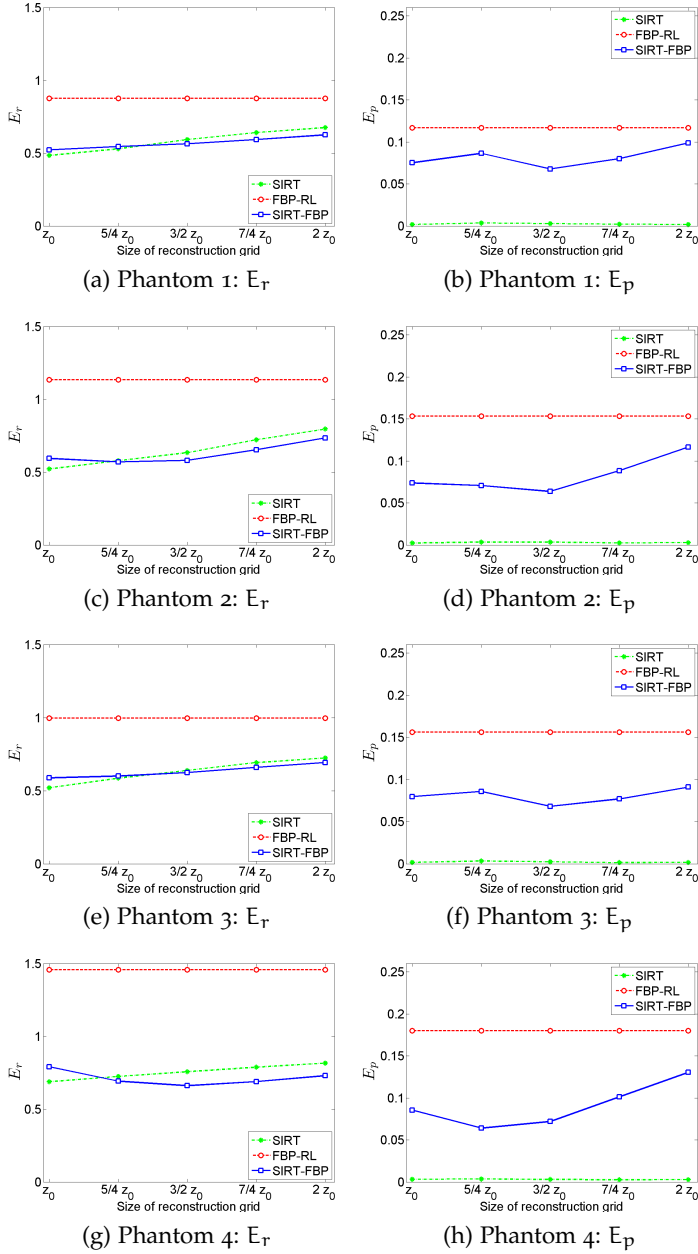


Figure 2.3: Mean reconstruction and projection error as a function of the size of the reconstruction grid, with  $d = 32$ .

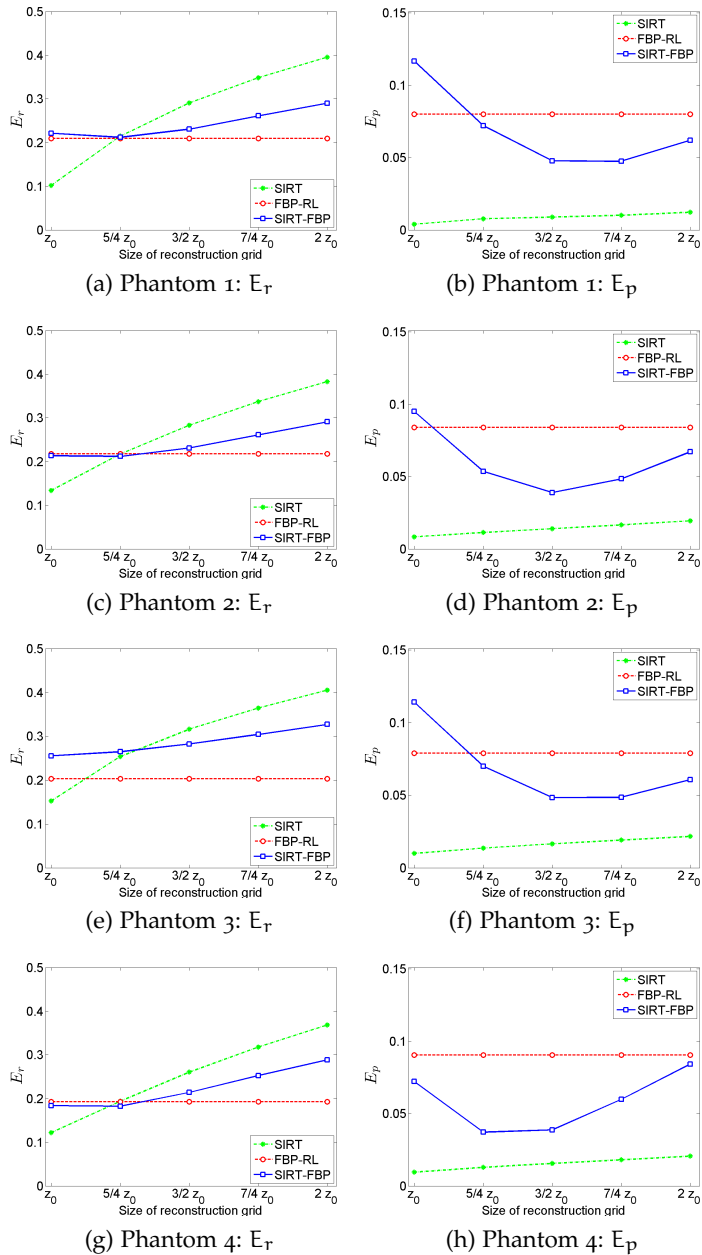


Figure 2.4: Mean reconstruction and projection error as a function of the size of the reconstruction grid, with  $d = 256$ .

### 2.6.1 Varying the Size of the Reconstruction Grid

As the SIRT reconstruction depends on the size of the reconstruction grid  $z$ , the filters that are based on SIRT reconstructions also depend on  $z$ , thereby affecting the quality of the SIRT-FBP reconstructions. In the first series of experiments we examine the accuracy of the reconstructions as a function of  $z$ . During the first run, the relatively low number of 32 projection angles is used, while for the second run a larger set of 256 projection angles is used.

Reconstruction errors are shown in Fig. 2.3 and Fig. 2.4, for  $d = 32$  and  $d = 256$  angles, respectively, where the mean reconstruction error is plotted in the first column and the mean projection error in the second column. As expected, the errors of the FBP-RL reconstructions are independent of  $z$ . Since the number of unknowns of the equation system that is solved by SIRT increases with increasing  $z$ , while the number of equations remains the same, the system becomes increasingly underdetermined. This results in decreasing reconstruction accuracy of SIRT as a function of  $z$ . The results show that the reconstruction error for SIRT-FBP is minimal when  $z$  is between  $z_0$  and  $\frac{3}{2}z_0$ . For larger grid sizes the decreasing quality of the SIRT reconstructions determines the behavior of the errors of the SIRT-FBP reconstructions. The minimal mean projection error occurs close to  $z = \frac{3}{2}z_0$ , and the error of SIRT-FBP for this grid size is significantly less than the mean projection error of FBP-RL. Furthermore, the quality of the SIRT-FBP reconstructions with  $d = 32$  exceeds that of FBP-RL and SIRT on grids with  $z$  between  $\frac{3}{2}z_0$  and  $2z_0$ . Such results are not to be expected for  $d = 256$ , since for a sufficiently large number of angles FBP-RL is known to outperform SIRT. Still we see that SIRT-FBP has a significantly smaller reconstruction error than SIRT on these grid sizes.

### 2.6.2 Varying the Projection Angles

In the second series of experiments the number of projection angles  $d$  is varied between 16 and 256 angles, while  $z$  is kept fixed at  $z = \frac{3}{2}z_0$ , based on the results of the previous experiments. Some reconstructions of Phantom 3 are shown in Fig. 2.5. Fig. 2.6 shows that, for all considered numbers of projection angles, the mean projection error of SIRT-FBP is smaller than the mean projection error of the FBP-RL re-



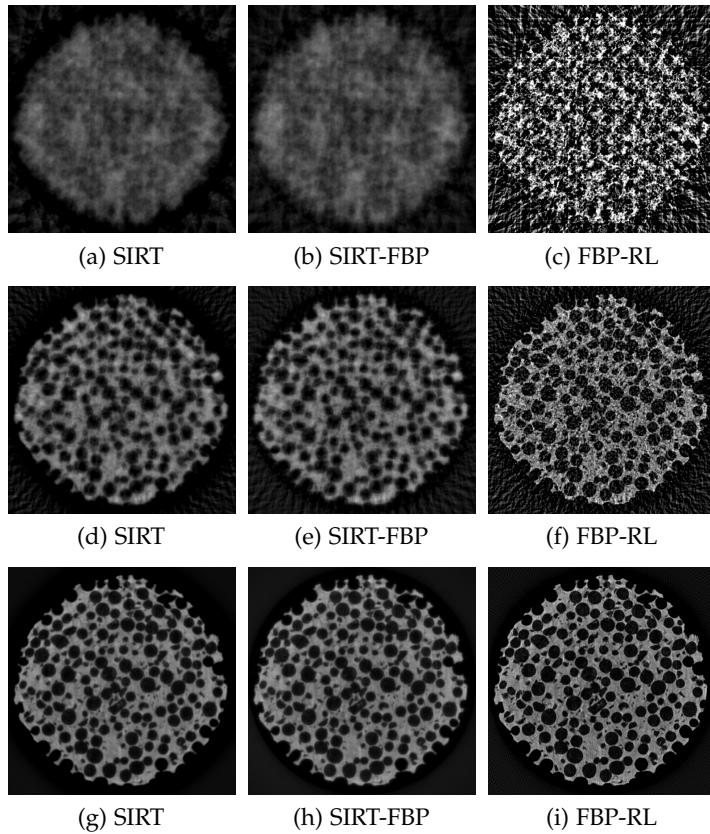


Figure 2.5: Reconstructions of phantom 3 with  $z = (3/2)z_0$  and varying number of projection angles. Top row:  $d = 16$ . Middle row:  $d = 64$ . Bottom row:  $d = 256$ .

constructions. For most phantoms, the projection error is also smaller for SIRT-FBP than for FBP-RL, as long as the number of angles is not too large (i.e., at most 192).

### 2.6.3 Varying the Angular Range

In this series of experiments the angular range is varied between  $5^\circ$  and  $170^\circ$ . Fig. 2.7 shows the difference between Phantom 1 and its reconstructions for a selection of the considered limited angular ranges, i.e.  $35^\circ$ ,  $80^\circ$ ,  $125^\circ$  and  $70^\circ$ , comparing SIRT, SIRT-FBP and FBP-RL. The values of the difference plots range between black and white, where a

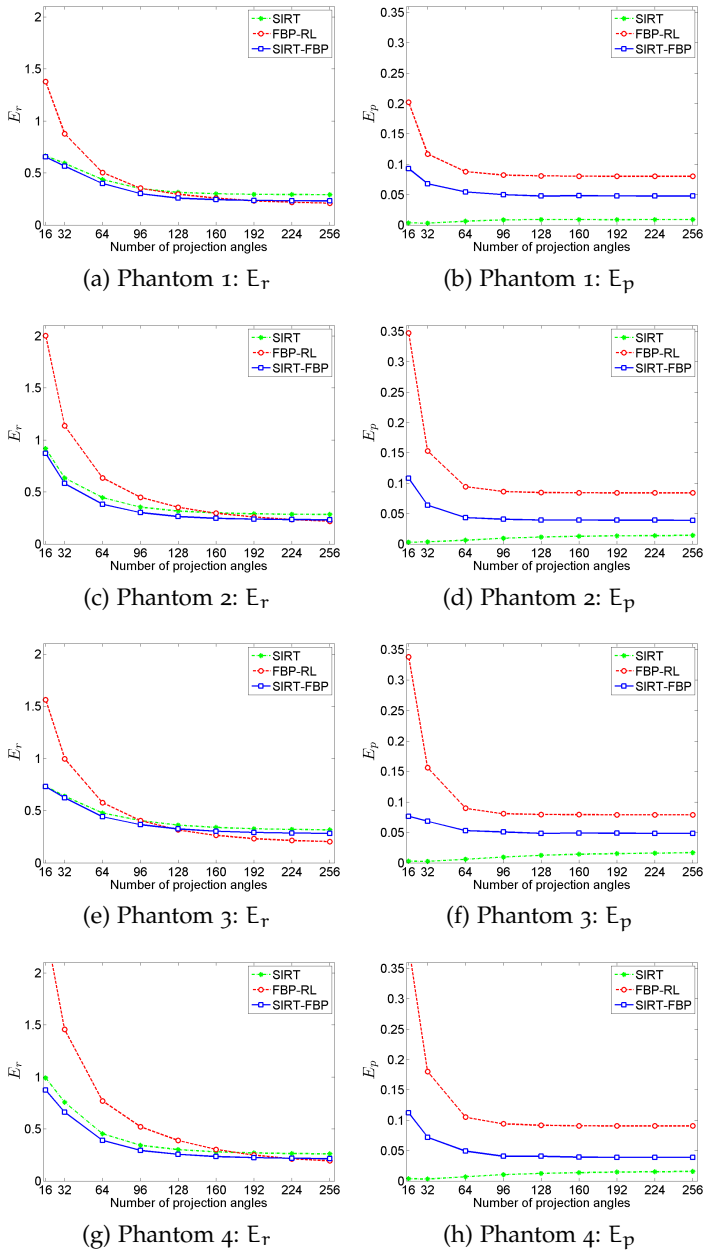


Figure 2.6: Mean reconstruction and projection error as a function of the number of projection angles with  $z = (3/2)z_0$ .

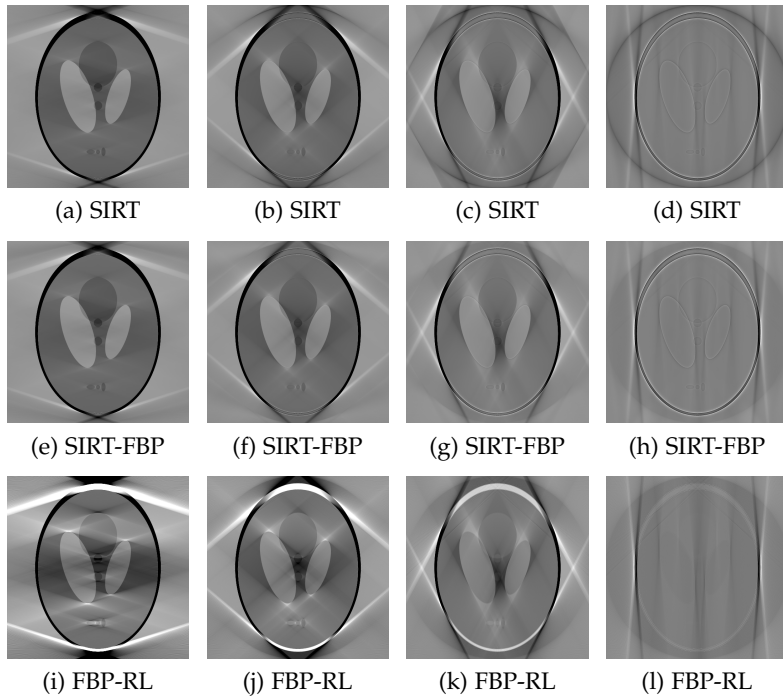


Figure 2.7: Difference between the original image and reconstructions of phantom 1 with  $z = (3/2)z_0$  and varying angular range; limited angular range per column (from left to right):  $35^\circ$ ,  $80^\circ$ ,  $125^\circ$ ,  $170^\circ$ . Dark (light) pixels correspond to reconstruction values that are higher (smaller) than those of the original phantom.

pixel is black if the corresponding reconstruction pixel has a value of at least  $(3/2)$  the value of the phantom pixel, and a pixel is white if the corresponding reconstruction pixel has a value of at most  $(1/2)$  the value of the phantom pixel. The difference plots for SIRT and SIRT-FBP are very similar, while FBP-RL results in quite different reconstructions. The results in Fig. 2.8 show the accuracy of the reconstructions when the angular range is limited, for the three methods. The projection error is calculated using only those projections that are included in the angular range. The reconstruction errors of SIRT-FBP are similar to those of SIRT reconstructions, while for an angular range below  $150^\circ$  the reconstruction errors of SIRT-FBP are much smaller than the errors of FBP-RL for all phantoms.

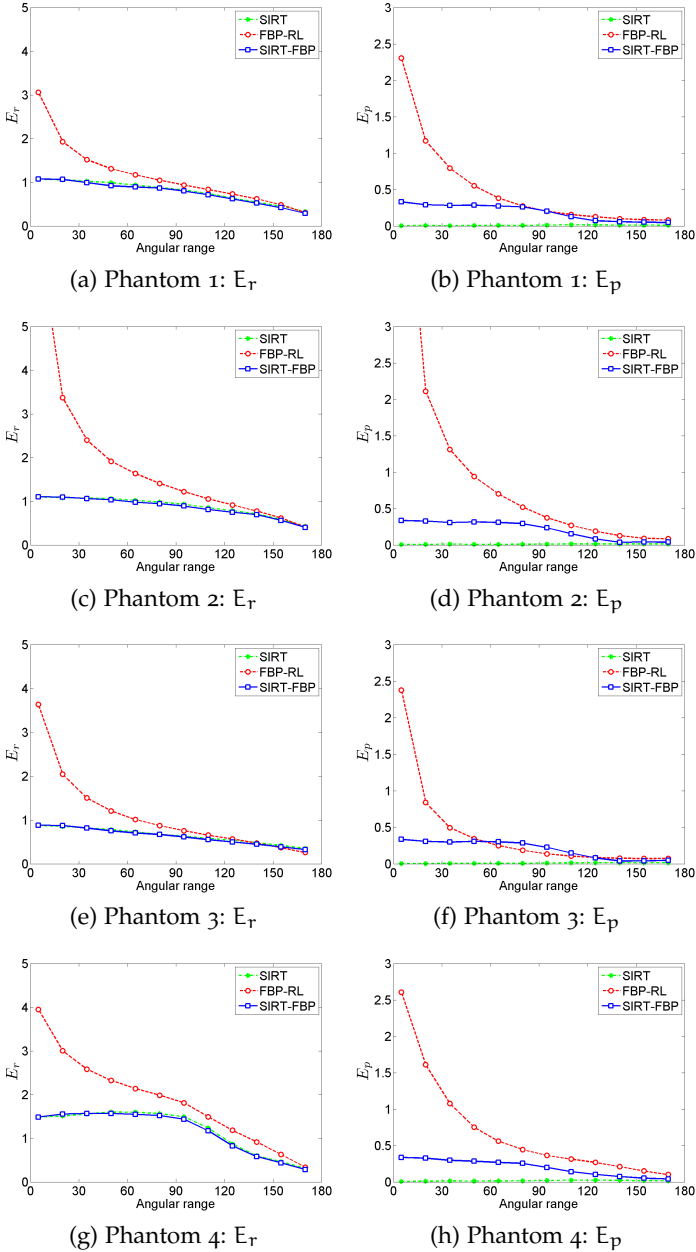


Figure 2.8: Mean reconstruction and phantom error as a function of the angular range with  $z = (3/2)z_0$ .

The projection error of SIRT-FBP reconstructions is smaller than that of FBP-RL for almost all test cases. Since SIRT-FBP is an approximation of SIRT, some discrepancy exists between the SIRT and SIRT-FBP reconstructions. The magnitude of this effect depends on the particular image, which can lead to an inferior reconstruction quality of SIRT-FBP compared to FBP-RL in certain cases. An example is Phantom 3 in Fig. 2.8 for the limited angular range between  $60^\circ$  and  $120^\circ$ . The magnitude of this effect depends on the particular image. The results also demonstrate that for the cases where iterative reconstruction methods perform well, i.e. few projection angles or highly limited angular range, SIRT-FBP clearly outperforms FBP-RL.

#### 2.6.4 Variations in the Filters

Since the operation of the SIRT algorithm depends on both the size of the reconstruction grid and the set of projection angles, the corresponding filters also depend on these parameters. Fig. 2.9 shows a selection of filters computed for the central pixel for a varying number of projection angles and varying grid size, respectively. Every row in these grayscale figures represents a filter. Consecutive rows correspond to consecutive angles and the first row corresponds to the filter for an angle of  $0^\circ$ . The standard Ram-Lak filter, which does not depend on the projection angle, is also shown for comparison. The SIRT-based filters corresponding to an angle of  $0^\circ$  for  $d = 64$  and  $d = 256$  are also shown as line plots in Fig. 2.10 together with the standard Ram-Lak filter. Note that the algebraic filters depend on the particular projection angle. As the reconstruction grid in our experiments is a square, the algebraic reconstruction problem is not rotationally invariant, not even when pixel discretization effects are neglected. In the grayscale figures that show the SIRT-based filters some irregularities appear in the form of lines. These may be attributed to aliasing effects due to discretization of both the detector and the image domain. For the case of limited angle tomography, we found that presenting a thorough, yet compact overview of the filter variations is not straightforward. The filters may vary significantly depending on the particular projection angle.

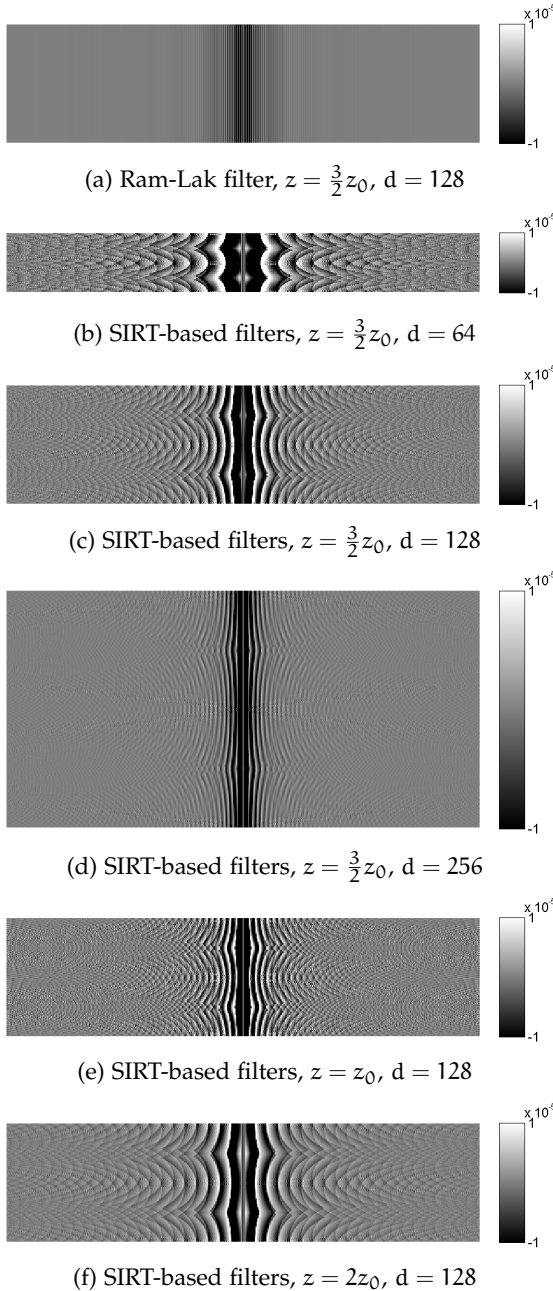
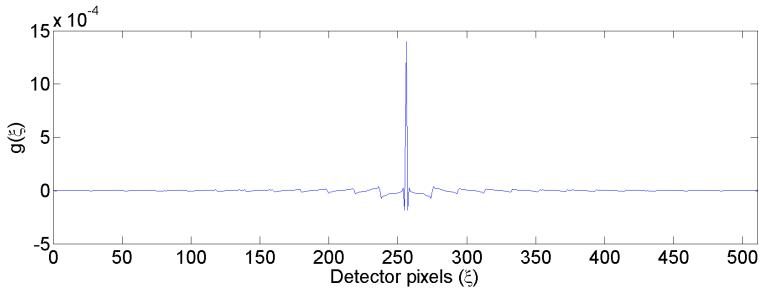
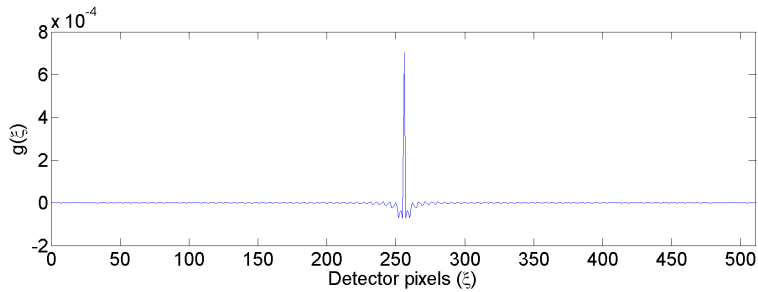
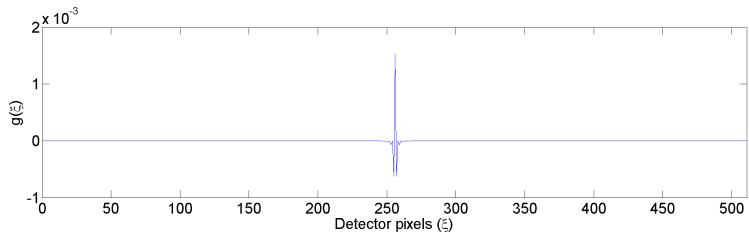


Figure 2.9: Grayscale representations of various filters, where each row represents a filter for some projection angle. In all cases, a detector with 511 bins was used ( $z_0$ ). Both the size of the reconstruction grid  $z$  and the number of projection angles  $d$  is varied. The range of the gray scale is  $[-1, 1] * 10^{-5}$ .

(a) Filter for  $\theta = 0^\circ$ ,  $z = (3/2)z_0$ ,  $d = 64$ (b) Filter for  $\theta = 0^\circ$ ,  $z = (3/2)z_0$ ,  $d = 256$ 

(c) Ram-Lak filter

Figure 2.10: Two AFs used in SIRT-FBP and the standard Ram-Lak filter in the spatial domain.

### 2.6.5 Noise

All experiments so far were performed using noiseless projection data. FBP-RL is known to produce poor quality reconstructions from projection data that are highly polluted with noise, while SIRT handles this data relatively well. In this series we examine the accuracy of SIRT-FBP compared to FBP with several common filters and SIRT in case of noisy projection data, where the detector count  $I_0$  ranges from  $10^2 - 10^6$ . Some reconstructions are shown in Fig. 2.11. The re-

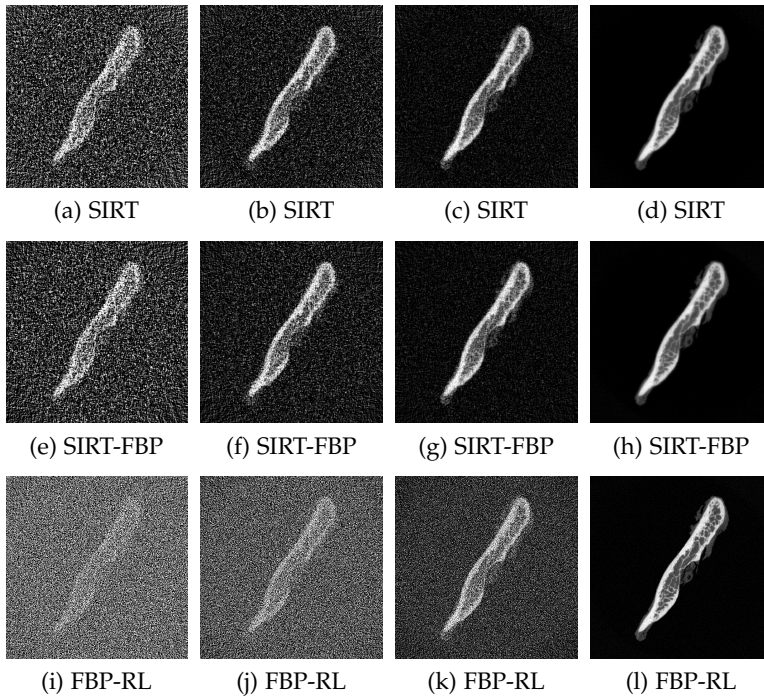


Figure 2.11: Reconstruction of phantom 4 with  $z = (3/2)z_0$  and varying noise levels,  $I_0$  per column (from left to right): 250, 1000, 5000,  $10^6$ .

sults in Fig. 2.12 show that the reconstruction errors of SIRT-FBP and SIRT are very similar and that the reconstruction and projection errors of SIRT-FBP are significantly lower than the corresponding errors of FBP reconstructions with any standard filter used in this experiment. Surprisingly, the projection errors for SIRT-FBP are smaller than for SIRT for very high noise levels. This can be attributed to the fact that for SIRT, noise can accumulate in corners of the reconstruction grid, where the intersection between projected lines and the image domain is very small for certain projection angles. These effects may cause numerical instabilities, resulting in a somewhat larger projection error, which does not occur for SIRT-FBP as only the angle-dependent filter for the central pixel is employed there. We remark that one cannot say that SIRT-FBP is more robust to noise than FBP in general, as SIRT-FBP itself is just a variant of FBP with an appropriately chosen filter.



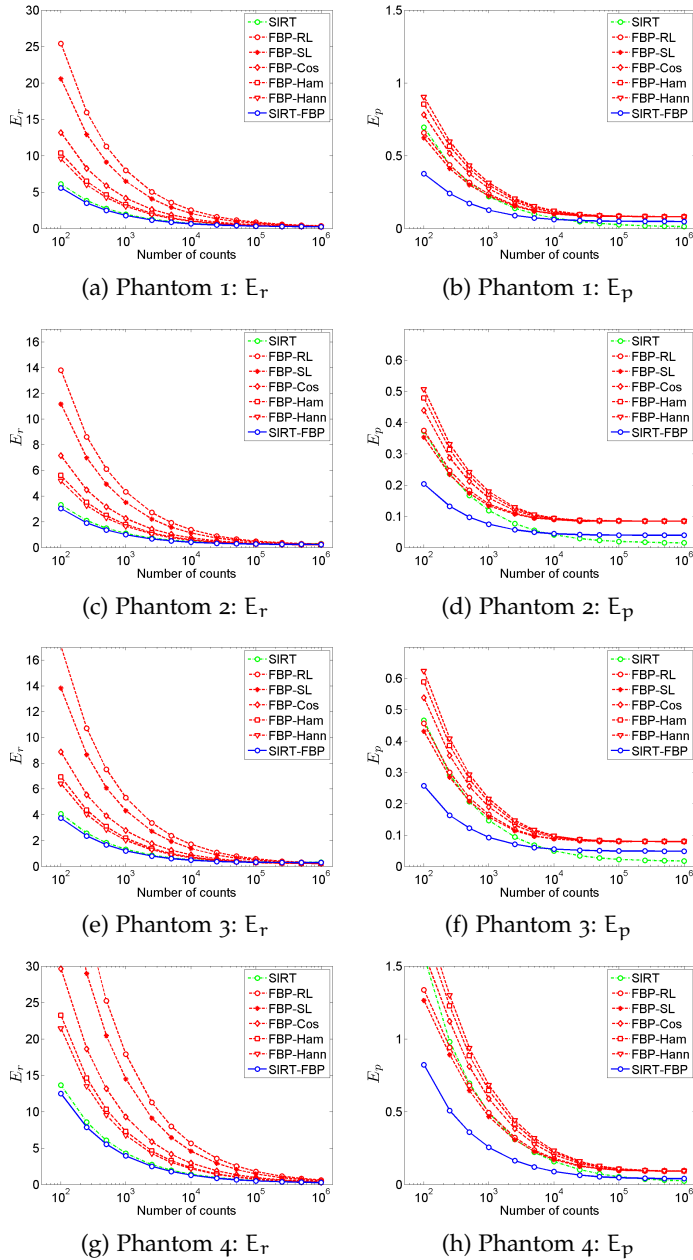


Figure 2.12: Mean reconstruction and projection error as a function of the noise level with  $z = (3/2)z_0$  and  $d = 256$ .

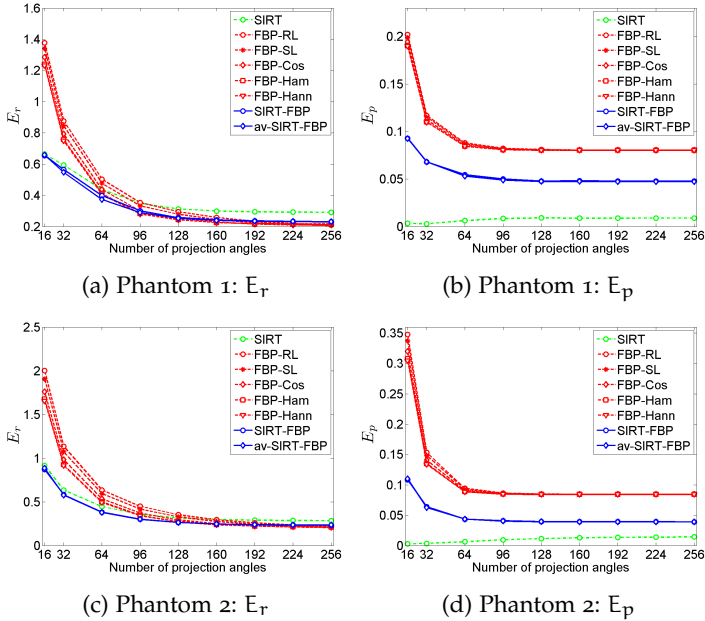


Figure 2.13: Mean reconstruction and projection error of FBP with several standard filters, SIRT, SIRT-FBP, and av-SIRT-FBP, as a function of the number of projection angles with  $z = (3/2)z_0$ .

### 2.6.6 Experiments with an angle independent filter

In this series of experiments, av-SIRT-FBP is compared with SIRT-FBP, SIRT and with FBP based on various standard filters. Although the implementation of av-SIRT-FBP is similar to FBP with a standard filter, the quality of av-SIRT-FBP reconstructions is comparable to that of SIRT-FBP reconstructions, as can be seen in Fig. 2.13 for Phantoms 1 and 2. The reconstructions of Phantoms 3 and 4 show similar patterns and are therefore not included. We remark that in some cases, av-SIRT-FBP actually results in a smaller reconstruction error compared to both SIRT and SIRT-FBP. As all experiments presented here deal with underdetermined systems of linear equations, even SIRT cannot be expected to converge to the phantom image. As both SIRT-FBP and av-SIRT-FBP are approximations to SIRT, they sometimes perform better and sometimes worse than SIRT.

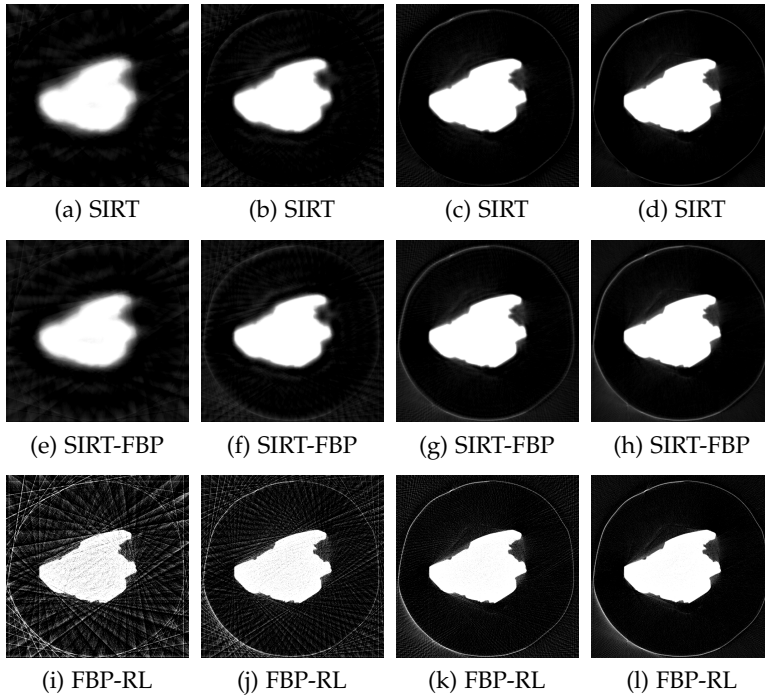


Figure 2.14: Diamond reconstruction with  $z = (3/2)z_0$  from experimental  $\mu$ CT data;  $d$  per column (from left to right): 20, 40, 100, 200.

### 2.6.7 Experimental $\mu$ CT data

For the final experiments, an experimental  $\mu$ CT data set is used. The dataset was acquired by scanning a raw diamond using a Skyscan 1172  $\mu$ CT scanner. Cone-beam projection data were acquired for 400 angles in a full  $360^\circ$  angular range, using an angular step size of  $0.9^\circ$ . The camera pixel size was  $41\mu\text{m}$ . The projection data for the central slice are effectively fan-beam data. Since the FBP algorithm and filter derivation used in this chapter are based on a parallel beam geometry, the projection data were rebinned to a parallel beam geometry, forming a dataset of 200 parallel beam projections equally distributed between  $0^\circ$  and  $180^\circ$ . Each of the projections consists of 511 detector values.

Since the ground truth data are not available, the reconstructions are compared with *each other* to analyze the reconstruction behavior for the different algorithms. The results in Fig. 2.15 show that the error

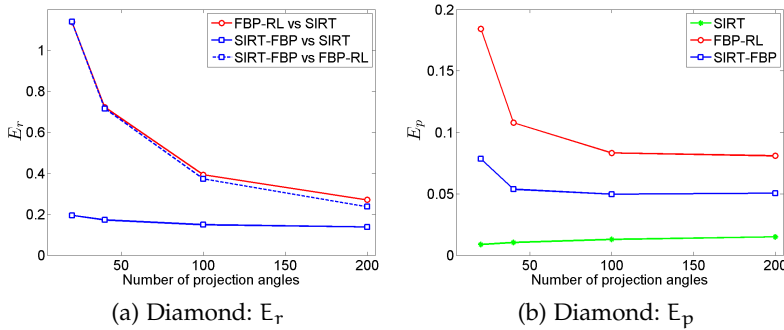


Figure 2.15: Reconstruction errors as a function of the number of projection angles for the experimental  $\mu$ CT diamond data with  $z = (3/2)z_0$ . As there is no ground truth data available, a comparison is made between pairs of reconstructions computed by different algorithms.

of the SIRT-FBP reconstructions behaves very similar to that of SIRT reconstructions, while the difference between SIRT-FBP and FBP-RL reconstructions is comparable to that between SIRT and FBP-RL reconstructions. The reconstructions in Fig. 2.14 show the same behavior patterns. For low numbers of projection angles the mean projection error of SIRT-FBP is much less than that of FBP-RL.

## 2.7 CONCLUSIONS

In this chapter, we have presented an algorithmic approach for computing AFs that can be used within the framework of the well-known FBP algorithm. The resulting AF-FBP reconstructs objects with the computational efficiency of FBP, while maintaining the more robust reconstruction properties of the chosen algebraic reconstruction technique. We have presented a formal description of the AFs and examined their properties in several series of experiments for the algebraic reconstruction method SIRT. The results showed that SIRT-FBP reconstructions are very similar to SIRT reconstructions. Therefore, AF-FBP could be applied in situations, where FBP with standard filters was known to produce low quality reconstructions and algebraic reconstruction techniques yield superior results, such as low dose tomography, limi-

ted angle tomography, etc. Computing the AF has a high computational cost. However, for a fixed scanning geometry and a fixed set of projection angles, this computation must be performed only once, as it does not depend on the scanned object. The filter computation should, therefore, be considered as a calibration step, which can be performed in an off-line setting. In further research, the properties of AF-FBP will be analyzed in more detail and generalizations to other common geometries, such as various cone-beam geometries will be considered.

#### ACKNOWLEDGEMENTS

The authors would like to acknowledge W.J. Palenstijn from the Vision Lab., University of Antwerp, Wilrijk, Belgium, for developing the high-performance GPU code used to generate the algebraic filters and assisting in the computations. They are grateful to J. Sijbers, also from the Vision Lab., for several useful discussions.

## BIBLIOGRAPHY

- [1] F. Natterer. *The Mathematics of Computerized Tomography*. Philadelphia: SIAM, 2001.
- [2] A. C. Kak and M. Slaney. *Principles of Computerized Tomographic Imaging*. Philadelphia: SIAM, 2001.
- [3] T. M. Buzug. *Computed Tomography: From Photon Statistics to Modern Cone-Beam CT*. Berlin: Springer, 2008.
- [4] G. T. Herman. *Fundamentals of Computerized Tomography: Image Reconstruction from Projections*. Berlin: Springer, 2009.
- [5] X. Pan, E. Y. Sidky, and M. Vannier. Why do commercial CT scanners still employ traditional, filtered back-projection for image reconstruction? *Inv. Problems* 2009; 25(12): 123009.
- [6] L. A. Feldkamp, L. C. Davis, and J. W. Kress. Practical cone-beam algorithm. *J. Opt. Soc. Am.* 1984; 1(A6): 612–619.
- [7] F. Xu and K. Mueller. Accelerating Popular Tomographic Reconstruction Algorithms On Commodity PC Graphics Hardware. *IEEE Trans. Nucl. Science* 2005; 52(3): 654–663.
- [8] D. Castano-Diez, H. Mueller, and A. S. Frangakis. Implementation and performance evaluation of reconstruction algorithms on graphics processors. *Journal of Structural Biology* 2007; 157(1): 288–295.
- [9] J. K. Older and P. C. Johns. Matrix formulation of computed tomogram reconstruction. *Physics in Medicine and Biology* 1993; 38(8): 1051–1064.
- [10] R. Clack. Towards a complete description of three-dimensional filtered backprojection. *Physics in Medicine and Biology* 1992; 37(3): 645–660.
- [11] H. Kunze et al. Pre-calculation of the image quality of the Simultaneous Iterative Reconstruction Technique. *Proc. of SPIE Medical Imaging*. 2007: 6510: 65105E.
- [12] A. Markoe. *Analytic Tomography*. New York: Cambridge University Press, 2006.
- [13] J. Hsieh Y. Wei G. Wang. An intuitive discussion on the ideal ramp filter in computed tomography (I). *J. Comput. Math. Appl.* 2005; 49(5–6): 731–740.

- [14] A. K. Louis and Th. Schuster. A Novel Filter Design Technique in 2D - Computerized Tomography. *Inverse Problems* 1995.
- [15] H. Kunze et al. Filter determination for Tomosynthesis aided by iterative reconstruction techniques. *Proc. of Fully3D* 2007: 309–312.
- [16] J. Ludwig et al. A Novel Approach for Filtered Backprojection in Tomosynthesis Based on Filter Kernels Determined by Iterative Reconstruction Techniques. *Proc. of IWDM* 2008; 5116: 612–620.
- [17] J. Gregor and T. Benson. Computational analysis and improvement of SIRT. *IEEE Trans. Med. Imag.* 2008; 27(7): 918–924.
- [18] P.M. Joseph. An improved algorithm for reprojecting rays through pixel images. *IEEE Trans. Med. Imag.* 1982; 1(3): 192–196.
- [19] L. A. Shepp and B. F. Logan. The Fourier reconstruction of a head section. *IEEE Trans. Nucl. Science* 1974; 21(3): 21–43.





---

## SPATIAL VARIATIONS IN RECONSTRUCTION METHODS FOR CT

---

*Abstract* – In both Filtered Backprojection and algebraic reconstruction algorithms for tomography, the reconstruction of an object can depend on the position of the object within the discretized region, even if the object is aligned perfectly with pixel boundaries. In this chapter, we investigate this effect and report on a simulation study concerning *spatial dependencies* in these reconstruction methods. We demonstrate that for algebraic methods, these dependencies are influenced not only by the discretization within the reconstruction region, but also by the *shape* of the reconstruction region itself.

### 3.1 INTRODUCTION

Most reconstruction algorithms for CT can be assigned to either the class of analytical reconstruction methods, which are based on analytical inversion formulas of the Radon transform, or to the class of algebraic reconstruction methods, which start with a discretized inverse problem and then apply a numerical solver [1–3].

One of the fundamental differences between these two classes relates to the spatial locality of the reconstruction properties. Analytical inversion formulas are usually spatially invariant, in the sense that the value of a particular point in the reconstruction only depends on the measured values relative to the position of that point. If this dependency is known for a single point, it can be applied to all image points (e.g., pixel centers) to obtain a full reconstruction. Also, there is no predefined window outside which the reconstruction must be zero. The well-known Filtered Backprojection (FBP) algorithm is obtained by discretizing an analytical inversion formula of the Radon transform, and can therefore be expected to have approximately similar properties.

For *algebraic methods* on the other hand, there is no intrinsic reason why the reconstruction should be spatially invariant, and the reconstruction is constrained a priori to a *reconstruction region*, which is discretized and represented by a collection of basis functions. Outside this region, the reconstruction is automatically set to zero, as the exterior region is not covered by the support of the basis functions.

For both FBP and algebraic methods, there may be differences in the way projection values are sampled to determine the value of an image pixel, depending on the position of that pixel, due to discretization and interpolation effects within the projection model. As a consequence, reconstructing an object centered at one position within the reconstruction region may yield a different result from reconstructing this same object centered at another position. We refer to these variations as *discretization-effects*.

For algebraic methods, the *shape* and position of the reconstruction region with respect to the object can also influence its reconstruction. For example, if a line intersects the reconstruction region as a short segment in a corner, noise that is present in the projection for that line can have a strong impact on the values of the pixels on the small segment. For a line segment that has a longer intersection with the reconstruction region, the noise can be distributed among many pixels on

that segment. We refer to these local reconstruction variations, which depend on the shape of the reconstruction grid, as *shape-effects*.

In this chapter, we report on a case study that was carried out to investigate both discretization-effects and shape-effects for the FBP method and the Simultaneous Iterative Reconstruction Technique (SIRT), respectively. By moving an object across the reconstruction region and observing how its reconstruction changes with position, we keep track of both effects and obtain error maps that can be interpreted visually and analyzed quantitatively.

This chapter is structured as follows: In Section 3.2, we briefly review the discretization approach followed for FBP and SIRT, respectively. Section 3.3 describes the simulation experiments performed. The results of these experiments are presented in Section 3.4, mainly by providing a sequence of images that represent two different error measures, as a function of the position within the reconstruction region. In Section 3.5, the observations are discussed and future work in this direction is briefly outlined.

## 3.2 METHOD

The Filtered Backprojection (FBP) algorithm is obtained by discretizing the following inversion formula of the Radon transform (see Section 3.3.2 of [1] for details):

$$f(x, y) = \int_{\theta=0}^{\pi} \int_{\tau=-\infty}^{\infty} p(\theta, \tau - x \cos \theta - y \sin \theta) g(\tau) d\tau d\theta, \quad (3.1)$$

where  $f : \mathbb{R}^2 \rightarrow \mathbb{R}$  denotes the unknown image,  $p(\theta, \tau)$  denotes the measured line projection at angle  $\theta$  and detector coordinate  $\tau$ , and  $g$  denotes a *filter*, which determines how the detector values are weighted before backprojection to form the value at position  $(x, y)$ . If we assume that  $p$  corresponds to the Radon transform of a certain original object, it is easy to see that translating this object over  $(\Delta x, \Delta y)$  leads to a corresponding translation in the reconstruction over  $(\Delta x, \Delta y)$ . As a consequence of the discretization step in FBP, interpolation steps are required to compute an approximation of Eq. (3.1), leading to violations in this translational property, which we refer to as *discretization-effects*.

In *algebraic* reconstruction methods, the image is represented as a finite weighted sum of *basis functions* (see, e.g., Chapter 7 of [1] or

Section 6.3 of [2]). For this chapter, we limited ourselves to the reconstruction of 2-dimensional (2D) slices from 1D parallel beam projections using a standard pixel basis, yet the general methodology can be applied to 3D volume reconstruction using various types of basis functions, and various acquisition geometries.

When setting up an algebraic method, it is assumed that a certain *reconstruction region* is known, which completely contains the scanned object. Typically, this region is chosen to be either square or rectangular, while sometimes it is modelled as a disk. This region is then discretized along with the projection operator, leading to the following relation between the unknown image  $\mathbf{x}$  and the measured projection data  $\mathbf{p}$ :

$$\mathbf{W}\mathbf{x} = \mathbf{p}, \quad (3.2)$$

where  $\mathbf{W} = (w_{ij}) \in \mathbb{R}^{m \times n}$  denotes the *projection matrix*,  $\mathbf{x} = (x_j) \in \mathbb{R}^n$  is a vector representation of the pixel values in the unknown image, and  $\mathbf{p} = (p_i) \in \mathbb{R}^m$  represents the full set of measured detector values in all projections.

The exact projection matrix  $\mathbf{W}$  depends on the selection of the reconstruction region, the choice and distribution of basis functions to represent the image within this region, and the model used for the projection operator.

The system in Eq. (3.2) is typically solved using iterative numerical solvers, as it is both very large and sparse. In this article, we consider one such iterative method called SIRT [4, 5], which converges to a weighted least-squares solution of the equation system.

Note that not all individual linear equations in Eq. (3.2) have the same algebraic structure. Each equation corresponds to a projected line. Depending on the intersection properties of that line with the discretized reconstruction region, the number of unknown pixel values that occur in the equation can vary, as well as their coefficients. As a consequence, the shape of the reconstruction region can influence the reconstruction of an object, depending on its location within that region, referred to as *shape-effects* of the reconstruction region.

### 3.3 EXPERIMENTS

To investigate discretization-effects and shape-effects for both FBP and SIRT, we performed a simulation study on the reconstruction of a small object that is placed at varying positions within the reconstruction region. All experiments were carried out using two different choices for the reconstruction region: (a) a square region of size  $63 \times 63$  square pixels of unit size; (b) a pixelated circular region that is circumscribed around the square region of (a).

We compare the results for Filtered Backprojection (FBP) using the ramp-filter, which exhibits only discretization-effects, with the Simultaneous Iterative Reconstruction Technique (SIRT), which is expected to show both discretization-effects and shape-effects. For SIRT, 200 iterations are performed with a relaxation factor of 1. This iteration number ensures that convergence has been reached.

Projection data were simulated for a parallel detector geometry, using a detector consisting of 91 bins of unit size, thereby ensuring that the full reconstruction region is covered by the detector. The simulation was performed using a ray-driven projector based on the Joseph kernel to determine the contribution of an image pixel to each ray [6], implemented as a parallel operation on the GPU [7]. The projection angles of the parallel beam projections are regularly distributed between 0 and 180 degrees. The number of projection angles is kept fixed at 64. For the SIRT reconstruction, a forward projector based on the Joseph kernel was used.

As test objects, the square and cross images in Fig. 3.1a were used. The reconstructions of these objects, when placed in the center of a square reconstruction region, are shown in Fig. 3.1b and 3.1c.

#### 3.3.1 *Experiments without noise*

In the first experiment, based on noiseless projection data, the test objects were moved across the reconstruction area. For each position of the object, its forward projection was computed and the object was reconstructed. The reconstruction within a small window around the object (a surrounding square, containing a boundary layer of one pixel thickness) was then shifted, placing the reconstructed object in the center of the reconstruction region. A comparison was made with the re-

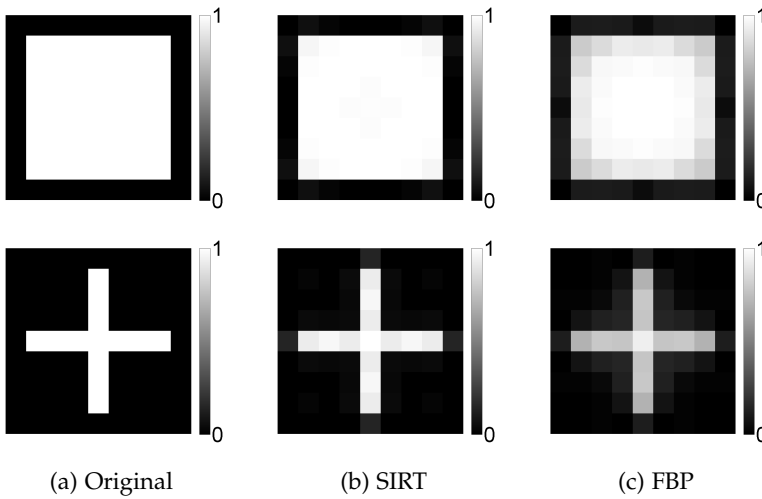


Figure 3.1: Test objects and their reconstructions when placed in the center of the reconstruction region.

construction for which the object was placed in the center, using the following two error measures: (a) the root mean square error (RMSE) for all pixels in the window; (b) the absolute value of the difference in average intensity within the object (AIE).

### 3.3.2 Experiments that include noise

In the second experiment, the test objects were again moved across the reconstruction area. Poisson distributed noise was applied to the projection data based on a flatfield photon count of  $10^6$  per detector pixel. As the exact noise realization depends on the simulated photon counts, which in turn are affected by discretization issues, we chose to compare the reconstructions to the actual test object, instead of comparing to its reconstruction in the center. The reconstruction within a window around the object (a surrounding square, containing a boundary layer of five pixels thickness) was compared with the original object, using the following two error measures: (a) the root mean square error (RMSE) for all pixels in the window; (b) the absolute value of the difference in average intensity within the object (AIE).

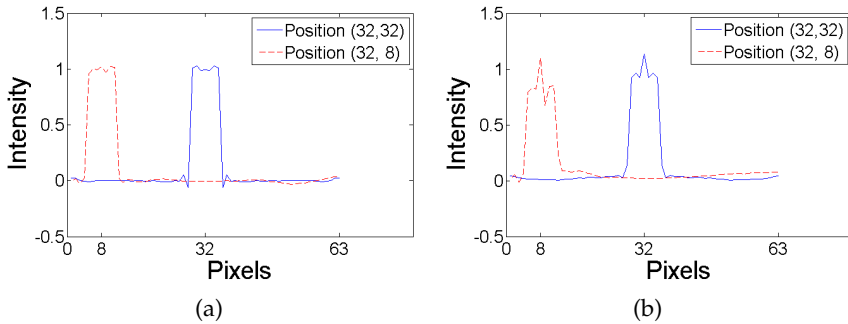


Figure 3.2: Intensity profile of an object at the center (blue line) and centered at pixel (32,8) (dashed red line); (a) square object, (b) plus object.

### 3.4 RESULTS

In this section, we examine the discretization and shape effects of SIRT and FBP for two test objects and two different shapes of the reconstruction grid.

#### 3.4.1 Noiseless projection data

In the first series of experiments, the reconstructions of the noiseless projection data of a shifted object are compared with the reconstructions of the same object placed in the center of the reconstruction region. Reconstructions of the phantoms contain a variety of intensity levels within the reconstructed object. These intensity levels can be visualized by an intensity profile along a horizontal line through the center of the reconstructed object. In Fig. 3.2, the intensity profiles are shown for SIRT reconstructions of the test objects placed in the center of the reconstruction region and placed near the left boundary of the reconstruction region.

The reconstructions of the test objects clearly depend on their position in the reconstruction grid. The root mean square error for all pixels in the window is used to examine these spatial variations. In Fig. 3.3 the RMSE are shown for SIRT and FBP reconstructions of both test objects in a square reconstruction grid. The results are similar for the circular grid. Since the discretization-effects of SIRT and FBP appear to be very similar, we subtract the RMSE of FBP from that of SIRT

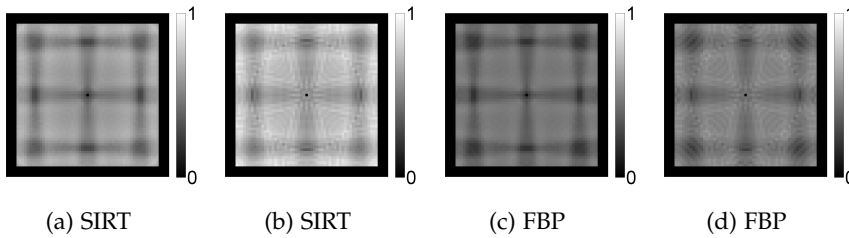


Figure 3.3: RMSE of reconstruction of the test objects using a square reconstruction grid without noise; (a) square object, (b) plus object, (c) square object, (d) plus object.

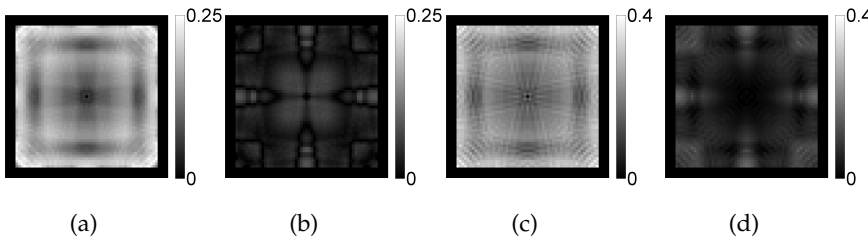


Figure 3.4: Absolute value of the difference of RMSE between SIRT and FBP of the reconstruction of the test object; (a) square phantom, square grid, (b) square phantom, circular grid, (c) plus phantom, square grid, (d) plus phantom, circular grid.

to obtain an approximation of the shape-effects for SIRT. The absolute value of this difference is shown in Fig. 3.4. Note that some scaling was required to enhance the visibility.

For square reconstruction grids, reconstructions of an object near the edge can differ substantially from a reconstruction of the same object placed in the center of the reconstruction grid. Fig. 3.4 shows that, at least in some cases, these shape-effects can be reduced by choosing a different, for example circular, reconstruction grid. These results are also supported by the second error measure (AIE), as is shown in Fig. 3.5 and 3.6.

### 3.4.2 Noisy projection data

In the second series of experiments, Poisson noise is applied to the projection data of the shifted object. An example of a SIRT and FBP reconstruction of the shifted square test object is shown in Fig. 3.7.



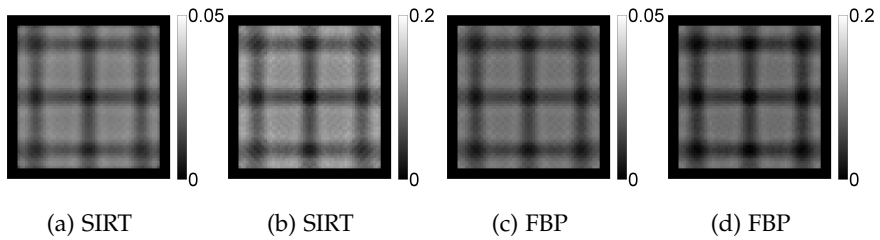


Figure 3.5: AIE of reconstruction of the test objects using a square reconstruction grid without noise; (a) square object, (b) plus object, (c) square object, (d) plus object.

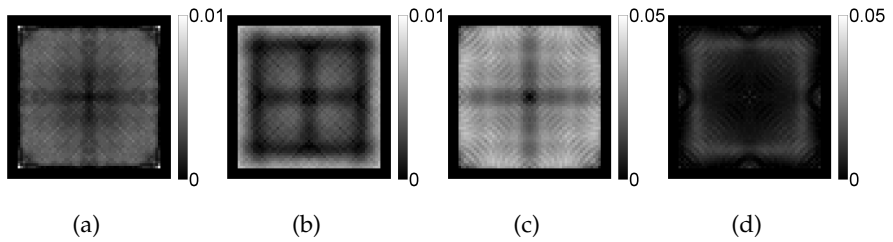


Figure 3.6: Absolute value of the difference of AIE between SIRT and FBP of the reconstruction of the test phantom; (a) square phantom, square grid, (b) square phantom, circular grid, (c) plus phantom, square grid, (d) plus phantom, circular grid.

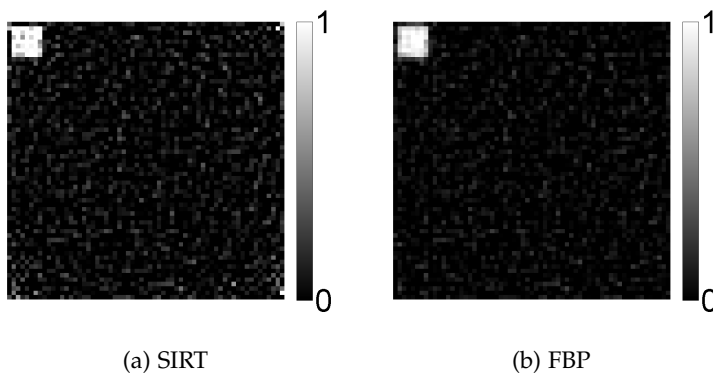


Figure 3.7: Reconstruction of the shifted square test object with Poisson noise applied to the projection data.

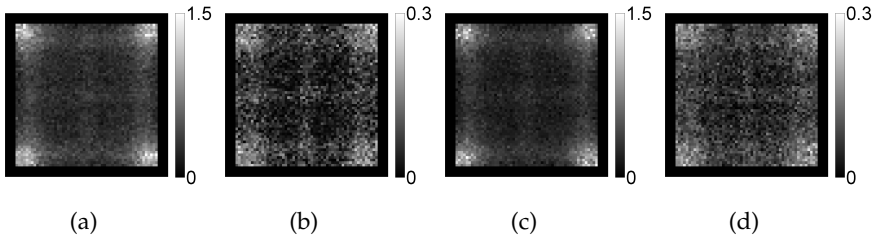


Figure 3.8: Absolute value of the difference of RMSE between SIRT and FBP of the reconstruction of the test object with Poisson noise; (a) square phantom, square grid, (b) square phantom, circular grid, (c) plus phantom, square grid, (d) plus phantom, circular grid.

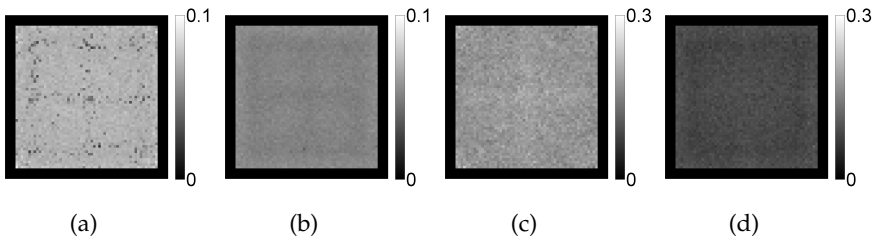


Figure 3.9: Absolute value of the difference of AIE between SIRT and FBP of the reconstruction of the test object with Poisson noise; (a) square phantom, square grid, (b) square phantom, circular grid, (c) plus phantom, square grid, (d) plus phantom, circular grid.

As mentioned in section 3.3 the reconstructions are compared to the original shifted image instead of the reconstruction of the object placed at the center of the reconstruction region. The spatial variations of SIRT due to shape-effects are again visualized by comparing both the RMSE and AIE measures of SIRT and FBP; see Fig. 3.8 and 3.9 for the RMSE and AIE measure, respectively.

Apparently, as suggested by Fig. 3.9, the total intensity within the object is invariant under the position of the test object. Fig. 3.8 shows that, also in the case of noisy projection data, SIRT reconstructions of an object depend on the position of the object in the reconstruction region. These spatial variations are influenced by the shape of the reconstruction region.

### 3.5 DISCUSSION AND CONCLUSIONS

The results of our case study demonstrate that significant discretization-effects can be observed in both FBP and SIRT reconstructions. Moreover, this effect is highly similar for both algorithms. For SIRT, the shape-effect also comes into play, yet mainly near the corners of a square reconstruction region. It appears that this effect can be mitigated by using a disk-shaped reconstruction region. The magnitude of shape-effects is increased by the influence of noise in the projection data, which can cause serious artefacts near the corners of the reconstruction region.

The actual position dependency may well depend strongly on the particular projection model used for the reconstruction. Here, we only considered the Joseph's method, which is broadly used in tomographic algorithms. In ongoing and future research, we are now focusing on the influence of different types of discretizations (e.g., blobs, wavelets) on the spatial dependencies, along with various projection models (e.g., lines, strips).

## BIBLIOGRAPHY

- [1] A. C. Kak and M. Slaney. *Principles of Computerized Tomographic Imaging*. Philadelphia: SIAM, 2001.
- [2] G. T. Herman. *Fundamentals of Computerized Tomography: Image Reconstruction from Projections*. Berlin: Springer, 2009.
- [3] X. Pan, E. Y. Sidky, and M. Vannier. Why do commercial CT scanners still employ traditional, filtered back-projection for image reconstruction? *Inv. Problems* 2009; 25(12): 123009.
- [4] P. Gilbert. Iterative methods for the three-dimensional reconstruction of an object from projections. *J. Theor. Biol.* 1972; 36(1): 105–117.
- [5] J. Gregor and T. Benson. Computational analysis and improvement of SIRT. *IEEE Trans. Med. Imag.* 2008; 27(7): 918–924.
- [6] P.M. Joseph. An improved algorithm for reprojecting rays through pixel images. *IEEE Trans. Med. Imag.* 1982; 1(3): 192–196.
- [7] W.J. Palenstijn, K.J. Batenburg, and J. Sijbers. Performance improvements for iterative electron tomography reconstruction using graphics processing units (GPUs). *J. Struct. Biol.* 2011; 176(2): 250–253.

---

APPROXIMATING ALGEBRAIC TOMOGRAPHY  
METHODS BY FILTERED BACKPROJECTION: A  
LOCAL FILTER APPROACH

---

*Abstract* – Filtered Backprojection is the most widely used reconstruction method in transmission tomography. The algorithm is computationally efficient, but requires a large number of low-noise projections acquired over the full angular range to produce accurate reconstructions. Algebraic reconstruction methods on the other hand are in general more robust with respect to noise and can incorporate the available angular range in the underlying projection model. A drawback of these methods is their higher computational cost.

In a recent article, we demonstrated that for *linear algebraic reconstruction methods*, a filter can be computed such that applying Filtered Backprojection using this filter yields reconstructions that approximate the algebraic method. In the present work, we explore a modification of this approach, where we use more than one algebraic filter in the reconstructions, each covering a different region of the reconstruction grid. We report the results of a series of experiments to determine the how well the reconstruction and approximation accuracy of this approach.

## 4.1 INTRODUCTION

Computed Tomography is a general technique for recovering an image of the interior of a scanned object from its projections, acquired from a range of angles. In this article, we focus on *transmission tomography*, where the source and detector of the scanning device are located on opposite sides outside the object. The source emits a penetrating beam that traverses the object. Depending on the thickness and composition of the materials on its path, part of the incoming beam is absorbed or scattered by the object. The measurements at the detector can be considered as *projections* of the object. This data forms the input for a *tomographic reconstruction algorithm*, which computes an image of the object from all available projections [1–3].

Most of the reconstruction algorithms proposed in the literature can be divided into two classes: (i) analytical reconstruction methods and (ii) algebraic reconstruction methods. The analytical reconstruction methods are based on discretizations of an inversion formula for the idealized continuous representation of the reconstruction problem [4]. The algebraic reconstruction methods are derived from a discrete approach of the reconstruction problem, which is formulated as a system of linear equations. Due to the large size of the problem, iterative methods are used to solve the problem instead of calculating a least-squares solution directly.

The best known example of an analytical reconstruction method is *Filtered Backprojection* [5]. Due to its fast computation time and robustness with respect to noise, it is often used to obtain reconstructions. Variants of FBP, such as the FDK algorithm for cone-beam reconstruction [6], are also highly popular in practice. A disadvantage of these reconstruction methods is their poor reconstruction quality when there are only few projection angles or when the angular range is limited.

Algebraic reconstruction algorithms, such as ART, SART, and SIRT [1, 7, 8], typically yield more accurate results in such limited data scenarios, as modeling the problem as a system of linear equations allows to encode exactly which information is known about the object, instead of interpolating data that has not been measured. The main drawback of iterative algebraic methods is that they are more computationally intensive, requiring a few times up to a hundred times the computation time of FBP.

An alternative route to obtaining more accurate reconstructions is to adjust the filter of FBP to specific properties of the projection data, the set of projection angles, or both [9–12]. In a recent article, we demonstrated that the operation of certain algebraic methods (those that are *linear*) can be approximated by applying FBP with a custom filter. This filter is computed once and depends on the particular algebraic method that is to be approximated. This method is known as *algebraic filter-filtered backprojection* (AF-FBP) [13]. For a particular pixel, the reconstructed image that results from applying FBP with this custom filter has exactly the same value as in the algebraic reconstruction. The AF-FBP reconstructions have been demonstrated to approximate the accuracy and robustness of the underlying algebraic method, while the computational efficiency is comparable to that of the fast FBP reconstruction method.

The AF-FBP method is based on selecting a particular pixel in advance, for which the filter is computed. This filter is subsequently applied to reconstruct all other image pixels as well. A logical question is therefore whether the AF-FBP method can be improved by computing *multiple* filters, at different locations in the image, and combining the FBP results for the set of computed filters.

In this article we examine the performance of such an approach, where the results of multiple algebraic filters are combined. We consider a filter sampling where nine filters are computed instead of a single one, each covering a tile in the reconstructed image. Two different ways of combining these nine AF-FBP reconstructions are experimentally examined. We compare the reconstruction accuracy with the standard AF-FBP method, with the algebraic SIRT method, and with FBP with the standard Ram-Lak filter.

This chapter is structured as follows. In Section 4.2 we briefly discuss FBP and review the standard AF-FBP method. In Section 4.3 we describe a variation on the standard AF-FBP. The experiments that we will perform are described in Section 4.4. In Section 4.5 the results of these experiments are presented. Section 4.6 contains the discussion, and the conclusions are drawn in Section 4.7.

## 4.2 INTRODUCTION TO AF-FBP

In this section we briefly introduce the key concepts of the AF-FBP method. We refer to [13] for a more detailed description. We consider here the standard case of reconstructing a 2D image from its parallel beam projections. The unknown image can be considered as a map  $\mathbb{R}^2 \rightarrow \mathbb{R}$ , which assigns a *grey level* to each image coordinate  $(x, y)$ . For  $\theta \in [0, \pi)$  and  $t \in \mathbb{R}$ , the *line projection*  $p(\theta, t)$  of  $f$  is defined by

$$p(\theta, t) = \iint_{\mathbb{R}^2} f(x, y) \delta(x \cos \theta + y \sin \theta - t) dx dy. \quad (4.1)$$

In practice, line projections are measured for a finite set of projection angles  $\theta$  and at a finite set of detector positions  $t$ . Denote the finite set of angles for which projections are available by  $\Theta = \{\theta_1, \dots, \theta_k\}$  and the finite set of detector positions for which a projected line has been measured by  $T = \{t_1, \dots, t_\ell\}$ . The *tomographic reconstruction problem* then consists of recovering  $f$  from its line projections for all  $(\theta, t) \in \Theta \times T$ . Typically, only an approximate solution can be obtained in practice.

We recall that the Filtered Backprojection algorithm can be described by

$$\tilde{f}(x, y) = \sum_{\theta \in \Theta} \sum_{\tau \in T} p(\theta, \tau) g(\theta, \tau - x \cos \theta - y \sin \theta), \quad (4.2)$$

where  $\tilde{f}(x, y)$  denotes the reconstructed image and  $g(\theta, t)$  is a pre-defined *filter*, such as the common Ram-Lak filter. Usually this filter does not depend on the projection angle  $\theta$ .

In *algebraic* reconstruction algorithms, the tomographic reconstruction problem is represented by a system of linear equations of the form

$$\mathbf{W}\mathbf{x} = \mathbf{p},$$

were the matrix  $\mathbf{W} = (w_{ij}) \in \mathbb{R}^{m \times n}$  denotes the discretized projection operator, the vector  $\mathbf{x} \in \mathbb{R}^n$  corresponds to the unknown image and the vector  $\mathbf{p} \in \mathbb{R}^m$  contains the measured projection data. The entry  $w_{ij}$  determines the weight of the contribution of pixel  $j$  to measurement  $i$ , which usually represents the length of the intersection bet-



ween the pixel and the projected line. As the equation system is usually inconsistent, an exact solution typically does not exist. For such cases, a range of numerical algorithms exist that minimize the residual  $\|\mathbf{W}\mathbf{x} - \mathbf{p}\|$  with respect to some vector norm.

A reconstruction algorithm can be considered as an operator  $\mathcal{S} : \mathbb{R}^m \rightarrow \mathbb{R}^n$ , which maps the vector  $\mathbf{p}$  of measurements to the reconstructed image  $\mathbf{x}$ . We call a reconstruction algorithm *linear* if  $\mathcal{S}$  is a linear operator. In such cases, the algorithm can be described by a matrix  $\mathbf{S} \in \mathbb{R}^{n \times m}$ . Several algebraic reconstruction algorithms, including the well-known ART, SART and SIRT algorithms [1], are linear methods.

We now focus on a single pixel  $c \in \{1, \dots, n\}$  of the reconstructed image. It has coordinates  $(x_c, y_c) \in \mathbb{R}^2$ . Denote the  $c$ th row of  $\mathbf{S}$  by  $\mathbf{s}^{(c)}$ . Each entry of  $\mathbf{s}^{(c)}$  corresponds to an entry in the vector  $\mathbf{p}$  of measured projection data, and therefore to a pair  $(\theta, \tau) \in \Theta \times \mathcal{T}$ , which we denote by  $s_{\theta\tau}^{(c)}$ . Let  $\mathbf{u} = \mathbf{S}\mathbf{p}$ . We then have

$$u_c = \sum_{\theta \in \Theta} \sum_{\tau \in \mathcal{T}} p_{\theta\tau} s_{\theta\tau}^{(c)}, \quad (4.3)$$

which is very similar to the filtered backprojection formula of Eq. (4.2). The vector  $\mathbf{s}^{(c)}$  can be computed by computing a series of reconstructions using a basis of unit vectors as input. For a given  $\theta \in \Theta$ , define  $t_c^{(\theta)} = x_c \cos \theta + y_c \sin \theta$ . Now define the function  $h^{(c)}(\theta, \cdot)$  by the following formula:

$$h^{(c)}(\theta, \tau) = s_{\theta(\tau + t_c^{(\theta)})}^{(c)}, \quad \text{for } \tau \in \mathcal{T} - t_c^{(\theta)}. \quad (4.4)$$

We refer to  $h^{(c)}$  as the *algebraic filter* for the algorithm  $\mathcal{S}$ . Note that  $h^{(c)}(\theta, \cdot)$  is only defined on a discrete domain. Intermediate values can be obtained by interpolation. Also note that the value  $h^{(c)}(\theta, \tau)$  can depend on the projection angle  $\theta$ . Just as in FBP, the algebraic filter determines the weight of the contribution of each detector position to the reconstructed value. For the selected pixel  $c$ , using the algebraic filter in FBP will result in an identical reconstructed value as for the linear algebraic method  $\mathcal{S}$ . It was demonstrated in [13] that if this same filter is also used to reconstruct all other image pixels, using the FBP

formula, an image is obtained that approximates the result of the linear algebraic reconstruction method very well.

### 4.3 AF-FBP WITH MULTIPLE FILTERS

In this section we describe a modified AF-FBP method where reconstructions of several filters are combined into one final reconstruction. As described in Section 4.2, we can create a filter for FBP based on any linear algebraic reconstruction method. This filter is created by computing a series of reconstructions (one for each detector element in the set  $T$ ), and storing the value of a single image pixel. The resulting filter depends on the choice of the image pixel. For the standard AF-FBP method the pixel in the center of the image grid is chosen (referred to as the central image pixel at location  $(x_c, y_c) \in \mathbb{R}^2$ ) to compute the filter. Afterwards, this filter can be applied to any vector  $\mathbf{p}$  of projection data, resulting in a reconstruction for which the central pixel has the same value as for the algebraic method.

In algebraic methods, the positioning of the reconstruction grid imposes implicit constraints on the reconstruction problem, namely that the reconstructed image is zero outside the region of the reconstruction grid. These constraints mainly affect the reconstruction near the boundary of the reconstruction grid. In general, these implicit constraints are beneficial to the quality of reconstructions computed by algebraic methods, as they limit the support of the reconstructed images to a subregion of  $\mathbb{R}^2$ . As a consequence, an object that is positioned in a corner of the reconstruction grid is not reconstructed identically (up to a shift) to an object that is positioned in the center of the grid. It is therefore natural to consider the question whether an algebraic filter computed for a pixel near a corner of the reconstruction grid is substantially different from the central filter, and whether it can provide more accurate reconstructions in this region. At the same time, using multiple filters for the reconstruction increases the implementation complexity of the reconstruction algorithm compared to FBP, as well as the computation time.

For the sake of simplicity, we limit our investigation here to the case where nine filters are used, obtained by dividing the image grid symmetrically in three columns and three rows. The central image pixel is also the center of one of these subregions. Since the size of

the image grid need not be divisible by three, the subregions need not be of equal size. The size of the subregion in the center of the image equals the image size divided by three. If this is not an integer, we use the smallest integer that is larger than this number. This integer is denoted by  $s$ . The pixels that are selected are located at  $(x_c \pm s, y_c \pm s)$ ,  $(x_c, y_c \pm s)$ ,  $(x_c \pm s, y_c)$ ,  $(x_c, y_c)$ . For each pixel a filter is created as described in Section 4.2.

According to Eq. (4.4), computing the filter for an image pixel  $j \in \{1, \dots, n\}$  with coordinates  $(x_j, y_j)$  requires the computation of the row  $s^{(j)}$  of the matrix  $\mathbf{S}$ . Subsequently, for each angle  $\theta$ , the part of  $s^{(j)}$  that corresponds with this angle is shifted over a distance  $t_j^{(\theta)} = x_j \cos \theta + y_j \sin \theta$ . Zero padding is applied for the filter values that fall outside the region where this shifted filter can be defined by interpolation.

After computation of the nine filters, each of these filters can be used in a standard FBP implementation. In this way we obtain nine reconstructions of the original image. The nine reconstructions can be combined in several ways to obtain a final reconstruction of the original image. In this chapter we explore two different ways to combine the reconstructions and we compare the reconstruction accuracy of both methods with the linear algebraic method, standard AF-FBP and FBP with the standard Ram-Lak filter.

## 4.4 EXPERIMENTS

In this section we describe a series of simulation experiments that we performed to examine the accuracy of the modified AF-FBP method.

### 4.4.1 *Phantoms*

The phantoms that are used in the experiments are shown in Fig. 4.1. Fig. 4.1a is a cross-section of a cylinder head in a combustion engine, Fig. 4.1b represents a cross-section of a wind turbine blade, Fig. 4.1c is the Shepp-Logan phantom which represents a simplification of a cross-section of a human brain [14], and Fig. 4.1d is a cross-section of a mandible.

The phantoms are defined on a square grid of  $2044 \times 2044$  pixels and are contained in the inscribed circle with diameter 2044 pixels. Real world objects can in general not be represented exactly on such a

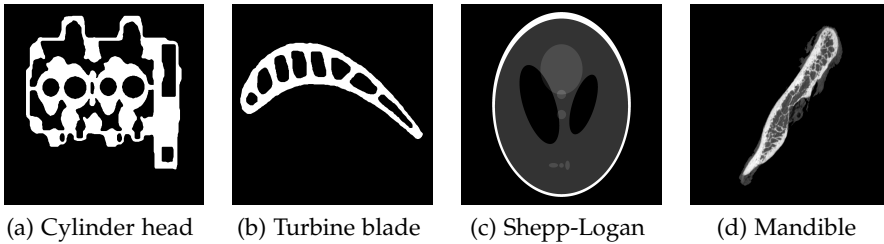


Figure 4.1: The phantoms.

pixel grid. To take this into account in our experiments, we reconstruct the phantoms on a coarser grid of  $511 \times 511$  pixels. To determine the reconstruction error we then refine the reconstruction to  $2044 \times 2044$  pixels by replacing every pixel in the coarse grid by a block of  $4 \times 4$  pixels with the same value.

As shown by experiments in [13], the quality of the reconstructions improves when the filters are created on a larger grid of  $767 \times 767$  pixels instead of  $511 \times 511$  pixels. Therefore, we use this larger grid to create the filters and to create the algebraic reconstructions. With error measures described in Section 4.4.4, we examine the reconstruction quality of the modified AF-FBP method.

#### 4.4.2 Projection data

The projection data are obtained using a parallel beam scanning geometry. The detector consists of 511 elements, each having a width of four image pixels. The Joseph's model is used to obtain the contribution of each image pixel to an individual projection ray [15]. Per detector element we use four rays, each having a width of one image pixel. This ensures that every image pixel contributes with nonzero weight to at least one ray per projection angle. The projection angles are equiangularly distributed within the full range of 180 degrees. The number of projection angles  $d$  varies during the experiments.

### 4.4.3 Reconstruction methods

In the experiments we use four different reconstruction methods to obtain the reconstructions. All algebraic filters are based on the iterative SIRT algorithm. In particular, the following algorithms are compared:

**SIRT** Simultaneous Iterative Reconstruction Method. The  $k$ th iteration  $\mathbf{u}^{(k)}$  is given by Eq. (4.5), where  $\mathbf{u}^{(0)} = \mathbf{0}$ .

$$\mathbf{u}^{(k+1)} = (\mathbf{I}_n - \omega \mathbf{C} \mathbf{W}^T \mathbf{R} \mathbf{W}) \mathbf{u}^{(k)} + \omega \mathbf{C} \mathbf{W}^T \mathbf{R} \mathbf{p}, \quad (4.5)$$

where  $\mathbf{C} = (c_{ij}) \in \mathbb{R}^{n \times n}$  and  $\mathbf{R} = (r_{ij}) \in \mathbb{R}^{m \times m}$  are diagonal matrices given by  $c_{jj} = \alpha(\sum_{i=1}^n |w_{ij}|)$  and  $r_{ii} = \beta(\sum_{j=1}^m |w_{ij}|)$  respectively,  $\mathbf{I}_n \in \mathbb{R}^{n \times n}$  denotes the identity matrix, and  $\omega$  is a relaxation parameter [8, 16]. In this chapter we set  $\omega = 1$ ,  $\alpha(x) = \beta(x) = 1/x$  for  $x \in \mathbb{R}$ . We stop the SIRT algorithm after a fixed number of 200 iterations.

**FBP-RL** Filtered Backprojection method given by Eq. (4.2) using the standard Ram-Lak filter.

**SIRT-FBP SF** SIRT-FBP ‘Single Filter’; this is the standard SIRT-FBP method using one angle-dependent filter based on the central pixel of the reconstruction grid; see Section 4.2.

**SIRT-FBP IR** SIRT-FBP ‘Isolated Regions’; this is a variation on SIRT-FBP using nine pixels to calculate nine angle-dependent filters. The selection of these nine pixels is described in Section 4.3. For each filter a reconstruction is created using FBP with this filter. The subregion containing the pixel that was used to create the filter is used for the final reconstruction. These subregions do not overlap and will be referred to as isolated regions. The collection of all these isolated subregions forms a complete reconstruction.

**SIRT-FBP BI** SIRT-FBP ‘Bilinear Interpolation’; for this method we use the same subregions as for IR, but we perform an additional bilinear interpolation step instead of only collecting the isolated subregions.

#### 4.4.4 Error measure

The accuracy of the reconstruction methods is examined using two different error measures. The first measure is obtained by calculating the sum of absolute pixel differences between the reconstruction and the original object. After normalization, the resulting error is denoted as the *mean reconstruction error*  $E_r$ . Since the reconstruction has a coarser grid than the original image, we cannot compare them directly. We first select in the  $767 \times 767$  reconstruction grid the smaller  $511 \times 511$  pixel grid with the same central pixel as the reconstruction grid. We then enlarge this grid by replacing every pixel by a block of  $4 \times 4$  pixels with the same value to obtain a grid of  $2044 \times 2044$  pixels. We denote this image by  $\hat{\mathbf{u}} = (\hat{u}_{ij}) \in \mathbb{R}^{n^2}$  with  $n = 2044$  and the original phantom by  $\mathbf{v} = (v_{ij}) \in \mathbb{R}^{n^2}$ . The mean reconstruction error is then defined by

$$E_r = \frac{\sum_{i,j} |\hat{u}_{ij} - v_{ij}|}{\sum_{i,j} v_{ij}}. \quad (4.6)$$

The second measure is obtained by calculating the sum of absolute pixel differences between the reconstruction  $\mathbf{u} = (u_{kl})$  and the algebraic reconstruction  $\mathbf{u}^{\text{ARM}} = (u_{kl}^{\text{ARM}})$  on the same grid of  $511 \times 511$  pixels that was used in the mean reconstruction error before refining it. After normalization this error is denoted as the *mean ARM reconstruction error*  $E_r^{\text{ARM}}$ , defined by

$$E_r^{\text{ARM}} = \frac{\sum_{k,l} |u_{kl} - u_{kl}^{\text{ARM}}|}{\sum_{k,l} u_{kl}^{\text{ARM}}}. \quad (4.7)$$

#### 4.4.5 Series of experiments

The reconstructions are compared in three series of experiments.

In the first series of experiments the number of projection angles is varied. We show the resulting mean reconstruction errors  $E_r$ , as well as the mean ARM reconstruction errors  $E_r^{\text{ARM}}$ , for all four phantoms and using several different interpolation methods for the filters. The

aim of this series is to compare the accuracy of the five reconstruction methods for a varying number of projections ( $d \in \{16, 24, 32, 64\}$ ).

In the second series of experiments we apply varying amounts of Poisson noise to the projection data. FBP with a Ram-Lak filter is known to produce poor quality reconstructions if the projection data has a low signal-to-noise ratio, while SIRT provides superior results for such data. We examine the reconstruction quality of SIRT-FBP with multiple filters, compared to SIRT, FBP-RL and standard SIRT-FBP.

In the third series of experiments a larger detector is used to obtain the projections and to create the filters. As discussed in Section 4.3, a shift operation has to be applied when computing an algebraic filter for a non-central image pixel. If such an image pixel is near the boundary of the reconstruction region, then substantial zero-padding is needed for some angles on one side of the shifted filter. Enlarging the size of the detector (and hence the size of the filter), decreases the number of zeros that has to be inserted. A disadvantage is the larger computation time to create the filter. In this series of experiments we examine the effect of using these larger filters on the reconstruction quality.

## 4.5 RESULTS

In this section we present the results of the experiments described in the previous section. We start with discussing the algebraic filters for the different selected image pixels and show their effect on the reconstructions. Then we compare the reconstructions of SIRT-FBP with multiple filters with reconstructions of both the standard SIRT-FBP and FBP-RL.

### 4.5.1 Filter dependence on the selected pixel

The algebraic filters depend quite strongly on the pixel that is used to create them. Each image in Fig. 4.2 provides a visual representation of a particular row  $s^{(j)}$  of the matrix  $\mathbf{S}$ , where the vertical axis corresponds with the projection angle and the horizontal axis corresponds with the position on the detector. The selected pixels  $p_1, \dots, p_9$  are numbered row-wise, starting at the top left corner with  $p_1$ .

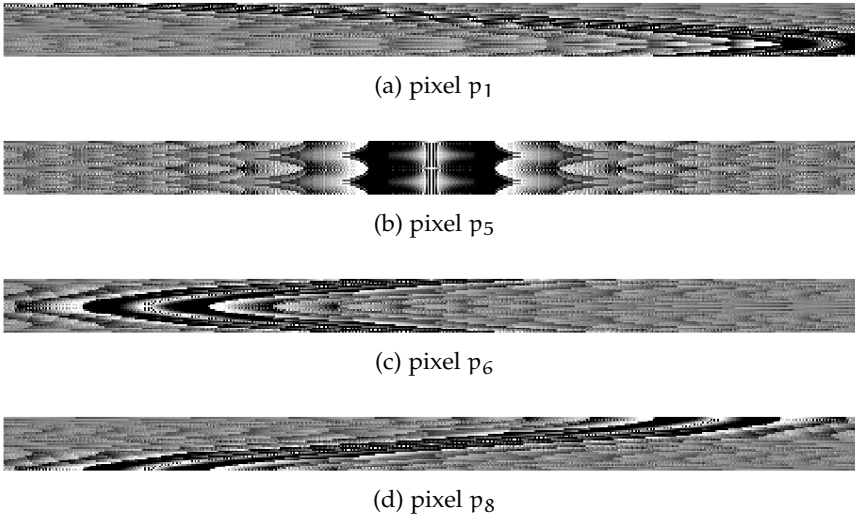


Figure 4.2: Visual representations of rows of the matrix  $S$  for  $d = 32$  projection angles.

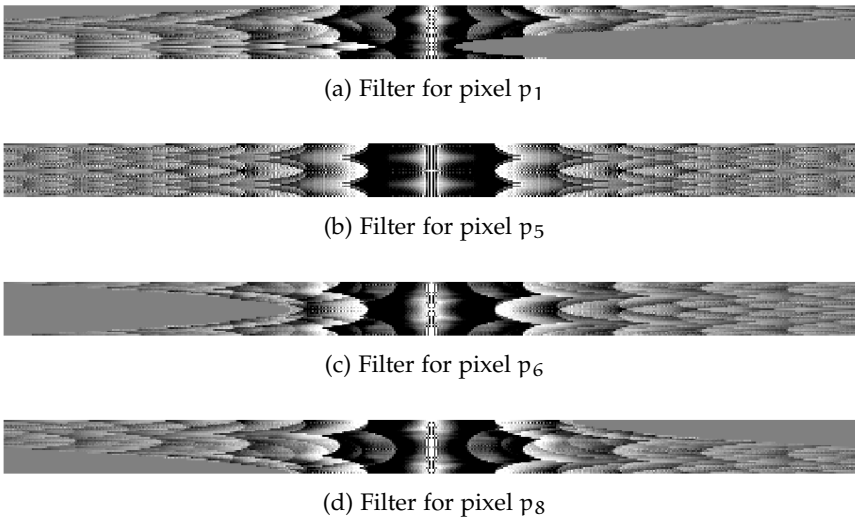


Figure 4.3: Filters for  $d = 32$  projection angles after linear interpolation and shifting.

Fig. 4.3 shows the corresponding filters that are the result of Eq. 4.4, after applying a linear interpolation and angle-dependent shifting of



the images in Fig. 4.2. The large homogeneous grey areas arise due to the necessary zero-padding to obtain a filter of size 511 after shifting. These areas might have a large influence on the resulting reconstructions. To examine this influence, we also include experiments for a larger filter of 767 elements. Since this gives rise to a larger system of equations  $\mathbf{W}\mathbf{x} = \mathbf{p}$ , the algebraic reconstructions will change as well. The corresponding filters will therefore not only contain fewer zero elements, but are different from the filters in Fig. 4.3 in the nonzero entries as well. The results are shown in Section 4.5.4.

In Fig. 4.4 the reconstructions are shown for the nine different angle-dependent filters with  $d = 32$ . These reconstructions are combined into a final reconstruction using either the filters corresponding to the central pixel (denoted by SF), or to the collection of isolated subregions (denoted by IR), or to a bilinear interpolation of the isolated regions (denoted by BI), as discussed in Section 4.4.3.

#### 4.5.2 *Varying the number of projection angles*

In the first series of experiments the four phantoms are reconstructed using different numbers of projection angles. The projection data are noiseless in these experiments. Fig. 4.6 shows the mean reconstruction errors for the turbine blade phantom.

The mean reconstruction error of both standard SIRT-FBP and modified SIRT-FBP is very close to the error of SIRT. The variation SIRT-FBP with bilinear interpolation outperforms SIRT-FBP with isolated regions. This is expected behavior, since bilinear interpolation uses the values of a pixel in two or more reconstructions, which results in a smoothing of the presumed larger pixel errors near the boundary of the isolated regions. Therefore, we expect the mean reconstruction error,  $E_r$ , to be smaller than that of SIRT-FBP with isolated regions. Furthermore, we observe that standard SIRT-FBP results in reconstructions that are slightly more accurate than SIRT or SIRT-FBP with multiple filters. FBP-RL is substantially less accurate than the other reconstruction methods considered here.

The standard SIRT-FBP method uses only a single filter based on the central pixel. These results therefore show that the local use of filters based on pixels other than the central pixel does not reduce the mean (ARM) reconstruction error. This might be due to the fact that

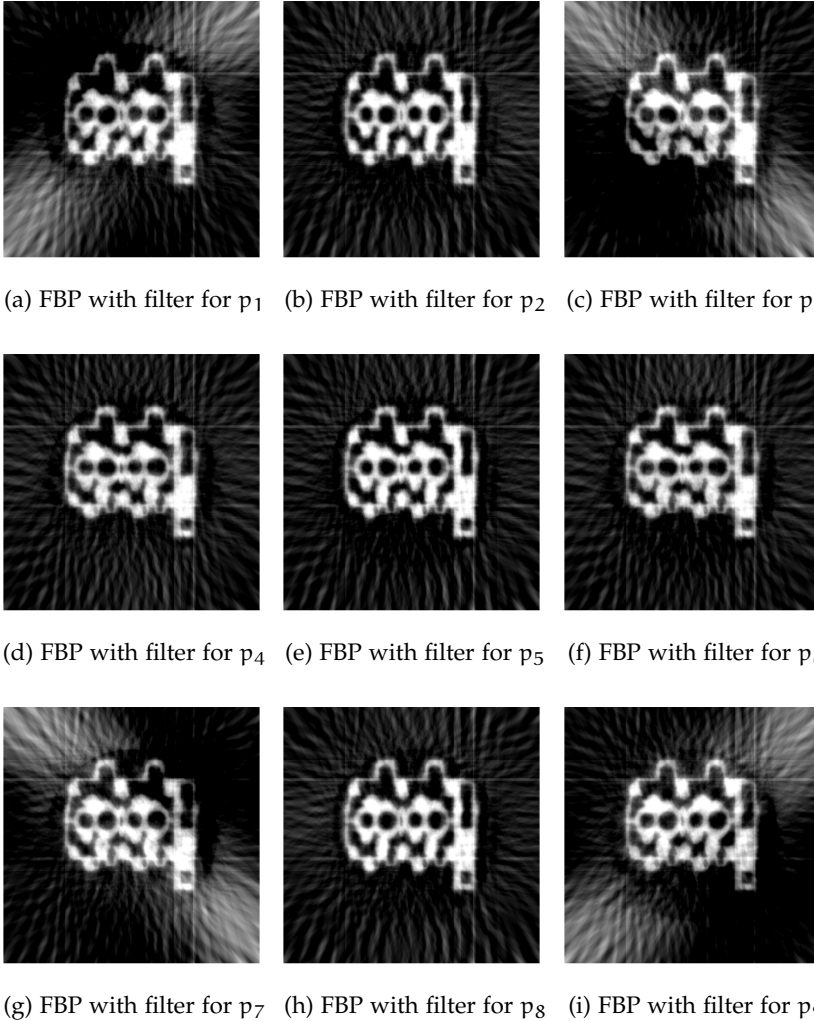


Figure 4.4: Reconstructions of the cylinder head phantom using the filters based on the nine different image pixels.

shifting and zero-padding of these filters is required before they can be applied to the projection data, resulting in the loss of some accuracy in the approximation of the ARM due to the additional interpolation step.

SIRT-FBP with bilinear interpolation is not only more accurate than SIRT-FBP with isolated regions, it is also a better approximation of

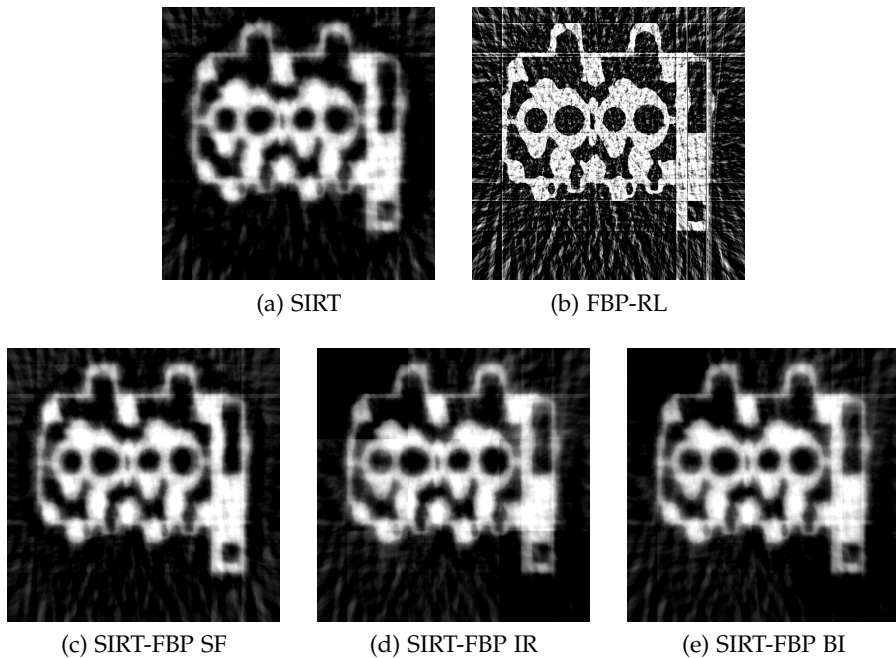


Figure 4.5: Reconstructions of the cylinder head phantom with  $d = 32$ ; (a) SIRT reconstruction using 200 iterations; (b) FBP with Ram-Lak filter; (c) SIRT-FBP with the filters corresponding to the central pixel; (d) SIRT-FBP combining the nine reconstructions from isolated regions; (e) SIRT-FBP combining the nine reconstructions using bilinear interpolation.

SIRT. Its mean ARM reconstruction error is only slightly larger than that of standard SIRT-FBP. The mean ARM reconstruction error of SIRT-FBP with isolated regions is larger than that of standard SIRT-FBP and SIRT-FBP with bilinear interpolation. However, it is still much smaller than that of FBP-RL.

Furthermore, we observe that the reconstruction errors are almost indifferent to the method chosen to interpolate the filter. Every row in Fig. 4.6 shows the reconstruction error for a different interpolation method. We will therefore not include the results of the different interpolation methods in the remainder of this chapter and only show the results using the linear interpolation method for the filters. These results for the other three phantoms are shown in Fig. 4.7. The left-hand side column shows the same pattern as for the turbine blade.

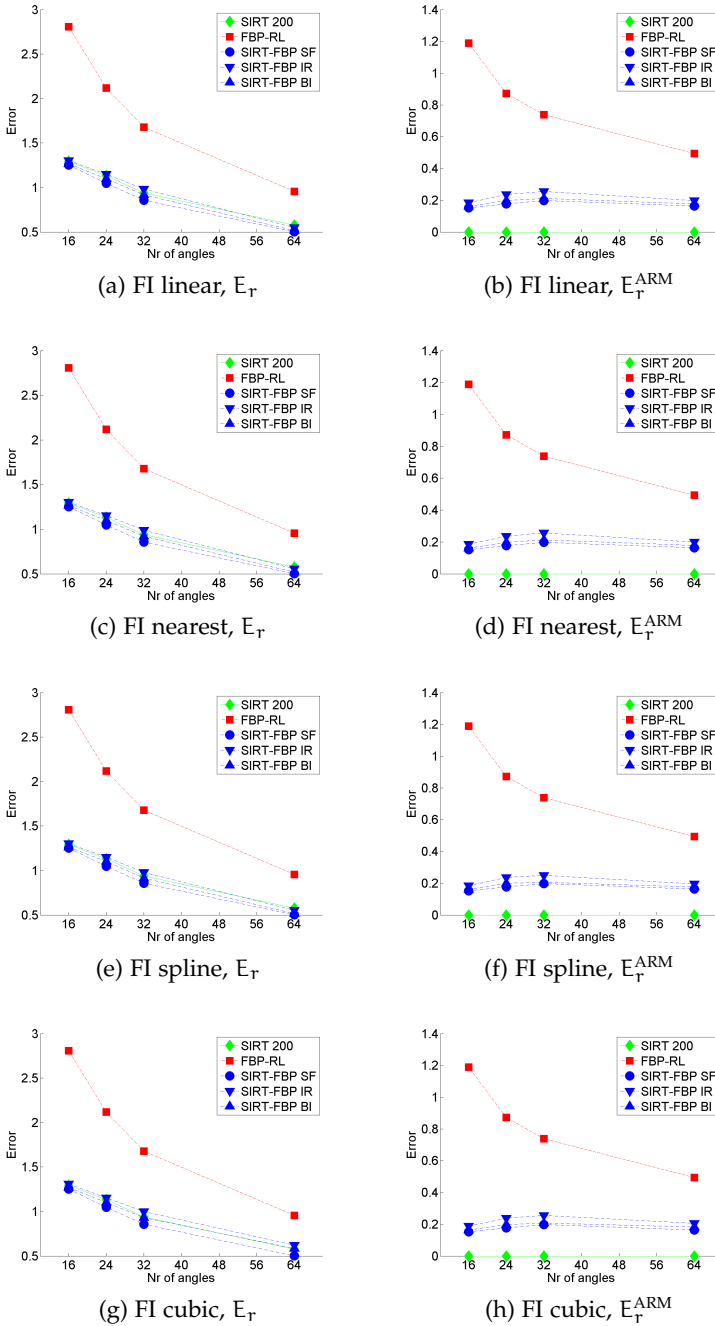


Figure 4.6: Mean (ARM) reconstruction error  $E_T$  ( $E_T^{\text{ARM}}$ ) for the turbine blade phantom. Several interpolation methods are used to compute the filters; SF = single filter, IR = isolated regions, BI = bilinear interpolation.

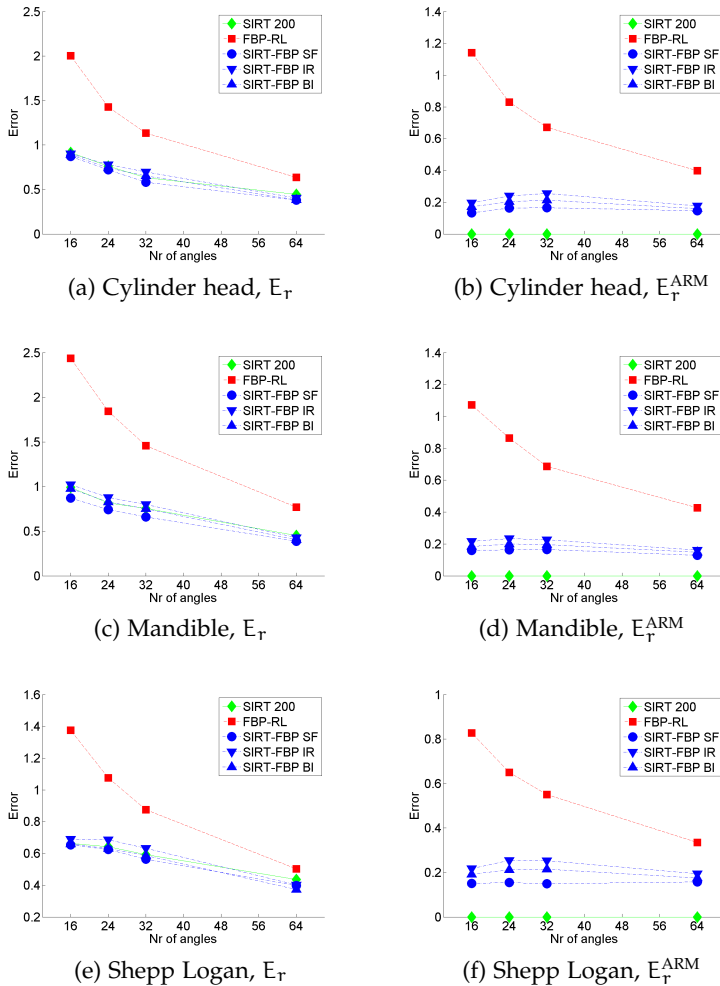


Figure 4.7: Mean reconstruction error  $E_T$  of the cylinder head phantom (top row), mandible phantom (middle row), Shepp Logan phantom (bottom row). Linear interpolation is applied to compute the filters. SF = single filter, IR = isolated regions, BI = bilinear interpolation.

The mean ARM reconstruction errors for SIRT-FBP with bilinear interpolation are again smaller than for SIRT-FBP with isolated regions. In all cases, the reconstructions computed using algebraic filters are more accurate than for FBP-RL.

### 4.5.3 Poisson noise

In the second series of experiments we apply Poisson noise to the projection data, by simulating the Poisson distribution based on a varying number of photons used for the beam profile. The lower this photon count, the higher the noise level. The results for varying noise levels are shown in Fig. 4.8 and Fig. 4.9.

It can be observed in Fig. 4.8 that FBP-RL cannot handle noisy projection data very well. The mean reconstruction errors for high amounts of noise are large compared to those for SIRT-FBP and SIRT. The right-hand side column of both figures is a detail of the figures on the left-hand side. In this detail we observe that SIRT-FBP performs slightly better in terms of the mean reconstruction error than SIRT. This is consistent with observations in [13] for  $d = 64$ . It can also be observed for the other numbers of projection angles. Furthermore, assembling the modified SIRT-FBP reconstruction using isolated regions or bilinear interpolation reduces  $E_r$  for high amounts of noise. The local reconstructions using filters corresponding to the selected pixels  $p_1, p_3, p_7$  and  $p_9$  contain less noisy reconstructions in the area around the selected pixel. Since only this area is used while assembling the final reconstruction, this might explain the smaller  $E_r$ . For less noisy projection data, the standard SIRT-FBP method based on one angle-dependent filter performs equally well or better than the modified SIRT-FBP method, depending on the number of projection angles.

In Fig. 4.9 the results are shown for  $d = 32$  and  $d = 64$ . The mean ARM reconstruction errors  $E_r^{\text{ARM}}$  with  $d = 16$  and  $d = 24$  are similar to those for  $d = 32$  and therefore not included in this chapter. The reconstructions of the standard SIRT-FBP (with one angle-dependent filter) differ less from SIRT than SIRT-FBP with multiple angle-dependent filters. We do observe that bilinear interpolation results in reconstructions that are closer to the SIRT reconstructions than using isolated regions.

All results for the cylinder head are representative for the other three phantoms. The results for the other phantoms are therefore not included in this chapter.

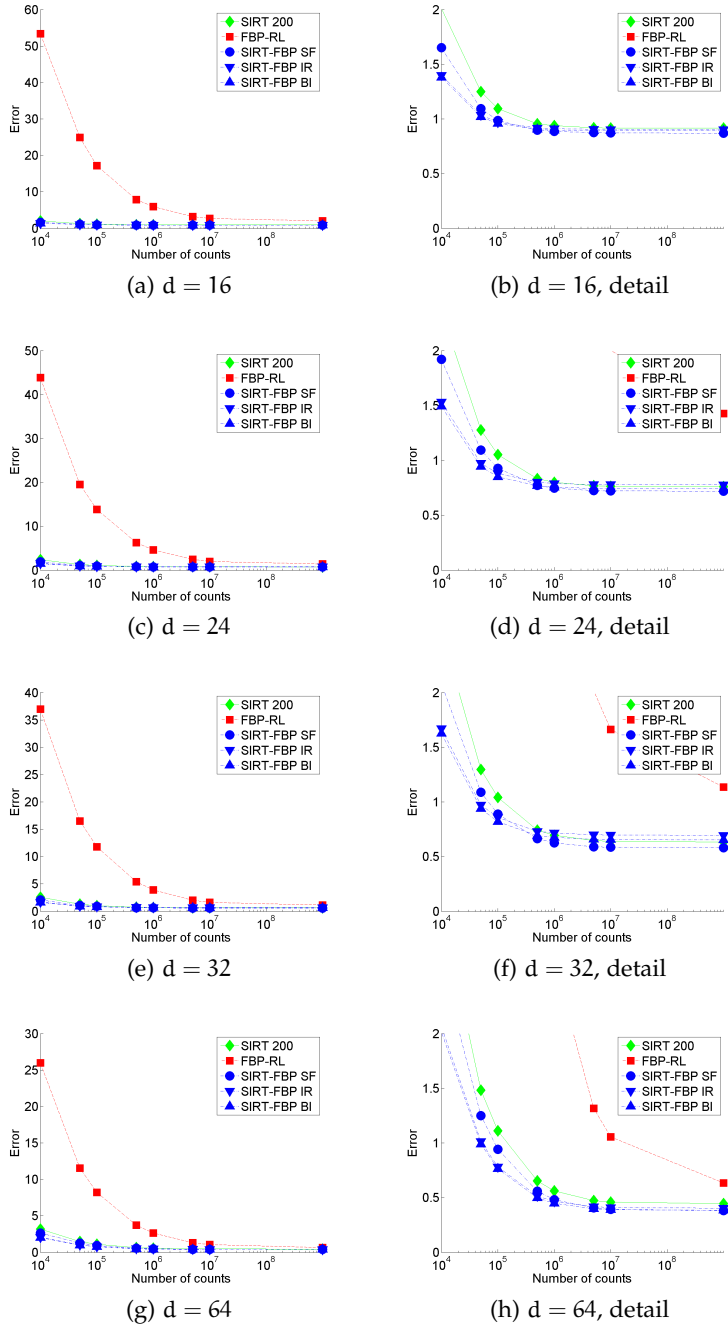


Figure 4.8: Mean reconstruction error  $E_T$  of the cylinder head phantom for varying amounts of noise applied to the projection data. Linear interpolation is applied to compute the filters. SF = single filter, IR = isolated regions, BI = bilinear interpolation.

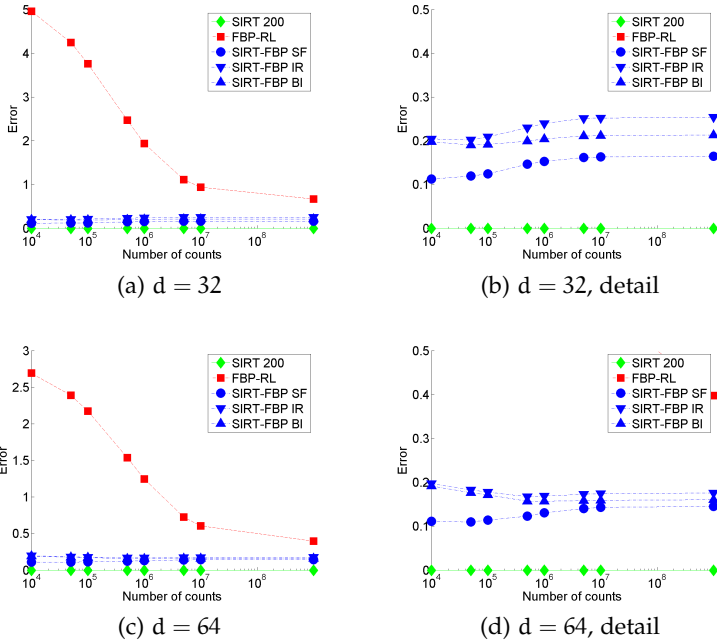


Figure 4.9: Mean ARM reconstruction error  $E_{\tau}^{\text{ARM}}$  of the cylinder head phantom for varying amounts of noise applied to the projection data. The rows correspond to different numbers of projection angles  $d$ . Linear interpolation is applied to compute the filters. SF = single filter, IR = isolated regions, BI = bilinear interpolation.

#### 4.5.4 Varying the size of the detector

In the third series of experiments we increase the size of the detector from 511 elements to 767 elements. The filters that cover the reconstruction grid of  $511 \times 511$  pixels need less zero-padding. Several filters are shown in Fig. 4.10.

The reconstruction errors using these larger filters are shown in Fig. 4.11. We compare them with the results for the smaller filters in Fig. 4.6. We observe that both  $E_{\tau}$  and  $E_{\tau}^{\text{ARM}}$  of SIRT-FBP are less affected by the method chosen to assemble the reconstruction than for the smaller filters with a support of 511 elements. The value of  $E_{\tau}$  is comparable in both cases. The right-hand side column of the figure shows that the reconstructions using a detector of 767 elements are more similar to



(a) Filter for pixel  $p_1$ (b) Filter for pixel  $p_5$ (c) Filter for pixel  $p_6$ (d) Filter for pixel  $p_8$ 

Figure 4.10: Larger filters with 767 elements per angle for  $d = 32$  projection angles.

the SIRT reconstructions than those using a smaller detector of 511 elements, although the differences are small.

The results for different interpolation methods used in the computation of the filter and for different phantoms are similar to those discussed above and are omitted here.

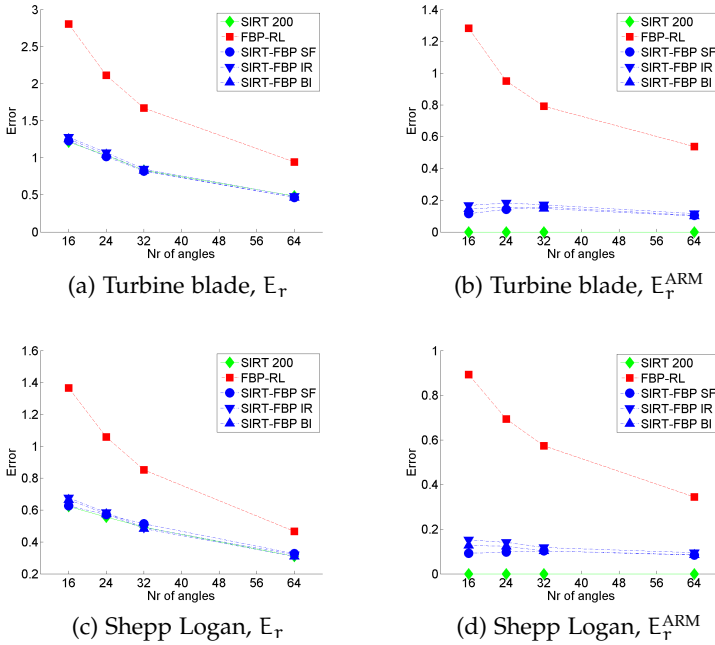


Figure 4.11: Mean (ARM) reconstruction error  $E_T$  ( $E_T^{\text{ARM}}$ ) for filters with 767 elements per angle, for varying number of projection angles. Linear interpolation is applied to compute the filters. SF = single filter, IR = isolated regions, BI = bilinear interpolation.

#### 4.6 DISCUSSION

Our experimental results suggest that the standard SIRT-FBP method approximates SIRT better than SIRT-FBP with nine algebraic filters. An interesting result is obtained in the case where we apply high amounts of Poisson noise to the projection data and compare the reconstructions with the phantom instead of with the SIRT reconstruction. In this case, the reconstructions of SIRT-FBP with bilinear interpolation are more accurate than the standard SIRT-FBP reconstructions and the FBP-RL reconstructions. Although it is not the aim of the AF-FBP method to improve the accuracy of the reconstructions, since there we want to approximate the ARM as best as possible, it opens new opportunities for further research.

The value of the pixel that was used to create the filter for SIRT-FBP is the same in both the SIRT reconstruction and the SIRT-FBP reconstruction. We can therefore view SIRT as an SIRT-FBP with an algebraic filter calculated for every image pixel. Hence we have compared the reconstruction accuracy of SIRT-FBP with one, with nine and with  $511 \times 511$  algebraic filters. The results show that for high amounts of Poisson noise the reconstruction accuracy of SIRT-FBP with nine algebraic filters outperforms that of SIRT-FBP with both one algebraic filter and with  $511 \times 511$  algebraic filters. Assuming that the reconstruction accuracy of SIRT-FBP depends smoothly on the number of algebraic filters, there should be an optimal number of algebraic filters that maximizes the reconstruction accuracy of SIRT-FBP. Also the position of the selected pixels in the image grid can influence this accuracy and should be examined in more detail.

#### 4.7 CONCLUSIONS

In this chapter we have investigated an approach to create algebraic filters (AFs) that can be used in the Filtered Backprojection method. Reconstructions of the standard AF-FBP method can be computed using the same computation time as FBP, while they resemble the reconstruction properties of the linear algebraic reconstruction method that was used to create the filter. Compared to the original AF-FBP method, which is based on a single filter, the approach proposed in this chapter is based on computing multiple filters, each covering a region of the reconstruction grid. For each (angle-dependent) filter we calculate an FBP reconstruction. Parts of these reconstructions are combined into a final reconstruction by either assembling separate regions or by using bilinear interpolation for neighboring regions from each reconstruction. In a series of simulation experiments, we examined the reconstruction accuracy of these variations by comparing the reconstructions with both the phantoms and the corresponding algebraic reconstructions, based on the SIRT algorithm.

For the sake of clarity, we focused on a particular scenario where nine filters are created, each based on a different pixel in the reconstruction grid. The resulting reconstructions show little dependence on the different interpolation methods that can be applied to compute the filters. Since in the creation of some filters substantial zero-padding

is required, we also created filters with an extended support to reduce this zero-padding. This results in only a small effect on the quality of the corresponding reconstructions, while it increases the computation time of the filters.

Assembling the final reconstruction using bilinear interpolation results in general in a more accurate reconstruction than combining separate regions. The differences between standard AF-FBP and AF-FBP based on multiple filters are small and in many situations the standard AF-FBP method outperforms the suggested variations. There are situations, such as projection data with few angles and a high amount of noise, where modified AF-FBP using bilinear interpolation outperforms standard AF-FBP when we compare the reconstructions with the original phantoms. In general however we observe that using more than one angle-dependent filter does not automatically lead to a better approximation of the corresponding algebraic method, or in a more accurate reconstruction method.

Our findings suggest that for the AF-FBP method, the central pixel is actually a very good choice for computing the filter, even if this filter is then applied to reconstruct image pixels in the outer regions of the reconstruction grid.

## BIBLIOGRAPHY

- [1] A. C. Kak and M. Slaney. *Principles of Computerized Tomographic Imaging*. Philadelphia: SIAM, 2001.
- [2] G. T. Herman. *Fundamentals of Computerized Tomography: Image Reconstruction from Projections*. Berlin: Springer, 2009.
- [3] T. M. Buzug. *Computed Tomography: From Photon Statistics to Modern Cone-Beam CT*. Berlin: Springer, 2008.
- [4] A. Markoe. *Analytic Tomography*. New York: Cambridge University Press, 2006.
- [5] X. Pan, E. Y. Sidky, and M. Vannier. Why do commercial CT scanners still employ traditional, filtered back-projection for image reconstruction? *Inv. Problems* 2009; 25(12): 123009.
- [6] L. A. Feldkamp, L. C. Davis, and J. W. Kress. Practical cone-beam algorithm. *J. Opt. Soc. Am.* 1984; 1(A6): 612–619.
- [7] A. H. Andersen and A. C. Kak. Simultaneous Algebraic Reconstruction Technique (SART): a superior implementation of the ART algorithm. *Ultrasound. Imag.* 1984; 6(1): 81–94.
- [8] J. Gregor and T. Benson. Computational analysis and improvement of SIRT. *IEEE Trans. Med. Imag.* 2008; 27(7): 918–924.
- [9] A. K. Louis and Th. Schuster. A Novel Filter Design Technique in 2D - Computerized Tomography. *Inverse Problems* 1995.
- [10] H. Kunze et al. Filter determination for Tomosynthesis aided by iterative reconstruction techniques. *Proc. of Fully3D* 2007: 309–312.
- [11] J. Ludwig et al. A Novel Approach for Filtered Backprojection in Tomosynthesis Based on Filter Kernels Determined by Iterative Reconstruction Techniques. *Proc. of IWDM* 2008; 5116: 612–620.
- [12] J. Hsieh Y. Wei G. Wang. An intuitive discussion on the ideal ramp filter in computed tomography (I). *J. Comput. Math. Appl.* 2005; 49(5–6): 731–740.
- [13] K. J. Batenburg and L. Plantagie. Fast Approximation of Algebraic Reconstruction Methods for Tomography. *IEEE Trans. Image Process.* 2012; 21(8): 3648–3658.

- [14] L. A. Shepp and B. F. Logan. The Fourier reconstruction of a head section. *IEEE Trans. Nucl. Science* 1974; 21(3): 21–43.
- [15] P.M. Joseph. An improved algorithm for reprojecting rays through pixel images. *IEEE Trans. Med. Imag.* 1982; 1(3): 192–196.
- [16] P. Gilbert. Iterative methods for the three-dimensional reconstruction of an object from projections. *J. Theor. Biol.* 1972; 36(1): 105–117.

---

## ALGEBRAIC FILTER APPROACH FOR FAST APPROXIMATION OF NONLINEAR TOMOGRAPHIC RECONSTRUCTION METHODS

---

**Abstract** – In this chapter we present a computational approach for fast approximation of nonlinear tomographic reconstruction methods by filtered backprojection methods. Algebraic reconstruction algorithms are the methods of choice in a wide range of tomographic applications, yet they require significant computation time, restricting their usefulness. We build upon recent work on the approximation of *linear* algebraic reconstruction methods and extend the approach to the approximation of nonlinear reconstruction methods, which are common in practice. We demonstrate that if a blueprint image is available that is sufficiently similar to the scanned object, our approach can compute reconstructions that approximate iterative nonlinear methods, yet have the same speed as filtered backprojection.

---

This chapter has been published with minor modification as: L. Plantagie and K. J. Batenburg. Algebraic filter approach for fast approximation of nonlinear tomographic reconstruction methods. *J. Electron. Imaging* 2015; 24(1). 013026. This publication is available through <http://dx.doi.org/10.1117/1.JEI.24.1.013026>. Copyright 2015 Society of Photo-Optical Instrumentation Engineers. One print or electronic copy may be made for personal use only. Systematic reproduction and distribution, duplication of any material in this paper for a fee or for commercial purposes, or modification of the content of the paper are prohibited.

## 5.1 INTRODUCTION

Computed Tomography (CT) deals with the reconstruction of an object from a series of projections of this object, taken along a range of angles [1–4]. Depending on the application, projection images are typically acquired by a scanning device, using a photon or particle beam that is transmitted through the object (e.g. X-rays, electrons, neutrons). Besides extensive applications in medical imaging, tomography is a common technique in many other fields in academia (materials science, micro-biology) as well as industry (quality inspection, process monitoring) [5–9].

In this chapter we focus on the reconstruction phase of the tomography pipeline, where an image of the original object is computed from the projections by a reconstruction algorithm. The characteristics of the reconstructed image depend not only on the set of input projection data, but also on the reconstruction algorithm employed. A range of reconstruction methods have been proposed in the literature, each having strong and weak points with respect to reconstruction quality, reconstruction time, and robustness [2, 10–13]. The reconstruction methods that are used often in practice can be divided into two categories: analytical methods and algebraic methods. Here, we use the term "algebraic methods" to refer to the category of algorithms that converge to a least-squares solution (e.g. the Simultaneous Iterative Reconstruction Technique (SIRT)), as well as the category of statistical methods such as the Expectation Maximization (EM) algorithm.

In the ideal situation, where the reconstruction problem can be represented by a continuous set of data, we can find an exact solution of the reconstruction problem using an analytical method. This method uses an inversion formula to obtain the analytical solution. By discretizing this inversion formula, a reconstruction algorithm is obtained that approximates the analytical result. Typically, such methods are based on the assumption that the projections can be sampled continuously and a full range of angles are available. In practice, interpolation techniques must be used to account for missing projection data [1].

The Filtered Backprojection (FBP) algorithm – and its many variants – is the most prominent example of an analytical reconstruction method. Due to its computational efficiency, ease of implementation, and high accuracy if sufficient data is available, FBP is extensively used in practice [14]. Reconstructions are obtained by convolution of the



projection data with a filter, followed by a so-called backprojection step. The filter can be customized and affects the quality of the reconstruction. FBP is capable of computing accurate reconstructions if a large number of low-noise projections are available, sampled along the full angular range. For reconstruction tasks involving just a small number of projections, or limited-angle datasets, FBP reconstructions are typically plagued by serious artefacts which hamper image interpretation .

Algebraic methods solve a system of linear equations, which represents the discretized tomographic reconstruction problem. This equation system directly models the finite set of projections available in the actual scan, resulting in a very large and sparse matrix describing the equations. The computation time required to calculate a least squares solution is so high, that in practice iterative methods are used for its solution [1]. The algebraic reconstruction methods are known to produce more accurate reconstructions than FBP when few projections are available or with noisy data. A key drawback of these methods is their high computational cost.

A subclass of the algebraic reconstruction methods consists of the linear algebraic reconstruction methods (LARMs). An algebraic reconstruction method is linear if the algorithm acts on the projection data as a linear operator. Examples of LARMs are ART, SART and SIRT [3].

In [15], a method was introduced to create filters for FBP that are based on the operation of linear algebraic reconstruction methods. The reconstructions of FBP with these filters approximate reconstructions of the corresponding algebraic reconstruction methods. This method is known as Algebraic Filter FBP (AF-FBP). Using these filters, one can approximate the accuracy of algebraic reconstruction methods while at the same time attaining the computational efficiency of FBP. The construction of the filters is computationally intensive, but needs to be performed only once for a given set of geometrical parameters (i.e. number of projections and their corresponding angles). The filters do not depend on the object that is being reconstructed. An important limitation of the method for constructing these filters is that the underlying algebraic reconstruction method (ARM) is required to be linear.

Other methods have been proposed in literature to create filters for FBP [16–19]. There are two different approaches; creating filters based on theoretical derivations which are suited for every geometry, [16, 17] and creating filters based on the geometry [18, 19]. The AF-FBP met-

hod belongs to this second group. Like the filters in [19], an iterative reconstruction method is used to obtain the filters. An important difference between these two methods is that in [19] an object consisting of three thin rods is used in the calculations of the filters, while AF-FBP for LARMs is object-independent.

Many common iterative tomographic reconstruction methods do not meet the linearity condition. Therefore, they cannot be approximated directly by the AF-FBP. Examples of these methods are *conjugate gradient least squares* (CGLS), and the statistical reconstruction method *expectation maximization* (EM) [20–22]. The CGLS algorithm is mildly nonlinear, in the sense that the algorithm becomes a LARM as the number of iterations tends to infinity. In tomography, only a relatively small number of iterations are typically performed, not only for limiting the computation time but also due to the regularizing effect embedded in the method itself. The Expectation Maximization algorithm (EM) maximizes the log likelihood function of the reconstructed image for a given set of projection data, assuming that the observed data and the Radon transform of the object are related by a Poisson distribution. Such statistical reconstruction methods are known to yield superior reconstructions to LARMs if the projection data contains a high level of (Poisson distributed) noise [23].

Even though each of the reconstruction methods mentioned above yields a different reconstruction, the forward operator in the underlying inverse problem solved by these methods is still a linear operator (i.e. a discretized Radon transform). We therefore intuitively expect that many nonlinear algebraic reconstruction methods (NLARMs) can *locally* be approximated by a linear method. By the term "locally" we refer here to the case where the reconstruction of a similar image, called a *blueprint*, is already available and only the difference of the projections compared to this known image needs to be reconstructed. Hence we refer not to spatial locality in the image, but to locality in the space of images, where each image is considered as a point in a high-dimensional vector space.

In this chapter we adapt the AF-FBP approach to approximate NLARMs that have this locally linear behavior, such that AF-FBP can still be applied in cases where a blueprint object is available. We present the results of a series of experiments performed to assess the nonlinearity present in the CGLS and EM methods. We subsequently examine the reconstruction quality of our adapted AF-FBP method

and compare them with reconstructions obtained by applying the NLARM directly.

The ability to compute fast approximations of NLARM reconstructions is useful in cases where the object to be reconstructed is expected to contain (small) variations with respect to the blueprint, which is known in advance. Such cases can be found, for example, in the field of nondestructive testing and inspection. Our approach is based on the computation of an *algebraic filter* that depends on the blueprint image. This processing step is computationally demanding, as it involves a series of runs of the iterative algebraic method. Once the filter has been computed, new images can be reconstructed with the same speed as Filtered Backprojection. Our method will mainly be useful in scenarios where a large number of similar objects are scanned in sequence, and where algebraic methods are required due to limitations in the scanning geometry or scanning time. In such cases, the approach enables the approximation of advanced algebraic methods, while still maintaining a low computation time, sufficient for real-time reconstruction.

The concept of replacing the full reconstruction problem by the task of reconstructing the difference from a blueprint object has been used in various nonlinear inverse problems in imaging (e.g. seismic inversion [24] and electrical impedance tomography) but is applied here for the first time to fast approximation of nonlinear tomographic reconstruction methods, thereby considerably extending the applicability of AF-FBP.

This chapter is structured as follows. In Sect. 5.2 the algorithms are briefly discussed and notation is introduced. The AF-FBP method for linear algebraic reconstruction methods is briefly introduced in Sect. 5.3.1. In Sect. 5.3.2, we extend the AF-FBP approach to NLARMs. In Sect. 5.4 we describe the setup and results of a series of computational experiments, comparing the proposed AF-FBP method to other methods. We conclude with discussion and conclusions in Sect. 5.5.

## 5.2 PRELIMINARIES

In this chapter, the projection data are obtained using a source and detector that rotate around the object in the 2D plane. We use *parallel beams* that cover all image pixels for each projection angle. The approach presented here is not limited to the scanning geometry described

here, but can be applied to other scanning geometries as well (e.g. fan-beam, cone-beam). An additional rebinning step of the projection data is necessary for these geometries. First, we give a brief introduction to the concepts and notation of FBP, followed by a description of the key algebraic methods studied in this chapter.

### 5.2.1 Filtered Backprojection

Our description of Filtered Backprojection introduces the same notation as used in Section II of [15], but is included here to keep the present article self-contained.

In the continuous tomography model that is used to describe Filtered Backprojection, the unknown image is represented by a finite and integrable function  $f: \mathbb{R}^2 \rightarrow \mathbb{R}$  of bounded support. Projections  $p(\theta, \cdot)$  of  $f$  are defined by the *Radon transform*

$$p(\theta, t) = (\mathcal{R}f)(\theta, t) = \int_{-\infty}^{\infty} f(t \cos \theta - s \sin \theta, t \sin \theta + s \cos \theta) ds, \quad (5.1)$$

where  $\theta \in [0, \pi)$  denotes the projection angle and  $t \in \mathbb{R}$  refers to the signed distance of a projected line from the origin.

The unknown image  $f$  can be recovered analytically from its Radon transform based on the following inversion formula:

$$f(x, y) = \int_0^{\pi} \int_{-\infty}^{\infty} P(\theta, u) G(\theta, u) e^{2\pi i u t} du d\theta, \quad (5.2)$$

where  $t = x \cos \theta + y \sin \theta$ ,  $G(\theta, u) = |u|$  and  $P(\theta, \cdot)$  is the Fourier transform of  $p(\theta, \cdot)$ . The function  $G(\theta, \cdot)$  acts as a filter on the projection data [25].

In practical experiments, the detector that measures the projections  $p(\theta, \cdot)$  is discretized as an array of detector elements, each measuring a single value. Moreover, the set of angles  $\theta$  for which projections are available is also finite and discrete.

Let  $R \in \mathbb{N}_{>0}$ . For simplicity, we assume that the detector contains  $l = 2R + 1$  detector elements of unit width and that it is symmetric around  $t = 0$ . Hence, the lines  $(\theta, t)$  for which the Radon transform is observed by these detector elements correspond to the set  $T = \{-R, -R + 1, \dots, R - 1, R\}$  of values for the parameter  $t$  in the Ra-

don transform. Furthermore, the finite set of projection angles is given by  $\Theta = \{\theta_1, \dots, \theta_d\}$ . The FBP formula, which approximates Eq. (5.2), is then given by

$$f(x, y) \approx \frac{\pi}{d} \sum_{\theta \in \Theta} \sum_{\tau \in T} p(\theta, \tau) g(\theta, x \cos \theta + y \sin \theta - \tau), \quad (5.3)$$

with  $g$  the inverse Fourier transform of  $G$ . In practice, various filters are used in FBP, combining the ideal ramp filter with smooth windowing functions. Examples are the Ram-Lak filter (using a hard frequency cut-off) and the Hann and Cosine filters (using soft windowing) [3].

### 5.2.2 Algebraic Reconstruction Methods

In this section we introduce the class of Algebraic Reconstruction Methods (ARMs). The input for these methods is the set of measured projections and a matrix describing the projection geometry, which together define a system of linear equations. Let  $\mathbf{p} = (p_i) \in \mathbb{R}^m$  denote a vector containing the  $m = dl$  measured detector values (with  $d$  the number of angles and  $l$  the number of detectors), and let  $\mathbf{v} = (v_i) \in \mathbb{R}^n$  denote the object to be reconstructed. We now form the system of linear equations

$$\mathbf{W}\mathbf{v} = \mathbf{p}, \quad (5.4)$$

where the matrix  $\mathbf{W}$ , called the *projection matrix*, describes the geometry of the tomography setup. Each entry  $p_i$  of the projection data corresponds to an angle  $\theta \in \Theta$  and detector bin  $t \in T$ , and is therefore also denoted as  $p_{\theta t}$ . Its value corresponds to the weighted sum of the values  $v_j$  on the line parameterized by  $(\theta, t)$ . Various models can be used to determine the weight of the contribution of the pixels on such a line, such as the line model, strip model [26], and Joseph's model [27]. Algebraic reconstruction methods solve the system in Eq. (5.4) by starting at an initial guess of the solution (which can be the zero vector) and iteratively refining the solution. If the system is inconsistent, due to noise or other artefacts in the projection data, the residual of the equation system is often minimized with respect to a particular norm. The results of ARMs can depend substantially on the particular ARM that is selected, for several reasons. First of all, the iteration process is

typically terminated before convergence has been fully reached, such that the resulting reconstruction depends on convergence properties of the algorithm. Secondly, the norm that is minimized depends on the particular ARM. Thirdly, if the equation system is underdetermined (which is quite common in tomography), the particular solution that is chosen among all solutions depends on the ARM.

Algebraic reconstruction methods can be modeled as an operator  $\mathcal{R} : \mathbb{R}^m \rightarrow \mathbb{R}^n$  that maps a vector  $\mathbf{p} \in \mathbb{R}^m$  of projection data to a reconstructed image  $\mathbf{u} \in \mathbb{R}^n$ . Some ARMs are linear, meaning that their operation can be written as  $\mathbf{u} = \mathbf{R}\mathbf{p}$  with  $\mathbf{R} \in \mathbb{R}^{m \times n}$  a matrix (called the *reconstruction matrix* of the ARM). By definition, a linear ARM has the property that  $\mathcal{R}(\lambda\mathbf{p} + \mu\mathbf{q}) = \lambda\mathcal{R}(\mathbf{p}) + \mu\mathcal{R}(\mathbf{q})$  for all  $\lambda, \mu \in \mathbb{R}$  and  $\mathbf{p}, \mathbf{q} \in \mathbb{R}^m$ , which makes it possible to decompose its operation as a sum of reconstructions of unit vectors. This property is essential to the filter construction presented in [15]. The well-known *SIRT* algorithm is an example of a linear method that can be used to compute algebraic filters.

Many ARMs used in practice are not linear. Here, we consider two examples. The *CGLS* algorithm is nonlinear, except in the limit case of an infinite number of iterations. In this limit, *CGLS* converges to the same reconstruction that would result by applying the *Moore-Penrose inverse* [28] to the projection data, which is a linear operator. For any finite number of operations, *CGLS* is not linear. We therefore refer to *CGLS* as a *mildly nonlinear ARM*. Another example of a common nonlinear ARM is the *Expectation Maximization* (EM) algorithm. Even in the case of an infinite number of iterations EM does not have the linearity property. Therefore, we refer to EM as a *nonlinear ARM*. Below, we will outline *CGLS* and EM in more detail.

### 5.2.2.1 CGLS

The Conjugate Gradient (CG) algorithm is commonly used for solving large systems of linear equations, due to its fast convergence. It is originally designed for large sparse systems of equations with a symmetric and positive-definite matrix [29]. We apply a variant of this method, Conjugate Gradient Least Squares (*CGLS*), where the CG algorithm is applied to the system of normal equations  $\mathbf{W}^T \mathbf{W} \mathbf{v} = \mathbf{W}^T \mathbf{p}$ .

Put  $\mathbf{u}^{(0)} = \mathbf{0}$ ,  $\mathbf{r}^0 = \mathbf{p}$ , and  $\mathbf{d}^0 = \mathbf{W}^T \mathbf{p}$ . The iteration which computes  $\mathbf{u}^{k+1}$  ( $k = 0, 1, 2, \dots$ ) is then given by Eq. (5.5).

$$\begin{aligned}
 \alpha_{k+1} &= \|\mathbf{W}^T \mathbf{r}^k\|_2^2 / \|\mathbf{W} \mathbf{d}^k\|_2^2, \\
 \mathbf{u}^{k+1} &= \mathbf{u}^k + \alpha_{k+1} \mathbf{d}^k, \\
 \mathbf{r}^{k+1} &= \mathbf{r}^k - \alpha_{k+1} \mathbf{W} \mathbf{d}^k, \\
 \beta_{k+1} &= \|\mathbf{W}^T \mathbf{r}^{k+1}\|_2^2 / \|\mathbf{W}^T \mathbf{r}^k\|_2^2, \\
 \mathbf{d}^{k+1} &= \mathbf{W}^T \mathbf{r}^{k+1} + \beta_{k+1} \mathbf{d}^k,
 \end{aligned} \tag{5.5}$$

For any system of linear equations, the CGLS algorithm converges to the least squares solution of minimal norm. One way to express this property, is that CGLS converges to  $\mathbf{W}^\dagger \mathbf{p}$ , where  $\mathbf{W}^\dagger$  denotes the Moore Penrose inverse. As  $\mathbf{W}^\dagger$  is a matrix, the limit behavior for CGLS corresponding to a large number of iterations is linear. In practice, one often performs just a few iterations, thereby implicitly imposing a form of regularization on the reconstructed image. As we will demonstrate in Sect. 5.4.1, CGLS is not linear in this case, but a linear model can be used as an approximation.

### 5.2.2.2 EM

Expectation Maximization (EM) aims at finding the reconstruction that is most likely to result in the measured projection data, where the measurements have been perturbed by Poisson noise. The detected photon counts in an X-ray scanner follow such a distribution. The reconstruction that maximizes the likelihood then satisfies Eq. (5.6) [2, 30];

$$\hat{\mathbf{u}} = \hat{\mathbf{u}} \mathbf{W}^T \frac{e^{-\mathbf{W}\hat{\mathbf{u}}}}{e^{-\mathbf{p}}}, \tag{5.6}$$

where  $\mathbf{W}$  has column sum 1 and the arithmetic operations are performed element wise [28, 31]. Here, we focus on a straightforward Expectation Maximization method that iteratively solves Eq. (5.6). For a nonzero start solution  $\mathbf{u}^0$ , the  $(k+1)$ th iteration of the multiplicative algorithm EM is given by Eq. (5.7);

$$\mathbf{u}^{k+1} = \mathbf{u}^k \mathbf{W}^T \frac{e^{-\mathbf{W}\mathbf{u}^k}}{e^{-\mathbf{p}}}. \tag{5.7}$$

Note that in practice, regularization is often employed to make the method more stable [28].

### 5.3 ALGEBRAIC FILTERS FOR FBP

We now briefly discuss the AF-FBP approach for linear algebraic reconstruction methods, followed by our adaptation to make this method applicable to nonlinear algebraic reconstruction methods.

#### 5.3.1 The Linear Case

In [15], a method is presented to create filters for FBP based on a linear algebraic reconstruction method (LARM) of choice. The reconstructions of FBP with these filters approximate the reconstruction quality of the LARM. As explained in Sect. 5.2.2, a linear reconstruction method can be represented by the reconstruction matrix  $\mathbf{R}$ . The value  $u_c$  of a single pixel  $c \in \{1, \dots, n\}$  in the reconstruction  $\mathbf{u} = \mathbf{R}\mathbf{p}$  is given by

$$u_c = \sum_{\theta \in \Theta} \sum_{t \in T} r_{\theta t}^{(c)} p_{\theta t}, \quad (5.8)$$

where  $r_{\theta t}^{(c)}$  is the entry of  $\mathbf{R}$  in row  $c$  and column  $\theta t$ .

Define the center of pixel  $c$  as  $(x_c, y_c) \in \mathbb{R} \times \mathbb{R}$ , and let  $t_c^{(\theta)} = x_c \cos \theta + y_c \sin \theta$  for  $\theta \in \Theta$ . Define the function  $h^{(c)}$  by

$$h^{(c)}(\theta, \tau) = r_{\theta(\tau+t_c^{(\theta)})}^{(c)}, \quad (5.9)$$

where  $(\theta, \tau) \in (\Theta \times (T - t_c^{(\theta)}))$ . Then we can write  $u_c$  as

$$u_c = \sum_{\theta \in \Theta} \sum_{t \in T} h^{(c)}(\theta, t - t_c^{(\theta)}) p_{\theta t}. \quad (5.10)$$

Note that the formulas are valid for any set of projection data, either consistent (i.e. in the range of the Radon transform) or inconsistent. Comparing Eqs. (5.3) and (5.10) shows that  $h^{(c)}$  acts as a filter on the projection data for pixel  $u_c$ . This filter is called an *algebraic filter*, and is determined by calculating the impulse response of pixel  $c$  for all the detector positions  $\theta t$ . Similarly, we can create filters for the other pixels in the image domain. It is reasonable to expect that these



filters resemble  $h^{(c)}$ , at least for pixels in a neighborhood of  $u_c$ . As shown in [15], applying the algebraic filter of  $u_c$  to all the pixels in the image results in a reconstruction quality that is comparable to that of the LARM used to create the filter. This method is known as AF-FBP with the algebraic filter  $h^{(c)}$ . Note that in practice, one uses a Fourier convolution operation to evaluate the result of applying the filter to the projection data.

### 5.3.2 The Nonlinear Case

Nonlinear algebraic reconstruction methods (NLARMs) are used in many applications of computed tomography. As with linear reconstruction methods, a disadvantage of these methods is their expensive computational cost. If the AF-FBP approach as described in Sect. 5.3.1 could be applied, then this would lead to a method with relatively low computational cost that approximates the NLARM.

The method described in Sect. 5.3.1 requires linearity of the reconstruction operator  $\mathcal{R}$  (see Sect. 5.2.2), which is clearly not satisfied for general NLARMs. We now introduce a variant of AF-FBP that *can* be applied to NLARMs, provided that the NLARM behaves *locally* as a linear transformation. We say that a reconstruction method is locally linear if for a set of projections  $\mathbf{p} \in \mathbb{R}^m$  and a small perturbation  $\Delta\mathbf{p} \in \mathbb{R}^m$ , there exists a linear transformation  $\mathbf{L}_{\mathbf{p}} : \mathbb{R}^m \rightarrow \mathbb{R}^n$  such that

$$\mathcal{R}(\mathbf{p} + \Delta\mathbf{p}) \approx \mathcal{R}(\mathbf{p}) + \mathbf{L}_{\mathbf{p}}\Delta\mathbf{p}. \quad (5.11)$$

As the matrix  $\mathbf{L}_{\mathbf{p}}$  can be seen as a linear reconstruction method that reconstructs the perturbation of the projection data with respect to the projection data  $\mathbf{p}$ , we can approximate this method by FBP with an appropriately chosen filter  $h^{(c)}$ .

A difference with the filter method for the linear case is the dependence of the matrix  $\mathbf{L}_{\mathbf{p}}$  on the projection data  $\mathbf{p}$ . For every new set of projections  $\mathbf{p}$  the matrix  $\mathbf{L}_{\mathbf{p}}$  changes and the filter  $h^{(c)}$  has to be recalculated. In certain practical applications, in particular in industrial tomography, a blueprint of the scanned object is already available, while one aims to reconstruct the deviations from this blueprint. In this case, the measured projection data  $\mathbf{p}_m$  is the superposition of the forward projection  $\mathbf{p}_b$  of this blueprint and the forward projection of

the variation, denoted by  $\Delta\mathbf{p}$ . The reconstruction  $\mathbf{v} = \mathcal{R}(\mathbf{p}_m)$  is then given by  $\mathbf{v} = \mathcal{R}(\mathbf{p}_b + \Delta\mathbf{p})$ . Since  $\mathcal{R}$  is a locally linear transformation, there exists a matrix  $\mathbf{L}_{\mathbf{p}_b} \in \mathbb{R}^{m \times n}$  such that  $\mathbf{v} \approx \mathcal{R}(\mathbf{p}_b) + \mathbf{L}_{\mathbf{p}_b} \Delta\mathbf{p}$ . Note that  $\mathbf{L}_{\mathbf{p}_b}$  is independent of the perturbation  $\Delta\mathbf{p}$ .

In the remainder of this chapter we will refer to the known image as the *blueprint image*. An example of a blueprint image is the cross-section of a turbine blade. Variations on this blueprint are cracks, holes or local variations in density, while the general shape and size of the blade is equal to that of the blueprint.

For these locally linear transformations we can create a filter with a similar method as described in Sect. 5.3.1 for linear algorithms. Instead of calculating an impulse response as in the linear case, we now calculate a local derivative around  $\mathbf{p}_b$ , because  $\mathbf{L}_{\mathbf{p}_b}$  depends on  $\mathbf{p}_b$  and acts on the perturbation  $\Delta\mathbf{p}$ . Hence for a given pixel  $c$ , we calculate the filter values at  $\theta \in \Theta$ ,  $t \in T$  as stated in Algorithm 1.

---

**Algorithm 1:** Calculate filters for locally linear algebraic reconstruction algorithms

---

**Data:**  $\mathcal{R} : \mathbb{R}^n \rightarrow \mathbb{R}^m$  an NLARM,  
 $\mathbf{p}_b \in \mathbb{R}^m$  the projection data of a blueprint image,  
 $\Theta$  the set of all projection angles,  
 $T$  the set of all detector pixels.

**Result:** The algebraic filter  $h^{(c)}$  corresponding to  $\mathcal{R}$  for  $\mathbf{p}_b$ .

```

begin
  Choose a pixel  $c$  in the image
  Define  $(x_c, y_c) \in \mathbb{R} \times \mathbb{R}$  the center of pixel  $c$ 
  Define  $\mathbf{e}_{\theta t}$  the unit vector with value 1 at entry  $\theta t$  for
     $\theta \in \Theta, t \in T$ 
  for  $\theta \in \Theta$  do
    for  $t \in T$  do
       $\mathbf{l}_{\theta t}^{(c)} = [\mathcal{R}(\mathbf{p}_b + \mathbf{e}_{\theta t})]_c - [\mathcal{R}(\mathbf{p}_b)]_c$ 
    end
    Define  $\mathbf{t}_c^{(\theta)} = x_c \cos \theta + y_c \sin \theta$ 
    Define  $h^{(c)}$  for  $\tau \in T - \mathbf{t}_c^{(\theta)}$  by  $h^{(c)}(\theta, \tau) = \mathbf{l}_{\theta(\tau + \mathbf{t}_c^{(\theta)})}^{(c)}$ 
  end
end
```

---

This filter  $h^{(c)}$  can be used in FBP in the same way as the (angle dependent) standard filters and the filters for the linear algebraic reconstruction methods. The implementation of AF-FBP for NLARM is stated in Algorithm 2. We will refer to this algorithm as nIAF-FBP. In cases where the distinction between the linear and nonlinear variant of AF-FBP is not relevant for the discussion, we use the general term AF-FBP.

---

**Algorithm 2:** Applying the AF-FBP filters for NLARM

---

**Data:**  $BP : \mathbb{R}^n \rightarrow \mathbb{R}^m$  the unfiltered backprojection operation,  
 $\mathcal{R} : \mathbb{R}^n \rightarrow \mathbb{R}^m$  an NLARM,  
 $\mathbf{p}_m \in \mathbb{R}^m$  the measured projection data,  
 $\mathbf{p}_b \in \mathbb{R}^m$  the projection data of the blueprint image,  
 $\Theta$  the set of all projection angles,  
 $T$  the set of all detector pixels.

**Result:** Reconstruction  $\mathbf{v} \in \mathbb{R}^n$ .

**begin**

    // Calculate the perturbation  $\Delta \mathbf{p}$

$\Delta \mathbf{p} = \mathbf{p}_m - \mathbf{p}_b$

**for**  $\theta \in \Theta$  **do**

        // Apply the angle dependent algebraic  
         filter  $h^{(c)}$  on  $\Delta \mathbf{p}$

$\check{\mathbf{p}} = \sum_{\tau \in T} h^{(c)}(\theta, \tau - t_c^{(\theta)}) \Delta \mathbf{p}_{\theta\tau}$

**end**

$\mathbf{v} = \mathcal{R}(\mathbf{p}_b) + BP(\check{\mathbf{p}})$

**end**

---

5.4 EXPERIMENTS

To examine the performance of the nIAF-FBP method, a series of computational experiments has been carried out based on simulated projection data. Validating the approach is not straightforward, as the reconstruction accuracy depends not only on the algebraic method and its parameters, but also on the blueprint image and the scanned object. We have chosen to focus on five key-aspects: (i) to verify that the selected nonlinear algebraic methods indeed exhibit locally linear behavior; (ii) to demonstrate the image quality of the nIAF-FBP approximation for a set of realistic differences between blueprint and scanned

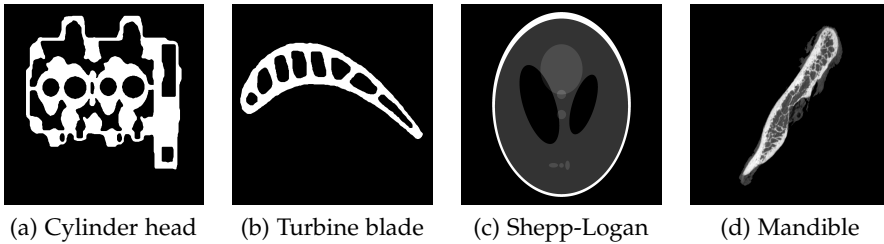


Figure 5.1: The blueprint images.

object; (iii) to investigate robustness with respect to noise; (iv) to determine robustness with respect to image registration errors between the scanned object and the blueprint; and (v) to investigate the robustness with respect to beam hardening artefacts.

As blueprint images, we consider both binary images and blueprints having continuous grey levels. They are shown in Fig. 5.1 and correspond to (5.1a) a cross-section of a cylinder head, (5.1b) a cross-section of a turbine blade, (5.1c) the well-known Shepp-Logan phantom, and (5.1d) a cross-section of a mandible. All the blueprint images are defined on a grid of  $2044 \times 2044$  pixels. The cylinder head and turbine blade phantoms are representative for inspection tasks in industrial tomography, which we consider the primary application target of our nIAF-FBP approach. The Shepp-Logan and mandible phantom have been added to demonstrate how the algorithm performs for objects with multiple and continuous grey levels, respectively.

Real-world objects can typically not be represented on a pixel grid. To approximate the continuous nature of real objects, the reconstructions are performed on a coarser grid, where four phantom pixels correspond to one pixel in the reconstruction grid. The projection data are computed based on a detector of 511 bins with a width of four image pixels per bin. We use an equiangular parallel beam geometry with a relatively small number of 64 projections, varying between 0 and 180 degrees, as this is a scenario where algebraic methods typically are preferred over Filtered Backprojection. We use the strip model to determine the contribution of each image pixel to a projection ray [26].

The following reconstruction methods are used in the computational experiments:

## ALGEBRAIC RECONSTRUCTION METHODS

**CGLS** Conjugate Gradient Least Squares; see Sect. 5.2.2.1. The start solution in Eq. (5.5) is  $\mathbf{u}^0 = \mathbf{0}$ . The total number of iterations is  $K = 10$ .

**EM** Expectation Maximization; see Sect. 5.2.2.2. The start solution in Eq. (5.7) is  $\mathbf{u}^0 = \mathbf{1}$ . The total number of iterations is given by  $K = 50$ .

## FILTERED BACKPROJECTION METHODS

**FBP-RL, FBP-HANN, FBP-COS** Filtered Backprojection with the standard Ram-Lak, Hann and Cosine filters; see Sect. 5.2.1.

**nLCGLS-FBP** Filtered Backprojection with an algebraic filter based on CGLS with 10 iterations. The filter coefficients for the central pixel in Alg. 1 are used to create the filter.

**nLEM-FBP** Filtered Backprojection with an angle-dependent algebraic filter based on EM with 50 iterations. For every blueprint image a non-zero pixel close to the central pixel in Alg. 1 is selected to calculate the filter coefficients.

For nLCGLS-FBP and nLEM-FBP, the algebraic filters are applied to the perturbation  $\Delta \mathbf{p}$  as described in Alg. 2 to obtain the AF-FBP reconstructions. For FBP with standard filters (FBP-RL, FBP-Hann, FBP-Cos), the filters are applied to the measured projection data.

To quantify the quality of the reconstructed images, we consider two error measures: the deviation from the phantom itself (i.e. the unknown ground truth) and the deviation from a reconstruction obtained by the algebraic method that one tries to approximate. To compare the reconstructions to the phantom, the reconstruction is upsampled by a factor 4, replacing each reconstruction pixel by a block of  $4 \times 4$  pixels with the same value. We denote this enlarged image of  $2044 \times 2044$  pixels by  $\hat{\mathbf{u}} = (\hat{u}_{ij}) \in \mathbb{R}^{n^2}$  with  $n = 2044$ . We define the *mean reconstruction error*  $E_r$  by

$$E_r = \frac{\sum_{i,j} |\hat{u}_{ij} - v_{ij}|}{\sum_{i,j} v_{ij}}, \quad (5.12)$$

where  $\mathbf{v} = (v_{ij}) \in \mathbb{R}^{n^2}$  denotes the phantom. The *mean ARM reconstruction error*  $E_r^{\text{ARM}}$  is computed similarly, yet the reconstruction is compared to the ARM reconstruction (either CGLS or EM) instead of the phantom. Our approach is designed to approximate the underlying nonlinear algebraic method, so ideally the ARM reconstruction error will be small, while the reconstruction error with respect to the phantom can still be considerable.

#### 5.4.1 Local Linearity

The validity of the proposed approach is based on the assumption that nonlinear tomographic reconstruction methods exhibit approximately linear behavior in the vicinity of the blueprint image. We performed a set of experiments to validate this assumption. In these experiments, the value of a single pixel in the reconstruction is monitored while a perturbation of increasing norm is introduced in the projections. If the reconstruction method is locally linear, the value of this pixel should also depend linearly on the magnitude of the perturbation.

We examined this property for CGLS and EM by considering two sets of projection data  $\mathbf{p}$ ,  $\mathbf{q}$ , for the blueprint and the scanned object respectively. The perturbation  $\Delta\mathbf{p} \in \mathbb{R}^n$  in Eq. (5.11) is defined as  $\lambda(\mathbf{q} - \mathbf{p})$  with  $\lambda \in [0, 1]$ . We compute both  $\mathcal{R}(\mathbf{p}) + \lambda(\mathcal{R}(\mathbf{q}) - \mathcal{R}(\mathbf{p}))$  and  $\mathcal{R}(\mathbf{p} + \lambda(\mathbf{q} - \mathbf{p}))$  for every value of  $\lambda \in [0, 1]$  and compare the results for a particular pixel (located in the interior of the phantom) in the reconstruction.

Figure 5.2 shows the grey level of this pixel as a function of the parameter  $\lambda$ , for CGLS and EM in two scenarios: (i) a disk-shaped gap of grey level 0 and radius 50 pixels is introduced in the cylinder head phantom, creating an artificial gap; the observed pixel is included in this disk. (ii) The images  $\mathbf{p}$  and  $\mathbf{q}$  are completely different;  $\mathbf{p}$  is the Shepp-Logan phantom, whereas  $\mathbf{q}$  is the cylinder head phantom.

The results are visualized using a blue (dotted) curve and a red (solid) line. The red line corresponds to the pixel value of  $\mathcal{R}(\mathbf{p}) + \lambda(\mathcal{R}(\mathbf{q}) - \mathcal{R}(\mathbf{p}))$ , and the blue curve corresponds to the pixel value of  $\mathcal{R}(\mathbf{p} + \lambda(\mathbf{q} - \mathbf{p}))$ , for  $\lambda \in [0, 1]$  variable. Large deviations of the blue curve from the red line imply that the corresponding reconstruction method does not behave locally as a linear function.

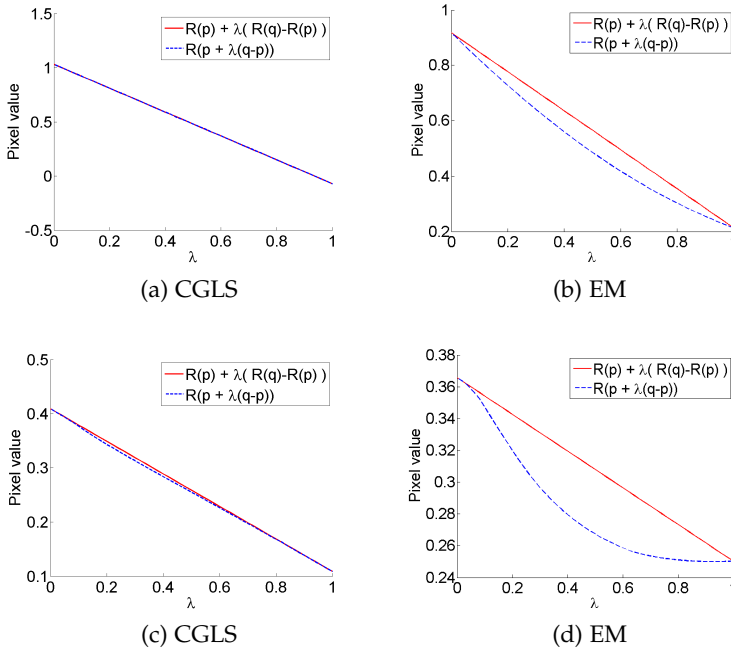


Figure 5.2: Plots of the local linearity for a particular image pixel; if the algorithm is locally linear, the blue and red lines should coincide. (a-b) deviation is a black disk of radius 50; (c-d) true object is completely different from blueprint.

Although these results depend on the particular pixel for which the grey value is plotted, they illustrate general observations about the two algorithms that we found in a broad set of observed pixels: (i) the CGLS algorithms shows almost perfectly linear behavior for small perturbations and close-to-linear behavior for large deviations; (ii) the EM algorithm clearly shows nonlinear behavior already for small deviations, although it may still be sufficiently linear for our purpose; for large deviations, EM exhibits strongly nonlinear behavior.

#### 5.4.2 Variations with cracks

To evaluate how the nAF-FBP approach performs for realistic deviations between the blueprint and the scanned object, we now consider the cylinder head and turbine blade phantoms, which resemble objects

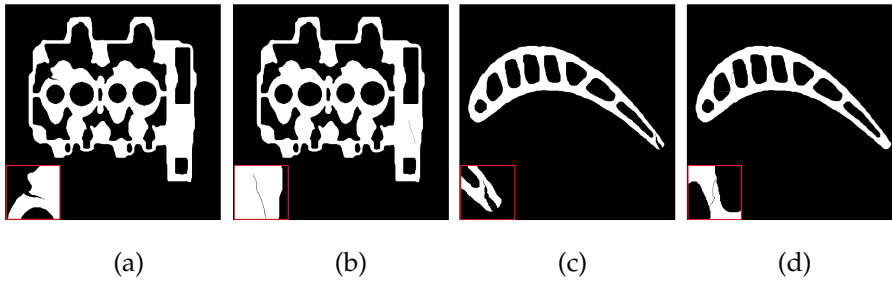


Figure 5.3: Example from each of the four categories of crack images: (a) cylinder head (broad); (b) cylinder head (narrow); (c) turbine blade (broad); (d) turbine blade (narrow).

that are common in the field of nondestructive testing. Four sets of test images have been manually created by introducing artificial cracks to the phantom objects. For each of the two objects, a set of *broad cracks* was created, as well as a set of *narrow cracks*. Each set consists of six images. An example for each set is shown in Figure 5.3, where the crack is magnified in the left corner.

In Table 5.1 we show the mean ARM reconstruction errors (i.e. compared to either CGLS or EM) over each of the four sets, for the proposed nAF-FBP method vs. FBP with three standard filters (FBP-Cos, FBP-Hann, and FBP-RL). We observe that the mean ARM reconstruction error for nCGLS-FBP is very small compared to FBP with standard filters. For nEM-FBP the approximation of EM is not as good compared to CGLS, but the ARM reconstruction errors are still substantially smaller than those of FBP with standard filters for all cracks examined.

An illustration of the results for a particular testcase is shown in Figure 5.4. In all images, the box in the left corner contains a zoomed version of the crack. We first note that a standard Filtered Backprojection reconstruction without the use of a blueprint object (Fig. 5.4a) clearly shows the crack, yet also contains a considerable number of streak artefacts, making it difficult to distinguish between defects and artefacts. The CGLS (Fig. 5.4b) and EM (Fig. 5.4d) reconstructions are less prone to such artefacts. For both CGLS and EM, the nAF-FBP reconstruction is visually very similar to the result of the algebraic method, whereas the FBP-Cos method yield quite different results. We observed similar results using other standard FBP filters.



Class	nIAF-FBP	FBP-Cos	FBP-Hann	FBP-RL
<b>CGLS</b>				
Cylinder head (broad)	1.7e-3 (7.5e-4)	1.9e-2 (1.7e-3)	1.6e-2 (1.6e-3)	2.6e-2 (2.1e-3)
Cylinder head (narrow)	4.0e-4 (1.1e-4)	6.4e-3 (8.3e-4)	4.9e-3 (6.1e-4)	1.1e-2 (1.4e-3)
Turbine blade (broad)	4.7e-3 (3.0e-3)	4.7e-2 (1.9e-2)	3.9e-2 (1.5e-2)	6.9e-2 (3.3e-2)
Turbine blade (narrow)	8.4e-4 (3.1e-4)	1.3e-2 (3.5e-3)	1.0e-2 (2.7e-3)	2.3e-2 (5.9e-3)
<b>EM</b>				
Cylinder head (broad)	6.8e-3 (1.2e-3)	6.4e-1 (9.3e-4)	6.0e-1 (8.4e-4)	7.2e-1 (1.1e-3)
Cylinder head (narrow)	1.9e-3 (2.1e-4)	6.4e-1 (1.6e-4)	6.0e-1 (1.3e-4)	7.2e-1 (2.7e-4)
Turbine blade (broad)	2.8e-2 (1.4e-2)	8.8e-1 (3.2e-3)	8.3e-1 (2.7e-3)	9.8e-1 (4.5e-3)
Turbine blade (narrow)	5.9e-3 (1.9e-3)	8.7e-1 (4.6e-4)	8.2e-1 (3.4e-4)	9.7e-1 (8.8e-4)

Table 5.1: Mean ARM reconstruction errors for the different categories of cracks, for the different reconstruction methods. For each set of experiments, the mean ARM reconstruction error is shown in black, and the standard deviation (over 6 crack images) in light grey.

We emphasize that the goal of our approach is to provide an accurate approximation of the algebraic method, which is not necessarily the same as providing the most accurate reconstruction. The results of Table 5.1 and Fig. 5.4 demonstrate that indeed the nICGLS-FBP and nIEM-FBP methods provide a reconstructed image highly similar to the respective CGLS and EM reconstructions.

#### 5.4.3 Robustness with respect to noise

So far, the projection data used in the experiments was noiseless. Since real (i.e. measured) datasets often contain noise, we also examine the robustness of nIAF-FBP with respect to noise. We applied Poisson

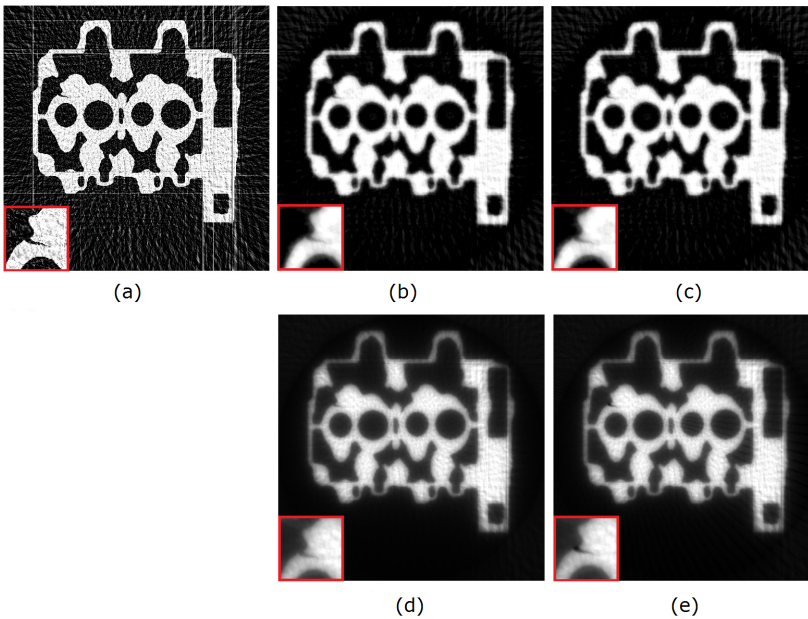


Figure 5.4: Illustration of reconstruction results for a broad crack in the cylinder head; (a) FBP-Cos, without using a blueprint, (b) CGLS, (c) nCGLS-FBP, (d) EM, (e) nEM-FBP. The images (c) and (e) are based on reconstruction of the difference between the object and the blueprint.

noise to the projection data by first transforming the Radon transform data into photon counts (using the exponential function), subsequently generating noisy photon count by drawing from a Poisson distribution for each detector value, and then using the logarithm to convert the noisy data back to linearized projection data. Note that the resulting linearized projections can contain negative values, which are set to 0. In the results, the noise level is indicated by  $I_0$ , the photon count measured at a detector pixel without an object between source and detector (higher value means less noise). Fig. 5.5 shows a series of examples of reconstructed images for the mandible and turbine blade phantoms. Fig. 5.6 shows the mean reconstruction error and mean ARM reconstruction error for the mandible phantom as a function of noise level, averaging the results over a large number of noise realizations.

By visually comparing the reconstructions in Fig. 5.5, we notice that nCGLS-FBP handles noisy projection data well compared to FBP with

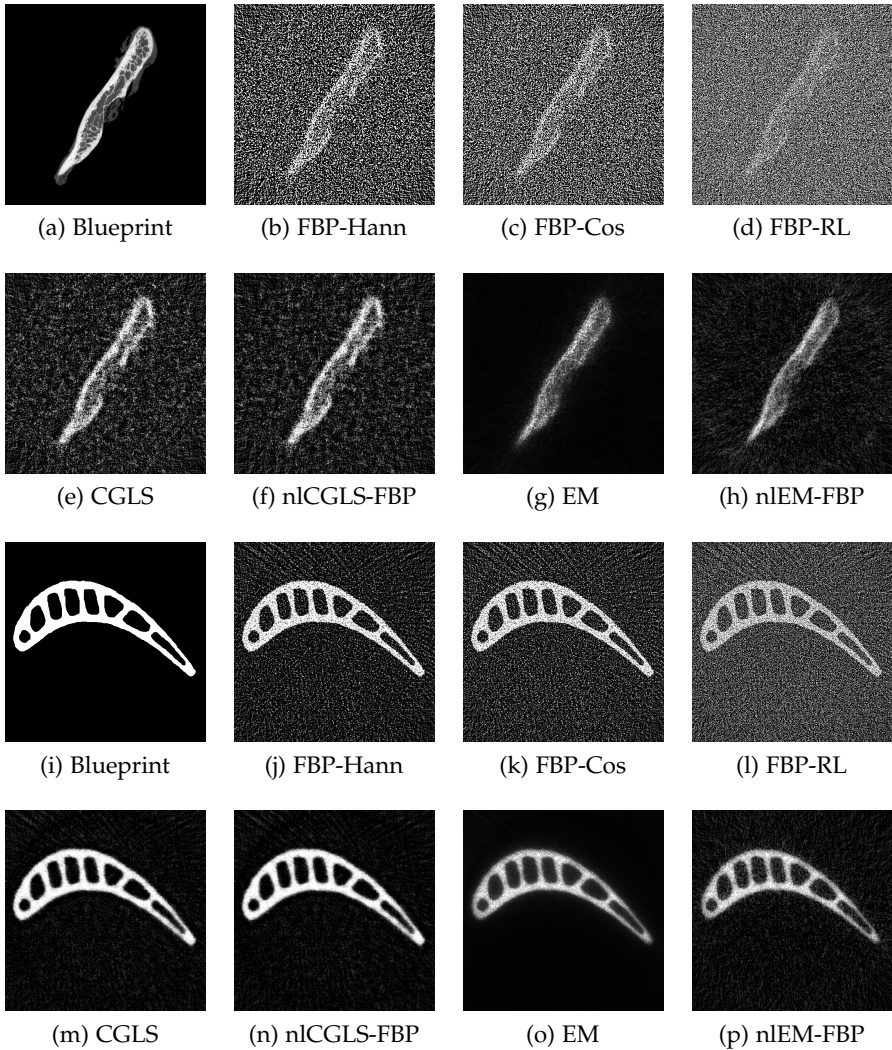


Figure 5.5: Reconstructions for the mandible and turbine phantom with noisy projection data; (a)-(h):  $I_0 = 10^5$ , (i)-(p):  $I_0 = 10^6$ .

a standard filter. This is confirmed by the corresponding reconstruction errors, where the accuracy of nCGLS-FBP is similar to that of the CGLS reconstructions. The accuracy of nLEM-FBP is also much better than that of FBP with standard filters, but it is not as close to EM as nCGLS-FBP is to CGLS. It is, however, a good approximation of EM

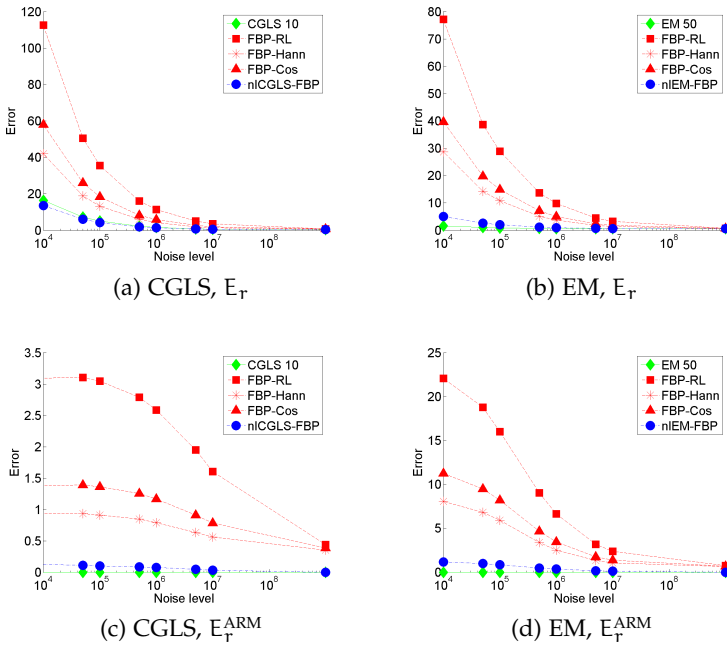


Figure 5.6: Mean reconstruction error with either the original phantom ( $E_T$ ) or the ARM reconstruction ( $E_T^{\text{ARM}}$ ) for the mandible phantom with varying Poisson noise levels  $I_0$  applied to the projection data.

based on the results of  $E_T^{\text{ARM}}$ . We observe similar results for the other phantoms and for other numbers of projection angles.

Hence in case of noisy projection data, nlAF-FBP yields results that approximate the NLARM well for both CGLS and EM, yet a more accurate approximation is observed for CGLS compared to EM. Compared to FBP using standard filters, the nlAF-FBP method (for both CGLS and EM) yields reconstruction with a strongly reduced noise level.

#### 5.4.4 Robustness with respect to registration errors

Even if a blueprint of the scanned object is available, there may be registration errors between the scanned object and the blueprint, in addition to the deviations of the actual object structure. To examine the effect of such errors on the reconstruction accuracy of the AF-FBP method, we performed a series of experiments where the scanned object

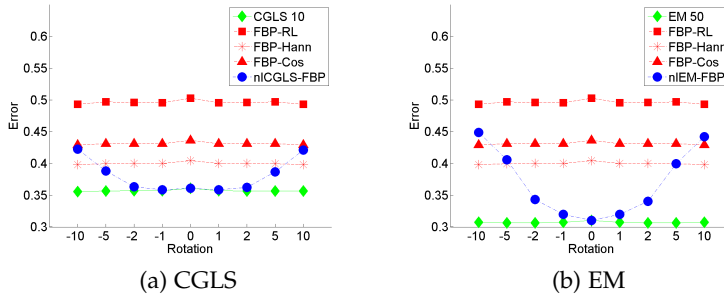


Figure 5.7: Mean reconstruction error with the rotated phantom ( $E_r$ ) for the Shepp-Logan phantom.

is obtained by rotating the blueprint around its center. The rotations are denoted by the number of degrees, where a positive number corresponds to a rotation clockwise and a negative number to a rotation counterclockwise.

In Fig. 5.7 the mean reconstruction error is shown for the Shepp-Logan phantom. For small rotations of at most a few degrees, nlCGLS-FBP is almost as accurate as CGLS. Using FBP with standard filters to obtain reconstructions results in considerably higher reconstruction errors. The nlEM-FBP is less tolerant to registration errors and becomes less accurate than EM already for rotations of 1 degree. We observed similar results for the other phantoms.

#### 5.4.5 Beam hardening

The previous experiments have been conducted using a monochromatic X-ray beam. For a monochromatic beam, the law of Lambert-Beer states that the measured projections (after log-correction) increase linearly with the thickness of a homogeneous object. In practice, however, a polychromatic X-ray beam is often used and the measured projections depend on the thickness of the object in a nonlinear way, resulting in beam hardening artefacts [2]. Especially for objects with metal parts, such as the cylinder head phantom and turbine blade phantom, beam hardening should be taken into account.

We performed a series of experiments to determine the behaviour of the nIAF-FBP method when the projection data are obtained using

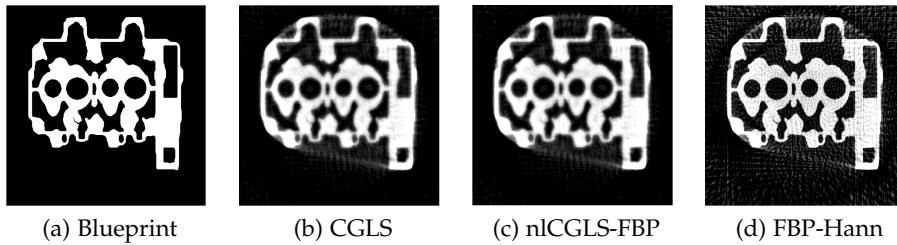


Figure 5.8: Reconstructions of the cylinder head phantom with a broad crack. Note that the subfigures (b)-(d) have a different grey level range compared to the phantom, to provide a more clear visualization of the beam hardening artefacts.

Class	nCGLS-FBP	FBP-Cos	FBP-Hann	FBP-RL
<b>CGLS</b>				
Cylinder head (broad)	1.7e-3 (4.8e-4)	2.7e-1 (3.2e-4)	2.4e-1 (2.7e-4)	3.4e-1 (4.3e-4)
Cylinder head (narrow)	9.9e-4 (5.2e-5)	2.7e-1 (5.5e-5)	2.4e-1 (4.5e-5)	3.4e-1 (9.8e-5)
Turbine blade (broad)	1.3e-1 (4.8e-4)	3.4e-1 (1.2e-3)	3.0e-1 (1.0e-3)	4.2e-1 (1.9e-3)
Turbine blade (narrow)	1.3e-1 (5.4e-5)	3.3e-1 (1.7e-4)	2.9e-1 (1.2e-4)	4.1e-1 (4.7e-4)

Table 5.2: Mean ARM reconstruction errors for the different categories of cracks for CGLS, using a polychromatic X-ray beam. For each set of experiments, the mean ARM reconstruction error is shown in black, and the standard deviation (over 6 crack images) in light grey.

a polychromatic source. For the sake of brevity, we focus here on the CGLS algorithm. To simulate beam hardening, we apply the correlation between material thickness and attenuation as found by [32]. The reconstructions are shown in Fig. 5.8. The corresponding mean ARM reconstruction errors for CGLS for both the cylinder head phantom and the turbine phantom are shown in Table 5.2.

We observe that also for a polychromatic X-ray beam the mean ARM reconstruction error for nCGLS-FBP is smaller than that of FBP

with standard filters. Hence nCGLS-FBP reconstructions resemble the CGLS reconstruction better than reconstructions of FBP with standard filters.

## 5.5 DISCUSSION AND CONCLUSIONS

We have presented a novel approach for computing algebraic filters that can be used in FBP. With these filters we can approximate algebraic reconstruction methods with the computational efficiency of filtered backprojection. Contrary to the original AF-FBP method, which requires the underlying algebraic reconstruction method to be linear, our new approach is aimed at approximating *nonlinear* reconstruction methods, provided that they exhibit *local* linearity for reconstructions close to a given blueprint image. We experimentally investigated this local linearity property for two nonlinear methods: Conjugate Gradient Least Squares with a small number of iterations, and Expectation Maximization. The results show that while for CGLS the local linearity assumption is satisfied quite well, EM shows significant deviations from linear behavior. Using our approach for computing filters that act on the *difference* between the measured projection data and the projections of the blueprint, we performed experiments to assess the capabilities of our algorithm for both CGLS and EM. For CGLS, our approach results in reconstructions that are highly similar to the result of applying CGLS directly to the measured data, while reducing the computation cost to that of applying FBP (once the pre-processing has been done). The variations can be confined to small regions (such as cracks), but moderate registration errors with respect to the blueprint image are also tolerated well. These results are not restricted to monochromatic beams. Also for polychromatic beams nCGLS-FBP approximates the reconstruction accuracy of CGLS. For the EM algorithm, which has a stronger nonlinear nature, the results are mixed. Noisy projection data and cracks are in general handled well. For variations concerning the whole blueprint image, such as rotations, the approximation accuracy of nEM-FBP degrades. Hence in several scenarios the nonlinear algebraic filter approach yields more accurate reconstructions than using a standard filter for FBP, but there are also cases where it fails. Investigating the exact conditions under which our method is favorable, and

also the influence of the pixel location for which the filter is computed, will require further research.

Compared to FBP, algebraic methods are more suitable for limited-data scenarios. The ability to approximate the results of slow, nonlinear algebraic methods using very fast FBP methods opens up the possibilities of reducing the acquisition time, while keeping reconstruction quality constant. As already discussed in [15], computing the algebraic filters is computationally highly demanding, as it requires one to carry out a large number of ARM reconstructions (one per detector element). Even when using a moderately sized GPU cluster, the computation of a new filter may take a full day of computation time, based on the implementation in [33]. As outlined in [15], the computational load can sometimes be considerably reduced by angle independent filters.

The computational overhead for calculating a set of filters for a blueprint becomes cumbersome when the blueprint changes frequently. The presented method is therefore especially suitable for nondestructive testing and inspection of a small range of industrial objects, for which blueprints are readily available. In situations where algebraic reconstruction methods are preferred over FBP with standard filters, such as a limited range of available projection angles, the extensive computation time can be a bottleneck in the testing process. For scenarios where a large number of similar objects must be scanned, the nIAF-FBP approach allows for very fast – or even real-time – reconstruction of batches of objects once the filters have been computed.



## BIBLIOGRAPHY

- [1] F. Natterer. *The Mathematics of Computerized Tomography*. Philadelphia: SIAM, 2001.
- [2] T. M. Buzug. *Computed Tomography: From Photon Statistics to Modern Cone-Beam CT*. Berlin: Springer, 2008.
- [3] A. C. Kak and M. Slaney. *Principles of Computerized Tomographic Imaging*. Philadelphia: SIAM, 2001.
- [4] G. T. Herman. *Fundamentals of Computerized Tomography: Image Reconstruction from Projections*. Berlin: Springer, 2009.
- [5] P. Targowski et al. The Application of Optical Coherence Tomography to Non-Destructive Examination of Museum Objects. *Studies in Conservation* 2004; 49(2): 107–114.
- [6] M. Defrise and G. T. Gullberg. Image reconstruction. *Phys. Med. Biol.* 2006; 51(13): 139–154.
- [7] W. A. Kalender. X-ray computed tomography. *Phys. Med. Biol.* 2006; 51(13): 29–43.
- [8] H. Sipila. Moving object computer-tomography for luggage inspection. *Applications of Signal and Image Processing in Explosives Detection Systems*. Ed. by M. C. Connelly and S. M. Cheung. Proc. SPIE, 1993; 1824: 39–40.
- [9] S. Van Aert et al. Three-dimensional atomic imaging of crystalline nanoparticles. *Nature* 2011; 470(7334): 374–377.
- [10] L. A. Feldkamp, L. C. Davis, and J. W. Kress. Practical cone-beam algorithm. *J. Opt. Soc. Am.* 1984; 1(A6): 612–619.
- [11] K. J. Batenburg and J. Sijbers. DART: a practical reconstruction algorithm for discrete tomography. *IEEE Trans. Image Process.* 2011; 20: 2542–2553.
- [12] D. C. Durairaj, M. C. Krishna, and R. Muregesan. A neural network approach for image reconstruction in electron magnetic resonance tomography. *Comput. Biol. Med.* 2007; 37: 1492–1501.
- [13] R. J. Gaudette et al. A comparison study of linear reconstruction techniques for diffuse optical tomographic imaging of absorption coefficient. *Phys. Med. Biol.* 2000; 45: 1051–1070.

- [14] X. Pan, E. Y. Sidky, and M. Vannier. Why do commercial CT scanners still employ traditional, filtered back-projection for image reconstruction? *Inv. Problems* 2009; 25(12): 123009.
- [15] K.J. Batenburg and L. Plantagie. Fast Approximation of Algebraic Reconstruction Methods for Tomography. *IEEE Trans. Image Process.* 2012; 21(8): 3648–3658.
- [16] J. Zhou et al. An investigation of higher-order tomographic filters using Fourier transforms of reconstructed images. *Nuclear Instruments and Methods in Physics Research Section B: Beam Interactions with Materials and Atoms* 1994; 88(4): 485–489.
- [17] J. Hsieh Y. Wei G. Wang. An intuitive discussion on the ideal ramp filter in computed tomography (I). *J. Comput. Math. Appl.* 2005; 49(5–6): 731–740.
- [18] T. Nielsen et al. Filter Calculation for X-Ray Tomosynthesis Reconstruction. *Phys. Med. Biol* 2012; 57(12): 3915–3930.
- [19] H. Kunze et al. Filter determination for Tomosynthesis aided by iterative reconstruction techniques. *Proc. of Fully3D* 2007: 309–312.
- [20] A. Björck. *Numerical Methods for Least Squares Problems*. Philadelphia: SIAM, 1996.
- [21] L. A. Shepp and Y. Vardi. Maximum Likelihood Reconstruction for Emission Tomography. *IEEE Trans. Med. Imag.* 1982; 1: 113–122.
- [22] L. Zhang et al. X-ray Spectrum Estimation from Transmission Measurements Using the Expectation Maximization Method. *IEEE Nucl. Sci. Symp. Conf. Rec.* 2007; 4: 3089–3093.
- [23] C.A. Bouman and K. Sauer. A unified approach to statistical tomography using coordinate descent optimization. *IEEE Trans. Image Process.* 1996; 5: 480–492.
- [24] L. De Barros, M. Dietrich, and B. Valette. Full waveform inversion of seismic waves reflected in a stratified porous medium. *Geophysical Journal International* 2010; 182(3): 1543–1556.
- [25] A. Markoe. *Analytic Tomography*. New York: Cambridge University Press, 2006.

- [26] J. Zhu et al. Analysis on the strip-based projection model for discrete tomography. *Discrete Applied Mathematics* 2008; 156(12): 2359–2367.
- [27] P.M. Joseph. An improved algorithm for reprojecting rays through pixel images. *IEEE Trans. Med. Imag.* 1982; 1(3): 192–196.
- [28] F. Natterer. *Mathematical methods in image reconstruction*. Philadelphia: SIAM, 2001.
- [29] P.C. Hansen. *Rank-deficient and discrete ill-posed problems: numerical aspects of linear inversion*. Philadelphia: SIAM, 1998.
- [30] K. Lange, M. Bahn, and R. Little. A Theoretical Study of Some Maximum Likelihood Algorithms for Emission and Transmission Tomography. *IEEE Trans. Med. Imag.* 1987; 6(2): 106–114.
- [31] W. Van den Broek, S. Van Aert, and D. Van Dyck. A model based atomic resolution tomographic algorithm. *Ultramicroscopy* 2009; 109(12): 1485–1490.
- [32] J.J. Lifton, A. A. Malcolm, and J. W. McBride. The application of beam hardening correction for industrial X-ray computed tomography. *5th International Symposium on NDT in Aerospace* 2013.
- [33] W.J. Palenstijn, K.J. Batenburg, and J. Sijbers. Performance improvements for iterative electron tomography reconstruction using graphics processing units (GPUs). *J. Struct. Biol.* 2011; 176(2): 250–253.



---

## FILTERED BACKPROJECTION USING ALGEBRAIC FILTERS; APPLICATION TO BIOMEDICAL MICRO-CT DATA

---

*Abstract* – For computerized tomography (CT) imaging in (bio)-medical applications, radiation dose reduction is extremely important. This can be achieved simply by reducing the number of projection images taken. In order to obtain accurate reconstructions from few projections, however, common reconstruction techniques are not sufficient. Algebraic reconstruction methods (ARMs) are often more suited, but inflict a much higher computational burden. In this work, a recently proposed method is applied to biomedical  $\mu$ CT, in which the benefits of ARMs are combined with the computational efficiency of the common Filtered Backprojection (FBP) algorithm. Our experimental results demonstrate that this approach yields reconstructed images highly similar to those obtained by an ARM, while maintaining the favorable computational efficiency of FBP.

## 6.1 INTRODUCTION

*Computerized tomographic (CT) imaging* has many applications in clinical settings, in (bio)medical research, and in industry. In this chapter, we focus on the biomedical imaging task. For example, in osteoporosis research, reconstructions from  $\mu$ CT scanners are commonly used to perform a longitudinal analysis on the bone structures of small animals subjected to some form of treatment [1]. Due to the harmful nature of X-rays, radiation dose reduction is an important research goal for the community. One common way of reducing radiation is simply to take fewer projection images. This requires reconstruction methods that can handle such datasets well.

Two main types of reconstruction methods exist in the literature. *Analytical reconstruction methods* are based on a discretization of an exact inversion formula for the reconstruction problem. Well-known methods of this type are *Filtered Backprojection (FBP)* and *Feldkamp-David-Kress (FDK)*. These methods perform a filtering step of the measured data in the Fourier space with a predefined filter. Many standard filters are known from literature, such as the Ram-Lak, Hann and Cosine filter [2]. The optimal filter depends on the characteristics of the projection data, such as the signal to noise ratio and the number of projection angles. The main advantage of analytical methods is their high computational efficiency, which is why they are offered in nearly all commercial CT-scanner packages [3]. The downside of these methods, however, is their inflexibility to special scanning geometries and its inability to deal with insufficient data (e.g. when only few projections images are available).

*Algebraic reconstruction methods (ARM)* are typically much more robust with respect to incomplete or noisy projection data, due to their inherent ability to model the actual projection geometry of the scanning device. ARMs, such as SIRT, ART and CGLS [4], which compute a reconstruction by applying a sequence of update iterations, generally converge to a solution that is optimally consistent with the measured data, with respect to some norm. The drawback of these methods is their heavy computational burden compared to analytical methods. Moreover, the rapid improvement in detector technology is leading to ever larger volume sizes (i.e. higher resolution reconstructions) much faster than the advances in computational hardware can keep up with. Ideally therefore, one would like to combine the computational requi-

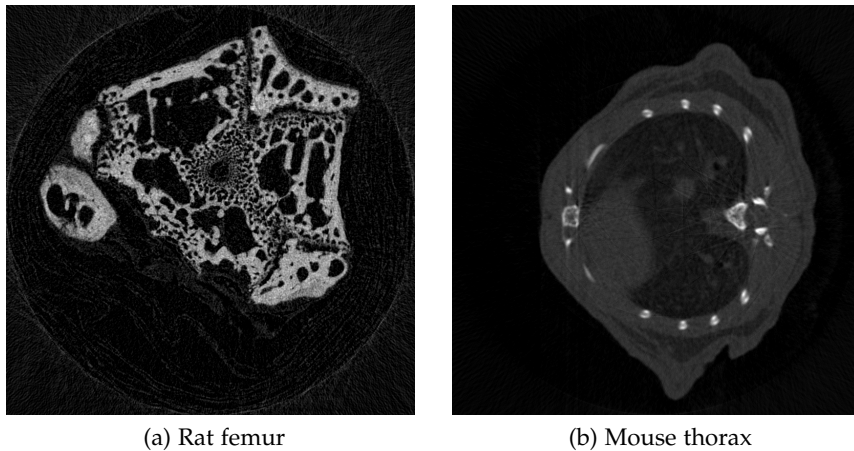


Figure 6.1: FBP reconstructions of two  $\mu$ CT scans using (a) 360 projection angles; (b) 225 projection angles.

rements of analytical methods with the robustness of algebraic methods. In [5], a method was described for developing filters for analytical methods that are based on the convergence behavior of a linear ARM. The reconstructions of FBP with these filters approximate the reconstructions of the corresponding ARM.

Many other methods have been developed to create optimal filters for FBP. Here, we mention only some recent work in the field. In [6], Zeng derives a filter in the frequency domain based on the Landweber algorithm. Nielsen et al. derive filters specifically for a tomosynthesis geometry [7]. Pelt and Batenburg use artificial neural networks to find good filters based on prior knowledge for datasets with a small number of projection angles [8]. They also provide a method to find filters such that the projection error is minimal [9]. In [10], Kunze et al. describe a method that also approximates an ARM. Opposed to the method described in [5], Kunze et al. need objects to obtain their filters.

In this chapter, we will apply the method from [5] to two sets of biomedical  $\mu$ CT data, that are acquired from a rat femur and a mouse thorax respectively. We aim to show the resemblance between SIRT and FBP that is obtained by using the custom filters from [5]. Reconstructions of the scanned objects using many projection angles are shown in

Fig. 6.1, where a display range was chosen to enhance visibility. The same range is used for all reconstructions in this chapter.

This chapter is structured as follows. In Sec. (6.2), the method from [5] is briefly described. Sec. (6.3) contains information on acquiring the experimental data and the experiments that are performed. The results are shown in Sec. (6.4). We discuss our findings and conclude this chapter in Sec. (6.5).

## 6.2 THE AF-FBP METHOD

This section contains a brief discussion of the *Algebraic Filter - Filtered Backprojection (AF-FBP)* reconstruction method. We first consider the Filtered Backprojection method and then explain the reasoning behind creating filters based on a linear ARM. For simplicity, we consider only a 2D parallel beam setup, but the concepts can be extended to other geometries as well.

FBP is a discretization of the inverse Radon transform, where the projection data  $\mathbf{p}$  is filtered by a filter  $g$  and then backprojected. The filter  $g : \mathbb{R}^2 \rightarrow \mathbb{R}$  can be chosen freely, depending on the experimental setup. The reconstruction formula for FBP is given by Eq. (6.1).

$$f(x, y) = \sum_{\theta \in \Theta} \sum_{\tau \in T} p_{\theta\tau} g(\theta, \tau - x \cos \theta - y \sin \theta), \quad (6.1)$$

where  $f : \mathbb{R}^2 \rightarrow \mathbb{R}$  is the unknown image,  $\Theta$  denotes the set of projection angles,  $T$  denotes the set of detector bins and  $\mathbf{p} \in \mathbb{R}^m$  with  $m = |\Theta| \cdot |T|$ .

The AF-FBP method generates angle-dependent filters  $g$  based on the convergence of a linear ARM [5]. For this chapter we use the iterative method SIRT. Since SIRT is a linear, stationary Richardson solver, there exists a reconstruction matrix  $\mathbf{R} : \mathbb{R}^m \rightarrow \mathbb{R}^n$  such that, for a fixed number of  $K$  iterations, the reconstruction  $\mathbf{u} \in \mathbb{R}^n$  of SIRT is given by  $\mathbf{u} = \mathbf{R}\mathbf{p}$ . By writing this equation element wise for a certain pixel  $c$  of  $\mathbf{u}$ , we obtain Eq. (6.2).

$$u_c = \sum_{\theta \in \Theta} \sum_{\tau \in T} r_{\theta\tau}^{(c)} p_{\theta\tau}, \quad (6.2)$$

where  $r^{(c)}$  denotes the  $c$ th row of  $\mathbf{R}$ .



Let the coordinates of the center of pixel  $c$  be denoted by  $(x_c, y_c) \in \mathbb{R} \times \mathbb{R}$ , then  $t_c^{(\theta)} = x_c \cos \theta + y_c \sin \theta$  is the projection of pixel  $c$  on the detector at angle  $\theta$ . For a variable  $\tau \in T - t_c^{(\theta)}$ , where the minus sign denotes element wise subtraction, we define a function  $h^{(c)} : \mathbb{R}^m \rightarrow \mathbb{R}$  by Eq. (6.3).

$$h^{(c)}(\theta, \tau) = r_{\theta(\tau + t_c^{(\theta)})}^{(c)}. \quad (6.3)$$

Combining Eq. (6.2) and Eq. (6.3) yields the formula in Eq. (6.4).

$$u_c = \sum_{\theta \in \Theta} \sum_{\tau \in T} p_{\theta\tau} h^{(c)}(\theta, \tau - x_c \cos \theta - y_c \sin \theta). \quad (6.4)$$

Hence for the central pixel  $c$ , the role of function  $h^{(c)}$  equals that of the filter  $g$  in Eq. (6.1). It has been shown in [5] that, for pixel  $c$  being the pixel at the center of the image grid, the use of the function  $h^{(c)}$  as a filter in the FBP method yields a good approximation of the linear ARM. We refer to  $h^{(c)}$  as an *algebraic filter*.

Each coefficient of the algebraic filter can be obtained by applying SIRT to projection data  $\mathbf{p}$  that equals a unit vector  $\mathbf{e}_{\theta\tau}$ , with entry one on position  $\theta\tau$  and zero otherwise. The resulting image pixel  $u_c$  will then equal  $r_{\theta\tau}^{(c)}$ ; see also Eq. (6.2). After applying this step for all unit vectors  $\mathbf{e}_{\theta\tau}$  with  $\theta \in \Theta$  and  $\tau \in T$ , the algebraic filter  $h^{(c)}$  can now be deduced from  $r^{(c)}$  by using Eq. (6.3).

The algebraic filter  $h^{(c)}$  can be applied to projection data in the same way as standard filters that are often used for FBP.

### 6.3 EXPERIMENTS

In this section, we describe experiments that we performed and define the measure that we use to examine the image quality of the reconstructions.

We consider the central slices of the two datasets depicted in Fig. 6.1. As the method AF-FBP is deduced for a parallel beam scanning geometry, the central slices were rebinned to parallel beam projection data. The first dataset concerns an ex-vivo scan of a rat femur, cross-sectioned at the epiphyseal plate, an area of interest for femur research. In total, 376 projection images were taken with a resolution of  $5\mu\text{m}$  in

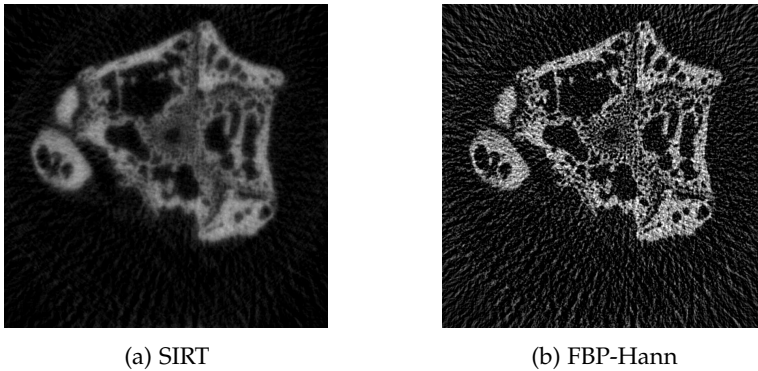


Figure 6.2: Reconstructions of femur projection data with 60 projection angles and SIRT with  $K = 50$  iterations.

a Bruker  $\mu$ CT SkyScan 1172 scanner running at 40kV. The second dataset concerns an in-vivo scan of a mouse, cross-sectioned at the thorax. Its 451 projections of resolution  $34\mu\text{m}$  were taken in a Bruker  $\mu$ CT SkyScan 1076 system running at 59kV. For both datasets, the SkyScan NRecon software was used for data preprocessing and beam hardening correction. To emulate low dose scans, we selected 45 and 60 projection angles from both scans.

In the experiments, we apply the SIRT-FBP method (FBP with an algebraic filter based on SIRT) to the above mentioned datasets. The aim of SIRT-FBP is to approximate the SIRT reconstruction. We will first consider the reconstructions of SIRT and FBP with a standard filter. They are shown for the femur dataset in Fig. 6.2, where SIRT is performed with  $K = 50$  iterations and the Hann filter is chosen as the standard filter for FBP. The reconstructions of SIRT and FBP-Hann (FBP with a standard Hann filter) have characteristic imaging features. The SIRT reconstruction is a smoothed image, while the FBP-Hann reconstruction contains extensive streaking artifacts. Furthermore, the heavy computational burden of SIRT can be a reason to choose FBP, even when a researcher would favor the reconstruction quality of SIRT over FBP. In those situations, SIRT-FBP could be applied, which yields an approximation of SIRT with comparable computation time as FBP with standard filters.

In all experiments, the number of detector bins is  $D = 799$ . The reconstruction grid is a square, consisting of  $D \times D$  pixels of unit size. The number of iterations for SIRT is  $K = 50$ , unless stated differently. The forward projections that are needed to execute SIRT are obtained using the Joseph kernel [11]. For the calculations in this chapter we use the ASTRA toolbox [12].

### 6.3.1 Quality measure

The quality of the reconstructions is examined by comparing the reconstructions with the SIRT reconstruction, since the aim of SIRT-FBP is to approximate SIRT. The reconstructions are compared on the reconstruction grid of  $D \times D$  pixels. Denote a reconstruction by  $\mathbf{u} = (u_{kl})$  with  $1 \leq k, l \leq D$ . Furthermore, let the algebraic reconstruction be denoted by  $\mathbf{u}^{\text{ARM}} = (u_{kl}^{\text{ARM}})$ . Then the *mean ARM reconstruction error* is defined as

$$E_r^{\text{ARM}} = \frac{\sum_{k,l} |u_{kl} - u_{kl}^{\text{ARM}}|}{\sum_{k,l} u_{kl}^{\text{ARM}}}. \quad (6.5)$$

Hence  $E_r^{\text{ARM}}$  is an  $L_1$ -norm in the object space combined with a scaling term. We assume that the set of projection data is nonnegative and that  $\mathbf{u}^{\text{ARM}}$  is nonzero.

## 6.4 RESULTS

In this section, we show the results of the experiments described in Sec. (6.3). We emphasize that the purpose of AF-FBP is to approximate the quality of the corresponding ARM reconstructions, instead of improving the overall reconstruction quality.

In Fig. 6.3 we show the reconstructions of the femur dataset for SIRT, SIRT-FBP, FBP-RL (FBP with a standard Ram-Lak filter) and FBP-Cos (FBP with a standard Cosine filter). The number of projection angles is  $d = 60$  and the number of SIRT iterations is  $K = 50$ . For the reconstruction of FBP-Hann (FBP with a standard Hann filter) we refer to Fig. 6.2. Notice the resemblance between the SIRT and SIRT-FBP reconstruction, and the streak artifacts for FBP-RL and FBP-Cos which are much more pronounced.

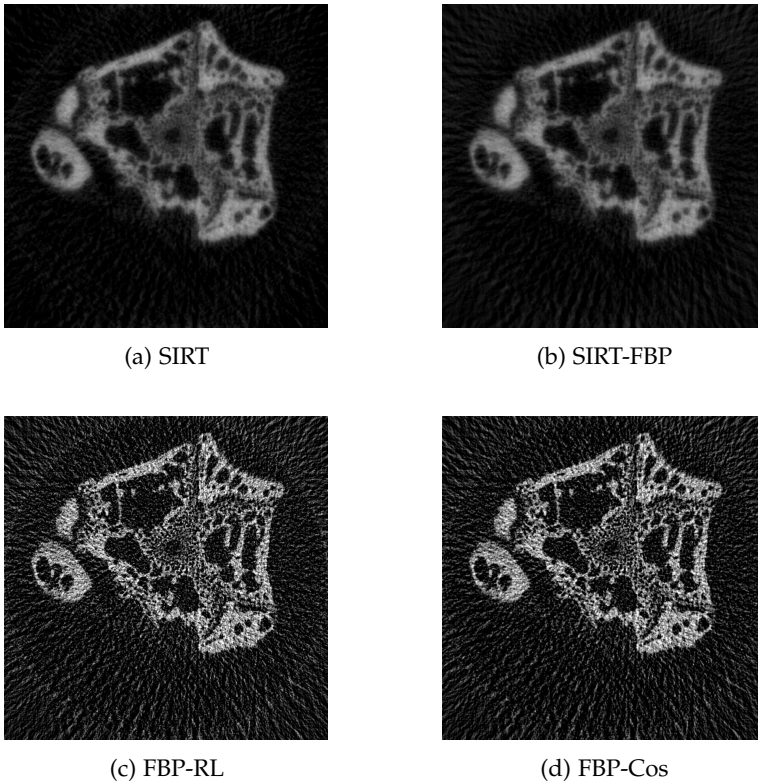


Figure 6.3: Reconstructions of femur projection data with 60 projection angles and SIRT with  $K = 50$  iterations.

We use the mean ARM reconstruction error (see Sect. 6.3.1) to compare the reconstructions. The results are shown in Table 6.1. The  $E_r^{\text{ARM}}$  for SIRT-FBP is significantly smaller than that of FBP with standard filters. This implies that SIRT-FBP approximates the SIRT reconstruction, while FBP reconstructions with standard filters differ substantially from SIRT reconstructions.

We obtain similar results for a different number of iterations  $K$  in the range from 10 to 1000, although the differences in  $E_r^{\text{ARM}}$  decrease for increasing  $K$ .

<i>Class</i>	<i>SIRT-FBP</i>	<i>FBP-RL</i>	<i>FBP-Hann</i>	<i>FBP-Cos</i>
<b>45 projection angles</b>				
femur	0.18	1.6	1.3	1.4
thorax	0.13	0.50	0.43	0.46
<b>60 projection angles</b>				
femur	0.17	1.3	1.1	1.2
thorax	0.12	0.42	0.36	0.38

Table 6.1: Mean ARM reconstruction errors  $E_r^{\text{ARM}}$  for  $K = 50$ .

## 6.5 CONCLUSIONS AND DISCUSSION

We introduced the method AF-FBP, which uses custom filters that are created based on a linear ARM. The reconstructions of AF-FBP approximate the reconstructions of the ARM that was used to create the filters. This was already shown in earlier work for simulated data [5]. In this work, we have applied this new method to experimental biomedical  $\mu$ CT data for the first time. Our results demonstrate that reconstructions approximating the image quality of SIRT can now be created with the computationally fast FBP method.

In this chapter we have focused on the image quality of AF-FBP compared to SIRT, because SIRT-FBP is designed to approximate SIRT. Whether it is advantageous to use SIRT (or SIRT-FBP) instead of FBP with other filters depends on the application and the features that are desirable for the particular imaging task. In future work, we will investigate how other algebraic methods – that are capable of incorporating prior knowledge or particular noise models – can be approximated following a similar approach.

## BIBLIOGRAPHY

- [1] E. Perilli et al. Detecting early bone changes using in vivo micro-CT in ovariectomized, zoledronic acid-treated, and sham-operated rats. *Osteoporosis International* 2010; 21(8): 1371–1382.
- [2] A.C. Kak and M. Slaney. *Principles of Computerized Tomographic Imaging*. Philadelphia: SIAM, 2001.
- [3] X. Pan, E. Y. Sidky, and M. Vannier. Why do commercial CT scanners still employ traditional, filtered back-projection for image reconstruction? *Inv. Problems* 2009; 25(12): 123009.
- [4] J. Gregor and T. Benson. Computational analysis and improvement of SIRT. *IEEE Trans. Med. Imag.* 2008; 27(7): 918–924.
- [5] K.J. Batenburg and L. Plantagie. Fast Approximation of Algebraic Reconstruction Methods for Tomography. *IEEE Trans. Image Process.* 2012; 21(8): 3648–3658.
- [6] G.L. Zeng. A filtered backprojection algorithm with characteristics of the iterative Landweber algorithm. *Med. Phys.* 2012; 39(2): 603–607.
- [7] T. Nielsen et al. Filter Calculation for X-Ray Tomosynthesis Reconstruction. *Phys. Med. Biol* 2012; 57(12): 3915–3930.
- [8] D.M. Pelt and K.J. Batenburg. Fast tomographic reconstruction from limited data using artificial neural networks. *IEEE Trans. Image Process.* 2013; 22(12): 5238–5251.
- [9] D.M. Pelt and K.J. Batenburg. Improving Filtered Backprojection Reconstruction by Data-Dependent Filtering. *IEEE Trans. Image Process.* 2014; 23(11): 4750–4762.
- [10] H. Kunze et al. Filter determination for Tomosynthesis aided by iterative reconstruction techniques. *Proc. of Fully3D* 2007: 309–312.
- [11] P.M. Joseph. An improved algorithm for reprojecting rays through pixel images. *IEEE Trans. Med. Imag.* 1982; 1(3): 192–196.
- [12] W.J. Palenstijn, K.J. Batenburg, and J. Sijbers. Performance improvements for iterative electron tomography reconstruction using graphics processing units (GPUs). *J. Struct. Biol.* 2011; 176(2): 250–253.

---

## THE ACCURACY OF FBP WITH RECENTLY INTRODUCED FILTERS: A COMPARISON

---

### 7.1 INTRODUCTION

The field of *Computerized tomography* (CT) focuses on reconstructing an image of a scanned object from its projections. Projection data are obtained using a scanning device, for example using X-rays (CT-scanning) or electrons (electron microscopy). The size of objects that can be scanned by tomography varies from nanometers in electron tomography to kilometers in seismic tomography [1–4].

In many tomography applications, such as medical and industrial imaging, finding an exact reconstruction is not possible due to the size of the reconstruction problem and due to inconsistent projection data. Therefore, many algorithms have been developed that approximate the scanned object. Two common categories of such methods are the algebraic reconstruction methods and the analytical reconstruction methods.

The *algebraic reconstruction methods* (ARMs) use a discrete representation of the tomographic reconstruction problem. This approach often involves iterative reconstruction techniques to solve the system of linear equations. Examples of these methods are the Kaczmarz method which is also known as the algebraic reconstruction technique (ART) and the simultaneous iterative reconstruction technique (SIRT). Also expectation maximization (EM) is a well-known iterative recon-

---

The author would like to acknowledge Dr. D.M. Pelt from the Centrum Wiskunde & Informatica, Amsterdam, The Netherlands, for developing the software that was used to generate the reconstructions for the experiments in this chapter and for his useful textual comments.

struction method [5, 6]. Algebraic reconstruction methods are well-suited for incorporating certain types of prior knowledge. These methods are preferred for limited-data problems, for example if only projections from few angles are available, or if the projections have a limited angular range. A disadvantage of algebraic methods is their high computational burden, which can become a bottleneck if large objects, or a large number of objects, have to be reconstructed in a short period of time.

The *analytical reconstruction methods* are based on a continuous representation of the tomographic reconstruction problem. The *Filtered Backprojection* algorithm (FBP) is a commonly used reconstruction method in CT imaging. It is a computationally fast reconstruction method, since it only requires a filtering step followed by a backprojection step. For low-noise projection data with a substantial number of equiangularly distributed projection angles, FBP is known to produce accurate reconstructions.

Due to the computational efficiency of FBP, extensive efforts have been made to improve the quality of its reconstructions for situations where FBP is known to produce poor quality reconstructions. This reconstruction quality depends strongly on the filters that are used in the FBP algorithm. Choosing the optimal filter for a particular reconstruction problem is not straightforward and often some standard variation on the Ramp filter is used. Many methods have recently been published to create filters for FBP. In this chapter we will compare methods that can be used in 2D parallel-beam tomography.

New filters can be obtained from theoretical derivations, as shown by Zeng [7]. Other methods, such as OFBP [8] and AF-FBP [9], create new filters using information from algebraic reconstruction methods and thereby incorporating the geometry of the reconstruction problem in the filters. Applying neural networks is another approach to obtaining filters for FBP, as shown by Pelt and Batenburg [10]. Pelt and Batenburg also introduce the method MR-FBP [11], where the filter depends on the measured projection data.

Also in the field of tomosynthesis, creating better filters for FBP has been a topic of interest. An example is OFBP, which was already mentioned above. Also Godfrey et al. [12] and Nielsen et al. [13] have recently introduced new filter methods for FBP. Since these algorithms cannot be translated into parallel-beam tomography, as opposed to OFBP, they will not be included in this chapter.



In this chapter, we will provide an overview of recently proposed methods to compute filters for the FBP algorithm. While the original descriptions of these methods are quite diverse, we formulate a common framework in which each of these methods can be expressed in a straightforward way. After an introduction to the various methods covered in this chapter, we will provide an analysis of the characteristic properties of each method. An illustration of the results obtained from the various filter methods is subsequently provided through a series of simulation experiments. We conclude this chapter with discussion and conclusions.

## 7.2 METHODS

In this section, we first describe the geometry that will be used in this chapter and the FBP method with standard filters. Then we give a short description of the methods that will be compared throughout this chapter.

We consider a parallel-beam geometry with a monochromatic X-ray source rotating in a circular trajectory around the object. The object is represented as a function  $f : \mathbb{R}^2 \rightarrow \mathbb{R}$ . We denote the set of projection angles by  $\Theta$  with  $N_\Theta = |\Theta|$ , and the set of detector bins by  $T$  with  $N_T = |T|$ . Define  $N_{T\Theta} = N_T N_\Theta$ . Furthermore we denote the projections by  $\mathbf{p} \in \mathbb{R}^{N_{T\Theta}}$ .

We assume that the measured projections are related to the object  $f$  by the continuous Radon transform, given in Eq. (7.1).

$$p(\theta, t) = (\mathcal{R}f)(\theta, t) = \int_{-\infty}^{\infty} f(t \cos \theta - s \sin \theta, t \sin \theta + s \cos \theta) ds \quad (7.1)$$

So, for each projection angle  $\theta \in \Theta$ , we obtain the value of the Radon transform for a discrete set of detector coordinates  $T$ . The *reconstruction problem* then consists of recovering the function  $f$  from this set of measurements.

In algebraic methods, the domain of  $f$  is discretized as a discrete (typically square) set of  $N \times N$  pixels, forming a vector of  $N^2$  pixel values. Similarly, the measured projections are represented by a vector of

size  $N_{T\Theta}$ . This leads to the following discretized version of the reconstruction problem:

$$\mathbf{W}\mathbf{x} = \mathbf{p}. \quad (7.2)$$

In this system of linear equations, the vector  $\mathbf{x}$  represents the unknown object, the vector  $\mathbf{p}$  represents the combined projection data for all angles, and the projection matrix  $\mathbf{W}$  models a discretization of the Radon transform, defining the relationship between  $\mathbf{x}$  and  $\mathbf{p}$ .

This chapter deals with *filtered backprojection* methods, which can all be written as

$$\mathbf{u} = \mathbf{W}^T \mathbf{H} \mathbf{p}, \quad (7.3)$$

where  $\mathbf{u} \in \mathbb{R}^{N^2}$  denotes a vector containing the  $N \times N$ -reconstruction,  $\mathbf{W}^T$  denotes the *transpose* of the projection matrix (also known as the backprojection operator), and  $\mathbf{H} \in \mathbb{R}^{N_{T\Theta} \times N_{T\Theta}}$  denotes some filter matrix. The particular choice of the filter matrix  $\mathbf{H}$  defines the reconstruction algorithm. In the following subsections we will introduce a series of filtered backprojection methods that have been proposed in the literature.

### 7.2.1 FBP

We first briefly comment on the FBP method itself. We recall that the Radon transform in Eq. (7.1) has an exact inversion formula given by Eq. (7.4).

$$f(x, y) = \int_0^\pi \int_{-\infty}^{\infty} p(\theta, \tau) g(\theta, t - \tau) d\tau d\theta, \quad (7.4)$$

where  $g : \mathbb{R}^2 \rightarrow \mathbb{R}$  is the inverse Fourier transform of the *Ramp filter*  $G(\theta, q) = |q|$ .

The FBP method is obtained by discretizing Eq. (7.4), as follows:

$$f(x, y) = \sum_{\theta \in \Theta} \sum_{\tau \in T} p_{\theta\tau} g(\theta, \tau - x \cos \theta - y \sin \theta). \quad (7.5)$$

Hence FBP can be written in the form of Eq. (7.3), where  $\mathbf{H}$  is defined by the filters  $g$ . The actual filter that is used in FBP does not have to be

the Ramp filter. In fact, each of the methods that we will cover in this chapter uses a different filter  $g$ .

### 7.2.2 Standard filters for FBP

There are several common filters for FBP, which will be called *standard filters* here. These filters are variations of the Ramp filter. The Ramp filter itself is not commonly used, since it amplifies the noise in the high frequencies, resulting in a poor reconstruction quality. Therefore, frequency windows are applied to the Ramp filter.

A well-known filter was proposed by Ramachandran and Lakshminarayanan. It uses a simple windowing function, as shown in Eq. (7.6) [2, 14]. We refer to this filter as the *Ram-Lak* filter.

$$G(\theta, q) = |q| \text{rect}(q). \quad (7.6)$$

Other, more smooth filter functions are the *Cosine* filter and the *Hann* filter, see Eq. (7.7) and Eq. (7.8) respectively.

$$G(\theta, q) = |q| \text{rect}(q) \cos(\pi q/2), \quad (7.7)$$

$$G(\theta, q) = |q| \text{rect}(q) (0.5 - 0.5 \cos(2\pi q)). \quad (7.8)$$

The latter two functions aim at smoothening the edges of the Ram-Lak filter. The advantage of the Cosine and Hann filter is that they reduce image noise. A disadvantage is that they do not preserve edges in the image.

A major advantage of the FBP method with such a standard filter is its computational efficiency. The complexity of the filtering step in the Fourier space is  $\mathcal{O}(N_{T\Theta} \log N_T)$  and a backprojection operation is  $\mathcal{O}(N_T N^2)$ . The standard filters are independent of both the object to be scanned and the geometry that is used, including the number of projection angles and the size of the reconstruction grid. A drawback is that no prior knowledge can be incorporated. Furthermore, FBP with standard filters is known to perform poorly in case of a missing wedge or limited number of projection angles.

### 7.2.3 MR-FBP

The method minimal residual filtered backprojection (MR-FBP) is proposed by Pelt and Batenburg (2014). It is designed for limited-data problems and it aims at finding the filter that minimizes the projection error of the resulting reconstruction, i.e. the difference between the forward projection of the reconstruction and the projection data  $\mathbf{p}$ .

FBP consists of a filtering step, which is a convolution of the projection data  $\mathbf{p}$  by some filter, followed by a backprojection. As argued in [11], FBP can also be written as a convolution of some filter  $\mathbf{h}$  by  $\mathbf{p}$ , followed by a backprojection operation, see Eq. (7.9).

$$\text{FBP}_{\mathbf{h}}(\mathbf{p}) = \mathbf{W}^T \mathbf{C}_{\mathbf{p}} \mathbf{h}, \quad (7.9)$$

where  $\text{FBP}_{\mathbf{h}}$  denotes FBP with the filter  $\mathbf{h}$  applied,  $\mathbf{W}^T$  is the backprojection, and the matrix  $\mathbf{C}_{\mathbf{p}}$  is the convolution by  $\mathbf{p}$ . The filter  $\mathbf{h}$  is chosen such that it minimizes the squared difference between the forward projection of the reconstruction and the measured projection data.

$$\mathbf{h}^* = \underset{\mathbf{h}}{\text{argmin}}[\mathbf{p} - \mathbf{W}\mathbf{W}^T \mathbf{C}_{\mathbf{p}} \mathbf{h}]^2. \quad (7.10)$$

Exponential binning is used to reduce the number of unknowns for the filter  $\mathbf{h}$  [11]. The resulting MR-FBP algorithm requires the computation of  $\mathcal{O}(\log N_T)$  projection operations and the total computation time is  $\mathcal{O}(N_{\Theta} N^2 \log N_T + N_{T\Theta} [\log N_T]^2)$  for  $N_T \approx N$ .

The filter  $\mathbf{h}^*$  is designed to minimize the residual in Eq. (7.10). It determines the filter as part of the reconstruction algorithm, since the optimal filter depends on both the object to be scanned and the scanning geometry. Therefore, the geometry can be altered during the experiments, as opposed to some other reconstruction methods discussed in this chapter. It is also possible for this method to incorporate prior knowledge for example by adding a regularization term to Eq. (7.10). Determining the filter is relatively fast and various scanning geometries can be used.

A disadvantage of MR-FBP is that it is less suited for creating large numbers of reconstructions with the same geometry, because the filter depends on the measured projection data. The filter therefore changes for every scanned object.

## 7.2.4 AF-FBP

Filters for FBP can also be created using a linear algebraic reconstruction method (ARM). In [9], Batenburg and Plantagie introduce the method algebraic filter - filtered backprojection (AF-FBP). They use the simultaneous iterative reconstruction technique (SIRT) to demonstrate the characteristics of this method. We will follow this approach here.

For any linear algebraic reconstruction method, there exists a transformation matrix  $\mathbf{R} \in \mathbb{R}^{N^2 \times N_{T\Theta}}$  such that  $\mathbf{u} = \mathbf{R}\mathbf{p}$ . For some pixel  $c$  of the reconstruction grid, denoted by  $(x_c, y_c)$ , define its projection onto the detector by  $t_c^{(\theta)} = x_c \cos \theta + y_c \sin \theta$  for  $\theta \in \Theta$ . Furthermore, let  $\mathbf{r}^{(c)}$  denote the  $c$ th row of  $\mathbf{R}$  and  $r_{\theta\tau}^{(c)}$  the entry of this row corresponding to angle  $\theta$  and detector element  $\tau \in T$ . It is shown in [9] that there exists a function  $h^{(c)}$  such that

$$u_c = \sum_{\theta \in \Theta} \sum_{\tau \in T} p_{\theta\tau} h^{(c)}(\theta, \tau - t_c^{(\theta)}). \quad (7.11)$$

When  $c$  is chosen such that it is the central pixel of the reconstruction grid, then  $h^{(c)}$  can be expressed as  $\mathbf{R}$  applied to a set of unit vectors  $\mathbf{e}_{\theta\tau}$  with value 1 at position  $(\theta, \tau)$  and value 0 otherwise, see Eq. (7.12).

$$h_{\theta\tau}^{(c)} = [\mathbf{R}\mathbf{e}_{\theta\tau}]_c, \quad \forall \theta \in \Theta, \tau \in T. \quad (7.12)$$

This angle dependent filter is then applied to obtain all image pixels of the reconstruction. As shown in [9], the characteristics of these reconstructions resemble those of the linear ARM that was used to create the filters. The reconstruction time is however significantly reduced compared to that of the ARM, since FBP can be used for the reconstruction. This is advantageous in situations with only few projection angles or limited projection range, where an ARM in general gives more accurate reconstructions than FBP with standard filters. When the computational burden of ARMs prevents the use of such an ARM, AF-FBP could be a good alternative. Another advantage of AF-FBP is that certain types of prior knowledge can be incorporated when creating the filters.

A disadvantage of AF-FBP is the time that is needed to create its filters. It takes  $\mathcal{O}(N_{T\Theta})$  ARM reconstructions to obtain this filter. Howe-

ver, since the filter is object independent, these calculations need only be executed once for a given geometry. Furthermore, not all ARMs are suitable for AF-FBP, since only linear ARMs can be used. The geometry is currently limited to 2D parallel beam. Several parameters need to be set in advance, such as the pixel  $c$  and the number of iterations  $k$ . Also a relaxation parameter  $\omega$  needs to be chosen, which is contained in SIRT.

### 7.2.5 Zeng

In [7], Zeng uses the algebraic Landweber algorithm to obtain a filter for FBP. The Landweber algorithm is an iterative algebraic reconstruction method that solves the system of linear equations  $\mathbf{W}\mathbf{x} = \mathbf{p}$  to obtain the minimum least squares solution. It is equivalent to SIRT that is used by AF-FBP. The  $k$ th iteration step of the Landweber algorithm is given by Eq. (7.13).

$$\mathbf{x}^{(k+1)} = \mathbf{x}^{(k)} + \omega \mathbf{W}^T (\mathbf{p} - \mathbf{W}\mathbf{x}^{(k)}), \quad (7.13)$$

where  $\omega$  is a relaxation parameter. Zeng describes a method to obtain a filter in the frequency domain based on this Landweber algorithm. The filter can be used in the FBP method.

The first step to deduce the formula for this filter, is to rewrite Eq. (7.13) into the form in Eq. (7.14), where  $\mathbf{x}^{(0)}$  is assumed to equal zero and  $k$  is finite.

$$\mathbf{x}^{(k)} = (\mathbf{W}^T \mathbf{W})^{-1} [\mathbf{I} - (\mathbf{I} - \omega \mathbf{W}^T \mathbf{W})^k] \mathbf{W}^T \mathbf{p}, \quad (7.14)$$

where  $\mathbf{I}$  denotes the identity matrix.

It is shown by Zeng that the impulse-response of the matrix  $\mathbf{W}^T \mathbf{W}$ , determined in the central region of the reconstruction grid, behaves approximately as  $1/r$ . This means that if we move away from the central pixel along radial lines, the intensity observed decays as  $1/r$ . Furthermore, the 1D Ramp filter is a good approximation of the operation  $(\mathbf{W}^T \mathbf{W})^{-1}$ . Hence the filter in 1D Fourier space is given by Eq. (7.15).

$$H_k(v_t) = |v_t| \left[ 1 - \left( 1 - \frac{\omega}{|v_t|} \right)^k \right], \quad (7.15)$$

where  $v_t$  denotes the spatial frequency with respect to the detector.

When we compare the filter in Eq. (7.15) with the general form in Eq. (7.3), we see that the filter  $\mathbf{H}$  is given by a 1D Fourier transform of  $\mathbf{p}$  followed by applying the windowed ramp filter  $H_k$  and a 1D inverse Fourier transform of this filtered data.

An advantage of this method is that the computational burden to obtain the filter is low. Furthermore, the filter can be obtained for a variety of geometries and is independent of the object to be scanned.

This method is specifically designed to approximate the Landweber algorithm. It is therefore not directly applicable to other algebraic reconstruction methods. It requires the start solution  $\mathbf{x}^{(0)}$  to be equal to zero and the number of iterations  $k$  has to be chosen in advance. The parameter  $\omega$  needs to be chosen appropriately, since a value exceeding  $2/\sigma_{\max}$ , with  $\sigma_{\max}$  the largest singular value of  $\mathbf{W}^T\mathbf{W}$ , results in a diverging algorithm, while the rate of convergence decreases with a decreasing  $\omega$ .

### 7.2.6 OFBP

Filters for FBP can also be created based on the impulse response of an algebraic reconstruction algorithm, as observed by scanning a very thin object on the detector. The method optimized filtered back-projection (OFBP) is an example of such a method. It is described by Kunze et al. in 2007 for breast tomosynthesis, with typically few projection angles and a limited angular range[8].

The iterative reconstruction method SIRT is used to derive a method to obtain filters for FBP. Kunze et al. derive an iterative method called *corrected projections simultaneous iterative reconstruction techniques* (P-SIRT) which has its update step in the projection space followed by a backprojection, see Eq. (7.16).

$$\begin{aligned}\mathbf{p}^{(k+1)} &= \mathbf{p}^{(k)} + \mathbf{p} - \mathbf{W}\omega\mathbf{W}^T\mathbf{p}^{(k)}, \\ \mathbf{u}^{(k+1)} &= \omega\mathbf{W}^T\mathbf{p}^{(k+1)},\end{aligned}\tag{7.16}$$

where  $\omega$  is a relaxation parameter. The initial parameter  $\mathbf{p}^{(0)}$  equals the measured projection data  $\mathbf{p}$ .

In the limit case  $k \rightarrow \infty$ , a reconstruction of P-SIRT is given by Eq. (7.17).

$$\mathbf{u}^{(\infty)} = \omega \mathbf{W}^T (\mathbf{W} \omega \mathbf{W}^T)^{-1} \mathbf{p}, \quad (7.17)$$

The matrix  $\mathbf{H} = \omega (\mathbf{W} \omega \mathbf{W}^T)^{-1}$  acts as a filter on the projection data.

Exact inversion of this matrix is difficult to perform due to the large scale of the problem. Kunze et al. approximate this inversion by simulating Dirac-line-functions using thin wires to determine the impulse responses. These impulse responses are then used as the corresponding angle-dependent filters for FBP.

Kunze et al. use three thin wires to determine three impulse responses. These impulse responses are then averaged to obtain the filters. The impulse response is assumed to have finite support and to be shift invariant within a projection angle. The distance between the wires should be large enough to avoid overlapping of the impulse responses. It is shown in [8] that the impulse responses for the top, middle and end of a wire are very similar, hence no averaging is needed in the direction of the wire. The impulse response corresponding to the middle of the wire is used for the filters. It is furthermore assumed that the filters created using these wires are independent for each projection angle.

An advantage of this method is that the computational burden to create the filters is low. Furthermore, since the filters are object independent, the filters need only be determined once for a given geometry and scanning device. With this method it is possible to incorporate prior knowledge when determining the filters.

A disadvantage of the method is that it is designed to approximate P-SIRT only. It is not possible to create filters with this method that can be used to approximate other algebraic reconstruction methods. Furthermore, as opposed to the other methods presented here, a specific object needs to be scanned to be able to determine the impulse responses, i.e. the three thin wires. As a result, the filters depend on the geometry and on the scanning device that is used to create the filters. Parameters that need to be chosen are the number of iterations, the thickness and position of the wires, the supersampling and interpolations that need to be used.



## 7.2.7 INN-FBP

A different approach for solving the CT reconstruction problems is by using neural networks. In [10] the neural network filtered backprojection method (NN-FBP) is introduced. The NN-FBP method consists of two stages: a *training stage* and a *reconstruction stage*. For the training stage, a series of high quality images of typical objects is required, along with their projections. It is important that these images are representative for the objects that will be reconstructed later on, in the reconstruction stage. In the training stage, a *supervised learning algorithm* is employed, to derive a set of filters such that the reconstructed pixel values for the training set are as similar as possible to the high quality test images. This learning algorithm is based on neural network theory. More concrete, the neural network is modeled as a multilayer perceptron. It consists of a layer of input nodes  $\mathbf{z}$ , a weight matrix  $\hat{\mathbf{W}}$ , a layer of hidden nodes  $\hat{\mathbf{h}}$ , an activation function  $\sigma$  that is applied to the output of each node, and a second weight matrix  $\mathbf{Q}$ . With appropriate choices of the variables, this network can be written as a weighted sum of Filtered Backprojections. As a full description of the network model is outside the scope of our current description, we refer to [10] for the exact details. By reducing the number of hidden nodes in the network to one, and choosing a linear activation function  $\sigma$  equal to the identity function, the neural network can even be written as a single filtered backprojection operation as shown in Eq. (7.18). We refer to this method as linear NN-FBP (INN-FBP).

$$n_{\mathbf{Q},\hat{\mathbf{H}}}(\mathbf{z}) = q_0 \text{FBP}_{\hat{\mathbf{h}}_0}(x, y) = [\hat{\mathbf{W}}^T q_0 \hat{\mathbf{h}}_0 \mathbf{p}]_{(x,y)}, \quad (7.18)$$

where the function  $n_{\mathbf{Q},\hat{\mathbf{H}}}(\mathbf{z})$  defines the value of a single reconstructed pixel  $(x, y)$ , based on the network parameters  $\mathbf{Q}$  and  $\hat{\mathbf{H}}$ , and on the input projection data  $\mathbf{z}$ . The input values for  $\mathbf{z}$  are derived from the projection data after a translation and reflection operation.

Pelt and Batenburg use an independent validation set during the training phase to avoid overfitting. After obtaining the optimal values  $q_0^*$  and  $\hat{\mathbf{h}}_0^*$  for  $q_0$  and  $\hat{\mathbf{h}}_0$  respectively, and due to the shift invariance of FBP, a reconstruction with INN-FBP is obtained from a single FBP with filter  $\mathbf{h} = q_0^* \hat{\mathbf{h}}_0^*$  applied to the projection data. This filter is angle independent. The computational complexity of the reconstruction part of INN-FBP with one hidden node equals  $\mathcal{O}(N_{\Theta} N^2)$ .

For INN-FBP a large training set of images is needed. If there is prior knowledge available of the object to be scanned, then this can be incorporated by the choice of this training set. An additional advantage of this method is that the optimal filters need only be computed once for a given training set. Furthermore, since FBP is shift-invariant, the filter calculation need not be repeated for every pixel of the reconstruction. The method is described here for a 2D scanning geometry. It is however also suitable for extension to 3D scanning geometries.

A drawback of the method is that the object to be scanned needs to be close enough to the training set, otherwise the parameters  $\mathbf{Q}$  and  $\hat{\mathbf{H}}$  are no longer accurate to minimize the squared difference between the reconstruction and the original object. Furthermore, the quality of the reconstructions depends on several decisions which have to be made in advance. These include the size of the training set and the method to obtain correct outputs (i.e. FBP with a standard filter or an algebraic reconstruction method with a high number of projection angles). It is furthermore known from literature that linear NN-FBP is less accurate than a normal NN-FBP with multiple nodes and with a nonlinear activation function  $\sigma$ .

### 7.2.8 Characteristics

We conclude this section with a brief overview of the main characteristics of the reconstruction methods that have been introduced above.

The first characteristic that we consider is the ability to handle few projection angles, see also Table 7.1. The standard filters for FBP and the method of Zeng are known to produce poor quality reconstructions for these datasets, while MR-FBP, AF-FBP, OFBP and INN-FBP can handle this input much better since they create filters based on an explicit model of the projection angles that are actually available.

The ability to handle noisy projection data varies amongst the different filter methods. The Ram-Lak filter amplifies high frequencies and thus noise. The Cosine and Hann filters do not amplify these high frequencies and can handle noisy data better. MR-FBP, AF-FBP, OFBP and INN-FBP perform better in reducing noise than FBP with standard filters. According to its inventor, the filter of Zeng depends on the index  $k$  which is the number of iterations in the Landweber method. For low  $k$  the noise is reduced while for high  $k$  the resolution increases and

Method	FBP-RL	FBP-Cos	FBP-Hann	MR-FBP	AF-FBP	Zeng	OFBP	INN-FBP
Handling few projection angles	-	-	-	+	+	-	+	+
Noise reduction	--	-	-	+	+	+/-	+	+
Prior knowledge	-	-	-	+/-	+/-	-	+/-	+
Variable geometry	v	v	v	v	x	v	x	x
Preprocessing time	+	+	+	+	-	+	+/-	-
Reconstruction time	+	+	+	+/-	+	+	+	+
Requiring a training set	x	x	x	x	x	x	x	v
Requiring a phantom for the filter	x	x	x	x	x	x	v	x
Filter depends on the object	x	x	x	v	x	x	x	x

Table 7.1: Characteristics of the different filtering methods; v = yes, x = no, - (--) = (very) incapable or slow, + = capable or fast, +/- = intermediate.

the noise is amplified. The results of OFBP and AF-FBP also depend on the parameter  $k$ .

The methods MR-FBP, AF-FBP, OFBP and INN-FBP are suitable to incorporate some types of prior knowledge of the scanned object by using an L2 regularization. For INN-FBP more object specific information can be incorporated in the training stage.

The geometry can be chosen freely for FBP with standard filters, MR-FBP and Zeng. For the other methods the filters are created based on a certain geometry. When the number of projection angles or the size of the detector or reconstruction grid changes, new filters should be calculated based on this new geometry.

The total reconstruction time can be split into two parts: a *preprocessing time*, where the filters are calculated once for a given geometry, and a *reconstruction time*, where the actual reconstruction method is applied. The preprocessing time depends on the parameters that are used. For INN-FBP, this step consists of the training stage and depends on both the geometry and the size of the training set. For AF-FBP the preprocessing time depends on the algebraic method that is used

and the geometry. The method OFBP requires only a small amount of preprocessing time compared to AF-FBP and INN-FBP. The other methods do not require processing time or they calculate a filter based on the projection data of the scanned object. The time required for these calculations is included in the reconstruction time. Therefore, the reconstruction time of MR-FBP is high compared to that of the other methods.

The last three characteristics concern additional elements that are required for the preprocessing step. The method INN-FBP requires a training set to be able to compute the filter, OFBP requires a phantom (in 3D three thin rods) to calculate the filter, and filters from MR-FBP depend on the scanned object.

### 7.3 EXPERIMENTS

In this section we describe the experiments that were performed and the choices that were made to implement the reconstruction methods. We compare the reconstruction time and preprocessing time of the different reconstruction methods. We also compare the quality of the reconstructions with the phantom using both the mean square error (MSE) and the structural similarity index (SSIM) for varying numbers of projection angles and for varying amounts of Poisson noise (expressed by the detector count  $I_0$ ).

#### 7.3.1 *Phantoms*

The Shepp-Logan phantom is used in the first series of experiments. It consists of a well-described pattern of ellipses and gray values, see Fig. 7.1a.

In the second series of experiments a foam phantom is used which is obtained from experimental micro-CT data, see Fig. 7.1b. The original cone beam dataset was obtained by a Skyscan 1172 with 511 projection angles. The reconstructed foam is a 3D object of consisting of 524 2D slices of  $1000 \times 1000$  pixels. A slice close to the center of the foam is used as the phantom for the experiments. Different slices from the 3D object are used as training examples for INN-FBP.

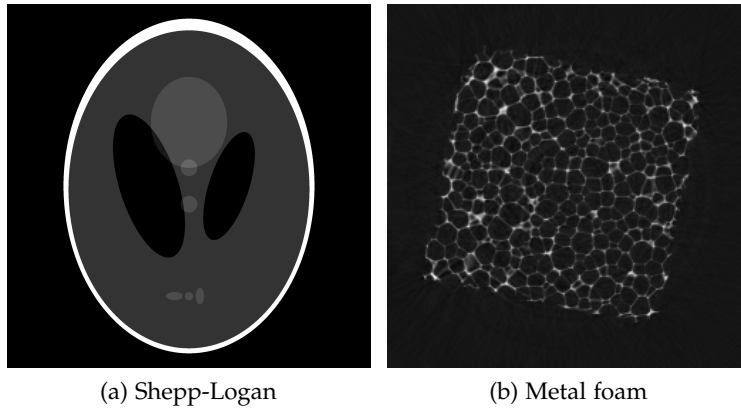


Figure 7.1: The phantoms.

### 7.3.2 Implementation details

The standard Ram-Lak filter for FBP is the windowed Ramp filter, where the window is the interval  $[-1, 1]$ . The same window is used for the Cosine and Hann filter, where some smoothing function is applied to Ram-Lak filter.

There are several implementation details to be discussed for the MR-FBP algorithm. The matrix  $W$  can be too large to obtain explicitly. Therefore, the matrix  $A_p = WW^T C_p$  is obtained column-by-column, where each column is obtained as the forward projection of applying FBP with unit vectors (with entries in  $\{0, 1\}$ ) as filters to the projection data  $p$ . Furthermore, exponential binning is used to reduce the number of unknowns for the filter  $h$ . Small bins are used around the center of the detector, and the size of the bins increases exponentially further away from this center. The filter is also assumed to be symmetric around this center, which decreases the number of unknowns even further. The direct method called `gels*` lapack routine is used to find  $h^*$  in Eq. (7.10).

For the AF-FBP method the algebraic reconstruction method SIRT with  $k = 100$  iterations and relaxation parameter  $\omega = 1$  is used to obtain the filters. The method SIRT itself is also included in the experimental results to give an idea of the reconstruction time and accuracy of an algebraic method.

For the method of Zeng there are two parameters to be chosen in advance. Zeng has empirically determined the value of the relaxation parameter  $\omega = 0.5$  for the filter function to be the optimal value. The number of iterations  $k$  of the Landweber algorithm is chosen to be  $k = 100$ .

The method OFBP is described for breast tomosynthesis. Since there are no limitations that prevent applying it to other geometries, we will apply it in this chapter to the parallel beam geometry. Instead of a thin rod we use a thin line placed vertically through the center of the detector as a 2D-phantom to calculate the filters. The thickness of the line equals the size of a detector pixel. Supersampling of 25 beams per detector pixel is used to obtain the projections. The number of iterations used for P-SIRT is  $k = 10$  and the relaxation parameter for P-SIRT is  $\omega = 1$ . It will become clear in the results section that  $k = 10$  is not always the optimal choice. We therefore also include some results with  $k = 100$ , which is the same number of iterations that is used for AF-FBP and Zeng, even though it is outside the scope of this work to determine (near) optimal parameters for every filter method.

The set of training objects for INN-FBP consists of 100 slightly altered Shepp-Logan phantoms, where either the direction of some ellipses, or the size or gray value is altered. Every image pixel of the training object can be used to train the neural network. Therefore, the size of the total training set is much higher than the number of training objects. The total training set and the validation set consist each of  $10^6$  different image pixels. We use the Levenberg-Marquardt algorithm to find the vectors  $\mathbf{q}_0^*$  and  $\hat{\mathbf{h}}_0^*$  that minimize the square differences between the output of the multilayer perceptron and the correct output. Furthermore, we use the Nguyen-Widrow initialization method to obtain start values for the parameters. Lastly, exponential binning is implemented to reduce the training time.

### 7.3.3 Geometry parameters

As mentioned before, a parallel beam scanning geometry has been used to obtain the projection data. The weight of each image projection for a specific projection is determined using the Joseph kernel. The number of projection angles  $N_\Theta$  varies between 8 and 64 and the projection angles are sampled equiangularly in the interval  $[0, 180)$  de-

grees. The number of counts on the detector  $I_0$  is varied from  $10^3$  (high noise level) to  $10^6$  (low noise level).

The projection data is downsampled to 256 bins and the phantoms are reconstructed on a square grid of  $256 \times 256$  pixels. The phantom is also downsamples to  $256 \times 256$  pixels and the reconstructions are compared with this downsampled phantom to avoid the inverse crime.

## 7.4 RESULTS

The results of the experiments will be presented in this section. We first give examples of filters for the different reconstruction methods. Then we compare the timings and we conclude this section with a comparison of the reconstruction qualities of the filtering methods.

### 7.4.1 Filters

The filters that are used in FBP vary per reconstruction method. They are all shown in Fig. 7.2 with  $|\Theta| = 24$ . If a filter is angle-dependent then the filter corresponding to an angle of 22.5 degrees is shown.

Note the difference in both the absolute values of the filter and in smoothing of the edge of the filter, which is mainly seen for FBP-Cos and FBP-Hann. Furthermore, we observe a local maximum between detector bins 1 and 50 in the experimentally determined filters MR-FBP, SIRT-FBP, OFBP and INN-FBP. This local maximum is not present in the theoretically derived filters FPB-RL, FBP-Cos, FBP-Hann and Zeng.

We also notice the small filter values for OFBP with 10 iterations, the number of iterations that was suggested by the inventors [8]. When we compare the reconstruction qualities of the different methods, then OFBP with  $k = 10$  is not competitive with the other methods. We therefore adjusted the number of iterations to  $k = 100$ , which is the same number of iterations as for SIRT-FBP and Zeng. The impact of this decision is shown in Fig. 7.3 and Fig. 7.4, where the filters with  $k = 10$  and  $k = 100$  are shown corresponding to an angle of 22.5 degrees, and two reconstructions of the metal foam phantom are shown with  $I_0 = 10^3$  and  $|\Theta| = 64$ . Also note the resemblance of the filters between OFBP with  $k = 100$  and SIRT-FBP with  $k = 100$ . Since the filters for  $k = 100$  substantially improve the results of OFBP, we have decided to show

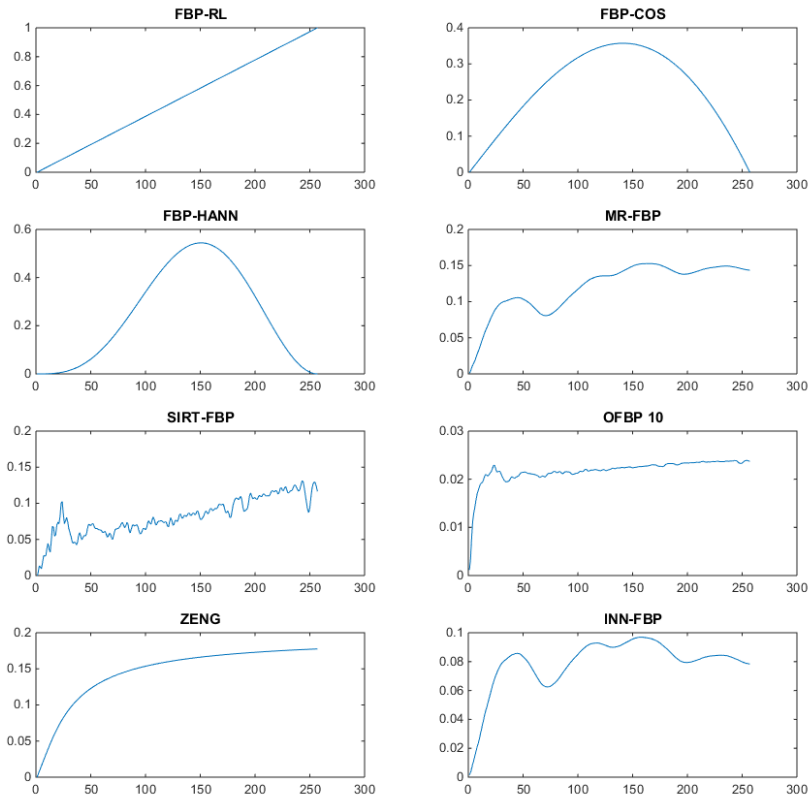


Figure 7.2: Filters for FBP with  $|\Theta| = 24$ . The Shepp-Logan phantom is used for the MR-FBP filter calculation and for the training set for INN-FBP.

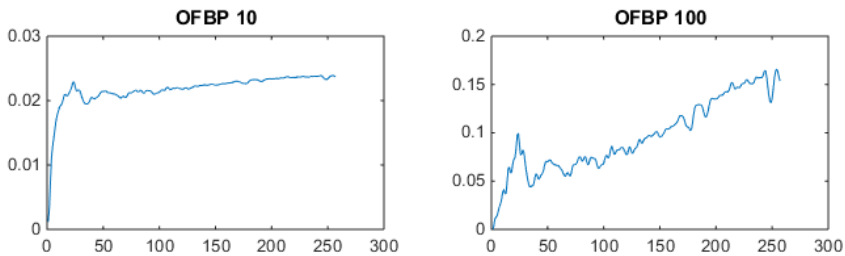


Figure 7.3: Filters for FBP with  $|\Theta| = 24$  with  $k = 10$  and  $k = 100$ , respectively.



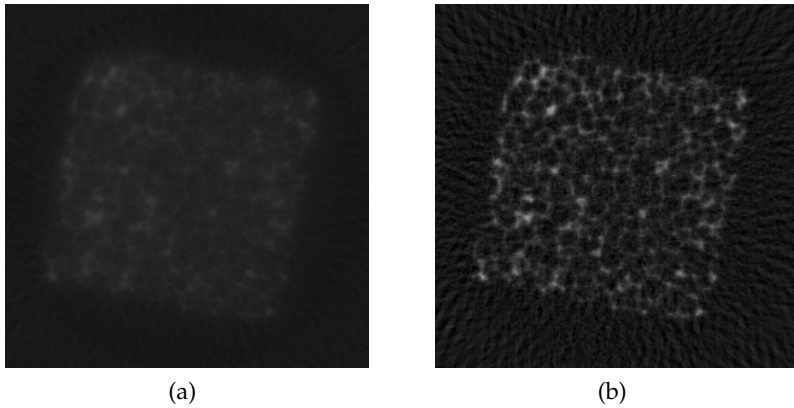


Figure 7.4: Reconstructions of the metal foam phantom with  $|\Theta| = 64$  and  $I_0 = 10^3$  for OFBP with (a)  $k = 10$ , (b)  $k = 100$ .

Method	FBP-RL	FBP-Cos	FBP-Hann	MR-FBP	AF-FBP	Zeng	OFBP	INN-FBP
PREP (s), $N_\Theta = 8$	$< 10^{-5}$	$< 10^{-5}$	$< 10^{-5}$	$1.8^* 10^{-3}$	55	$1.2^* 10^{-4}$	$2.8^* 10^{-1}$	300
PREP (s), $N_\Theta = 64$	$< 10^{-5}$	$< 10^{-5}$	$< 10^{-5}$	$2.2^* 10^{-3}$	775	$1.3^* 10^{-4}$	$8.3^* 10^{-1}$	295
REC ( $*10^{-3}$ s), $N_\Theta = 8$	2.3	2.3	2.3	25	2.3	2.3	2.3	2.9
REC ( $*10^{-3}$ s), $N_\Theta = 64$	3.6	3.7	3.7	43	3.7	3.7	3.7	4.3

Table 7.2: Preprocessing time (PREP) and reconstruction time (REC) for both  $N_\Theta = 8$  and  $N_\Theta = 64$  using the Shepp-Logan phantom with  $I_0 = 5 * 10^3$ .

results for OFBP with  $k = 100$  in the remainder of this chapter, for reasons of better comparison. It is, however, not in any way the purpose of this work to find optimal parameters for the different reconstruction methods. We therefore use the parameters that are suggested by their inventors for the other reconstruction methods.

#### 7.4.2 Timings

The time that is required to produce a reconstruction is split into the preprocessing time and the actual reconstruction time, see Section 7.2.8.

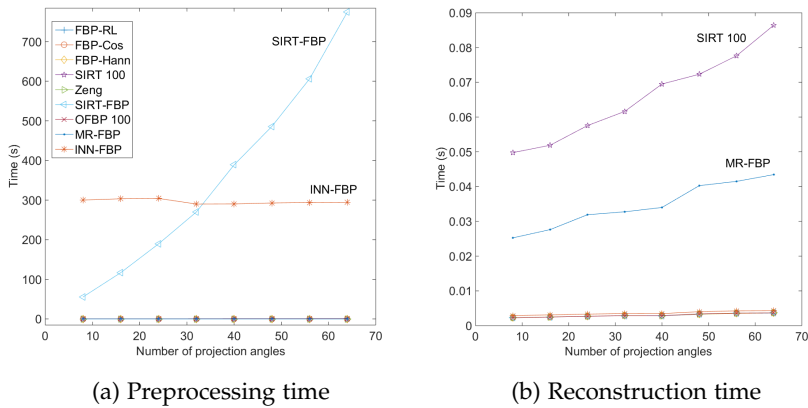


Figure 7.5: Timings required to reconstruct the Shepp-Logan phantom.

The preprocessing times and reconstruction times for the different reconstruction methods are shown in Fig. 7.5 and Table 7.2 for  $N_{\Theta} = 8$  and  $N_{\Theta} = 64$  where  $I_0 = 5 * 10^3$ . The phantom to be reconstructed was the Shepp-Logan phantom.

We observe that the preparation time of INN-FBP is substantial but does not increase with increasing number of projection angles. The time that is required to obtain a filter for SIRT-FBP increases linearly with the number of projection angles. The actual reconstruction time for these methods is comparable to that of FBP with standard filters, since no additional calculations need to be done after the filters have been created for a given geometry. In contrast to these methods, MR-FBP needs no preprocessing time, while the reconstruction time is substantially higher and increases with the number of projection angles. We have included the reconstruction time that is required for SIRT with  $k = 100$  iterations for comparison.

We also observe a slightly larger reconstruction time for INN-FBP compared to for example FBP with standard filters. The difference is small though, and is due to a slightly different implementation.

### 7.4.3 Number of projection angles

In this series of experiments, we vary the number of projection angles and show the resulting MSE and SSIM for a fixed amount of noise

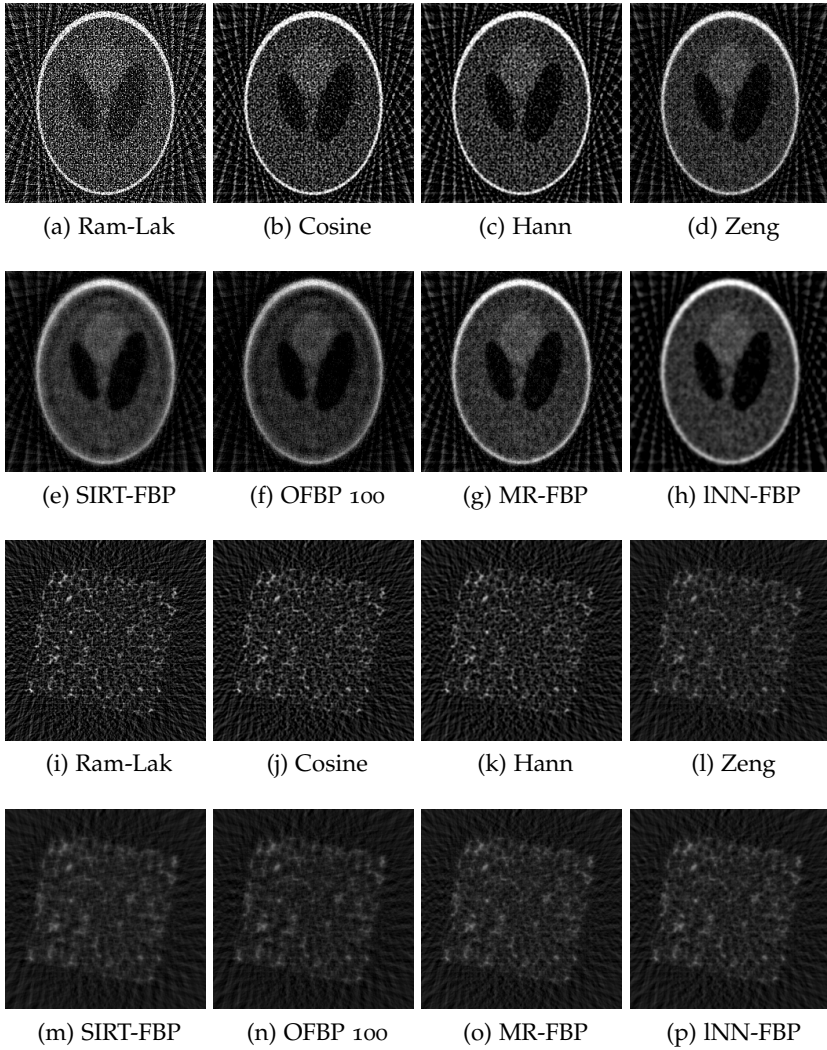


Figure 7.6: Reconstructions of (a)-(h) the Shepp-Logan phantom,  $I_0 = 10^3$ ,  $|\Theta| = 24$ , (i)-(p) the metal foam phantom,  $I_0 = 10^4$ ,  $|\Theta| = 32$ .

applied to the projection data. We first show some reconstructions in Fig. 7.6 of the Shepp-Logan phantom for  $I_0 = 10^3$  and  $|\Theta| = 24$ , and of the metal foam for  $I_0 = 10^4$  and  $|\Theta| = 32$ . The results for both the Shepp-Logan phantom and the metal foam phantom with  $I_0 = 10^3$  are shown in Fig. 7.7.

We observe that the differences in performance with this high noise level are large for both the MSE and SSIM measure. For few projection angles, FBP with standard filters and the method of Zeng are clearly outperformed by the other methods. FBP with the Ram-Lak filter performs worst with respect to both measures for all considered projection data. For a larger number of projection angles, the differences in reconstruction quality become smaller.

The reconstruction methods INN-FBP, SIRT-FBP, SIRT and OFBP perform similarly with respect to both the MSE and SSIM, where we note that INN-FBP is slightly better than the other methods. The exception is the SSIM for the Shepp-Logan phantom, where INN-FBP is substantially more accurate than all other filter methods. Furthermore, we observe that the reconstruction quality of SIRT-FBP and SIRT is comparable, and that it is slightly better than OFBP with respect to the MSE. For a sufficiently large number of projection angles, the SSIM of OFBP is larger than that of SIRT-FBP.

The reconstruction quality of MR-FBP for low numbers of projection angles is relatively high compared to the other methods, while for higher numbers of projection angles MR-FBP performs relatively poorly.

#### 7.4.4 Poisson noise

For the second series of experiments, we vary the amount of Poisson noise for a fixed number of projection angles. Again we observe that the reconstruction quality strongly depends on the chosen parameters, the phantom that is used and on the number of projection angles. This is demonstrated in Fig. 7.8, where the MSE and SSIM are shown for reconstructions of the Shepp-Logan phantom and the metal foam phantom for both  $|\Theta| = 16$  and  $|\Theta| = 64$ .

For few projection angles, the standard filters Ram-Lak, Cosine and Hann are outperformed by the other methods. Also Zeng cannot compete with the other filter methods for the metal foam phantom. For the Shepp-Logan phantom, however, the method of Zeng is a strong

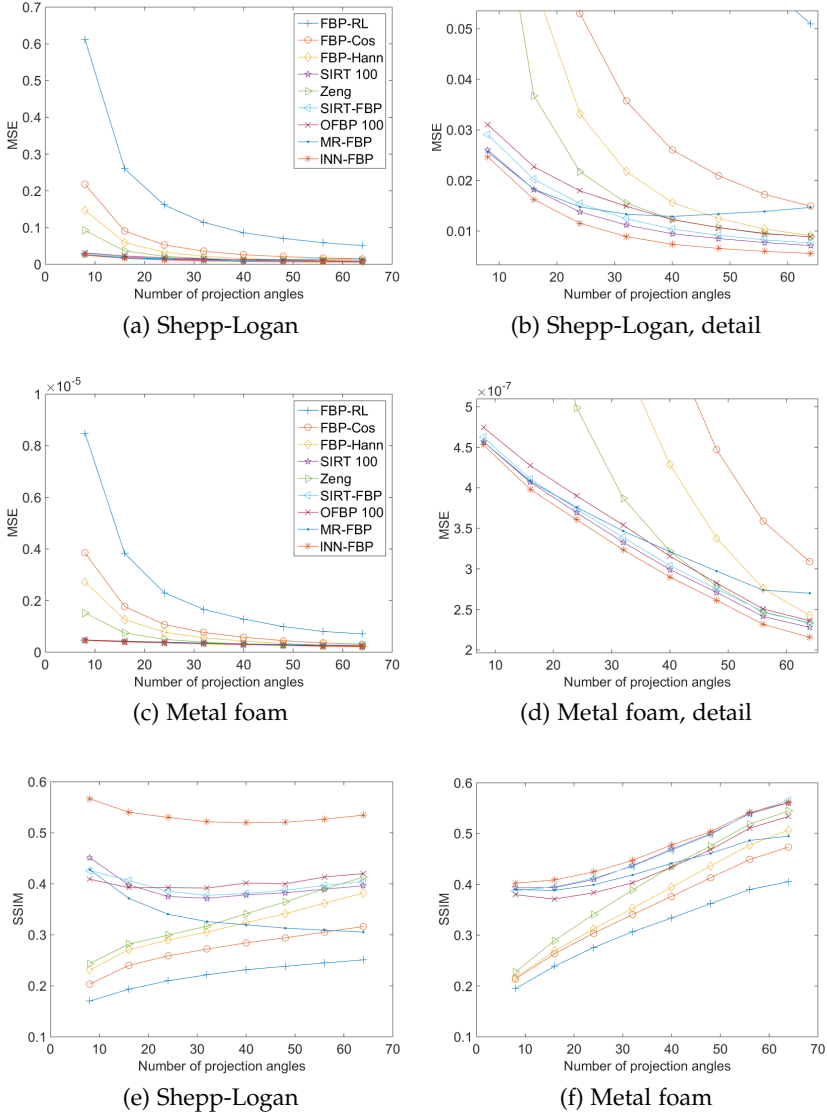
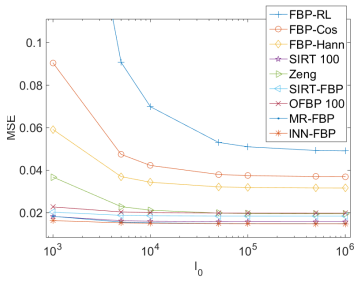
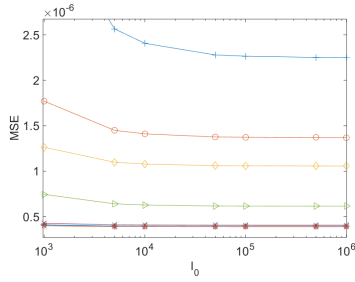


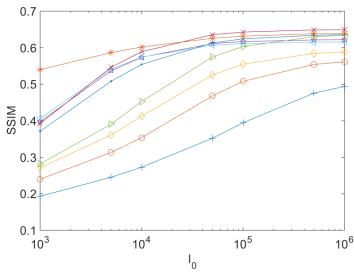
Figure 7.7: Mean square error and structural similarity index measure with  $I_0 = 10^3$ .



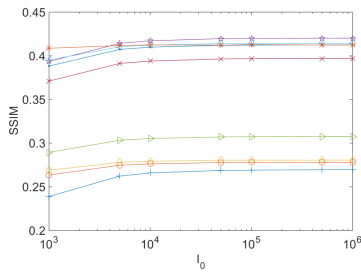
(a) Shepp-Logan,  $|\Theta| = 16$



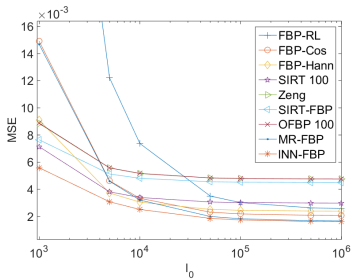
(b) Metal foam,  $|\Theta| = 16$



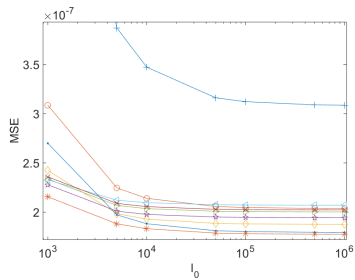
(c) Shepp-Logan,  $|\Theta| = 16$



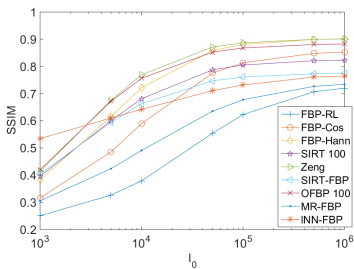
(d) Metal foam,  $|\Theta| = 16$



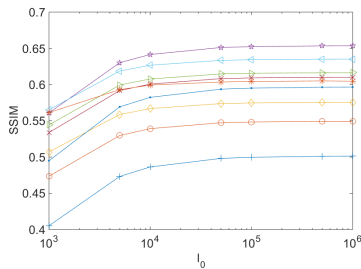
(e) Shepp-Logan,  $|\Theta| = 64$



(f) Metal foam,  $|\Theta| = 64$



(g) Shepp-Logan,  $|\Theta| = 64$



(h) Metal foam,  $|\Theta| = 64$

Figure 7.8: Quality of the reconstructions using the MSE and SSIM.

competitor for the other methods. The ranking of these methods also depends on the measure; for MSE the method INN-FBP performs best for both phantoms, while for SSIM the outcome does not only depend on the phantom, it also depends on the amount of noise that is applied to the projection data. The methods INN-FBP, OFBP and SIRT all perform best for a specific combination of these influencing factors.

The results also depend heavily on the number of projection angles. For the high number of projections  $|\Theta| = 64$ , we observe that INN-FBP performs very well with respect to the MSE, while the SSIM of INN-FBP varies from the best to below average compared to the other methods. The opposite is seen for SIRT-FBP, OFBP and Zeng, where for example the MSE of SIRT-FBP is large for low noise levels, while the SSIM varies from the best to average depending on the phantom that is reconstructed. The method MR-FBP performs well with respect to the MSE for low noise levels, while it ranges from poorly to average for the SSIM.

## 7.5 DISCUSSION AND CONCLUSIONS

The scientific research of the last decade that had aimed at improving filters for FBP has resulted in several new filtering methods. In this chapter we presented an overview of these algorithms and compared their characteristics. We have also shown some reconstruction results for two different phantoms.

Since the reconstruction methods have very different characteristics, the choice for a specific reconstruction method depends on many factors. Time constraints are often an important factor in this decision; in this work both the preprocessing time and the reconstruction time are considered during the experiments. Furthermore, the number of projection angles and the amount of noise have a large impact on the quality of the reconstructions. Some filtering methods are better at handling few projection angles and high noise levels than others. Another factor that can play a role in the choice for a specific reconstruction method is the ability to incorporate prior knowledge.

The reconstruction methods INN-FBP and AF-FBP require a large amount of preprocessing time and are therefore only suitable if the filters can be repeatedly used in a large number of experiments. The method OFBP also requires some preprocessing time, but this is small com-

pared to AF-FBP. The method MR-FBP requires a large reconstruction time, since it calculates a filter for every reconstruction based on the measured projections. Therefore this method is less favorable if large numbers of objects need to be scanned. The theoretically derived filters Ram-Lak, Cosine, Hann and Zeng require no preprocessing time and only a very short reconstruction time.

When not the reconstruction time but the ability to handle noise and few projection angles is the highest contributing factor to the choice for a reconstruction method, then the decision which method is best is less straightforward. We have shown that the reconstruction quality of the various methods depends highly on the number of projection angles and the amount of noise that is applied to the projection data. The suitability of the different methods varies with the phantom that is used. Furthermore, the outcome of comparing the reconstruction qualities depends on the choice of the measure. For the combination of geometry and phantoms we have considered here, the method INN-FBP performs in most situations for both measures very well, while Ram-Lak, Cosine, Hann and Zeng cannot handle few projection angles and high noise levels well. The relative reconstruction qualities of the methods AF-FBP, MR-FBP and OFBP vary too much per phantom and geometry to draw any conclusions on which one performs best.

The ability to incorporate some types of prior knowledge is not examined in this chapter. Neither did we attempt to optimize the parameters of the reconstruction methods, such as the number of iterations  $k$  or the relaxation parameter  $\omega$ . We have used the values suggested by their inventors, with the exception of OFBP since its reconstruction quality was otherwise not competitive with respect to the other filtering methods. Optimizing the parameters is outside the scope of this work.

Furthermore, we have deliberately refrained ourselves from any attempt to explain the observations in the Results section. Instead, we have limited our comments to a description of the behavior of the filtering methods. Since the aim of this chapter is to give an overview of the different filtering methods and their characteristics, the Results section is merely an illustration of the preceding theory. It requires further research with an increased number of phantoms and varying scanning geometries to be able to recommend filtering methods for specific reconstruction settings.



## BIBLIOGRAPHY

- [1] S. Van Aert et al. Three-dimensional atomic imaging of crystalline nanoparticles. *Nature* 2011; 470(7334): 374–377.
- [2] T. M. Buzug. *Computed Tomography: From Photon Statistics to Modern Cone-Beam CT*. Berlin: Springer, 2008.
- [3] H. Sipila. Moving object computer-tomography for luggage inspection. *Applications of Signal and Image Processing in Explosives Detection Systems*. Ed. by M. C. Connelly and S. M. Cheung. Proc. SPIE, 1993; 1824: 39–40.
- [4] G. Nolet. *Seismic Tomography: With Applications in Global Seismology and Exploration Geophysics*. Dordrecht: Springer Netherlands, 1987.
- [5] G. T. Herman. *Fundamentals of Computerized Tomography: Image Reconstruction from Projections*. Berlin: Springer, 2009.
- [6] F. Natterer. *Mathematical methods in image reconstruction*. Philadelphia: SIAM, 2001.
- [7] G. L. Zeng. A filtered backprojection algorithm with characteristics of the iterative Landweber algorithm. *Med. Phys.* 2012; 39(2): 603–607.
- [8] H. Kunze et al. Filter determination for Tomosynthesis aided by iterative reconstruction techniques. *Proc. of Fully3D* 2007: 309–312.
- [9] K. J. Batenburg and L. Plantagie. Fast Approximation of Algebraic Reconstruction Methods for Tomography. *IEEE Trans. Image Process.* 2012; 21(8): 3648–3658.
- [10] D. M. Pelt and K. J. Batenburg. Fast tomographic reconstruction from limited data using artificial neural networks. *IEEE Trans. Image Process.* 2013; 22(12): 5238–5251.
- [11] D. M. Pelt and K. J. Batenburg. Improving Filtered Backprojection Reconstruction by Data-Dependent Filtering. *IEEE Trans. Image Process.* 2014; 23(11): 4750–4762.
- [12] D. J. Godfrey, H. P. McAdams, and J. T. Dobbins 3rd. Optimization of the matrix inversion tomosynthesis (MITS) impulse response and modulation transfer function characteristics for chest imaging. *Med Phys.* 2006; 33(3): 655–667.

- [13] T. Nielsen et al. Filter Calculation for X-Ray Tomosynthesis Reconstruction. *Phys. Med. Biol* 2012; 57(12): 3915–3930.
- [14] A.C. Kak and M. Slaney. *Principles of Computerized Tomographic Imaging*. Philadelphia: SIAM, 2001.

---

## SAMENVATTING

---

### ACHTERGROND

*Computed tomography* (CT) is een techniek in de beeldvorming waarbij met behulp van wiskunde een afbeelding wordt gemaakt van het inwendige van een object zonder het open te maken. De term tomography is afgeleid van het Griekse tomos (snede). Er zijn vele toepassingen voor CT, waarbij de bekendste de medische beeldvorming is. Bij CT-scans in ziekenhuizen stuurt men röntgenstraling door het menselijk lichaam om dwarsdoorsnedes zichtbaar te maken. Naast medische toepassingen kent CT ook vele industriële toepassingen. Zo wordt er bijvoorbeeld op hele kleine schaal (nanometers) naar materialen gekeken met behulp van een elektronenmicroscop, en wordt er op hele grote schaal (kilometers) onderzoek gedaan naar structuren in de bodem bij seismische tomografie. Ook wordt computed tomography gebruikt bij materiaalkunde, bijvoorbeeld bij de inspectie van turbinebladen, waarbij wordt onderzocht of een voorwerp scheuren of andere onregelmatigheden bevat.

Bij computed tomography worden stralen door een object gestuurd en aan de andere zijde opgevangen door een detector. Deze detector meet de intensiteit van de stralen en verzamelt zo informatie over de hoeveelheid straling die onderweg verloren is gegaan. Door genoeg stralen onder verschillende hoeken door het object te sturen, wordt voldoende informatie verzameld om de dwarsdoorsnedes van het object te benaderen of zelfs exact te berekenen. Deze dwarsdoorsnedes kunnen als afbeelding worden weergegeven door de hoeveelheid geabsorbeerde straling om te zetten in grijswaarden. Doordat twee verschillende materialen van dezelfde dikte in het algemeen ongelijke hoeveelheden straling absorberen, kunnen de materialen waaruit het object bestaat worden onderscheiden op basis van hun grijswaarden. Zo zijn organen te onderscheiden bij een CT-scan in het ziekenhuis, en zijn bijvoorbeeld scheuren zichtbaar bij materiaalkundig onderzoek.

Een veelgebruikte term voor het resultaat van CT is een *reconstructie*. Hoewel er idealiter een exacte reconstructie wordt gemaakt, accepteert

men vaak een benadering om zo bijvoorbeeld de stralenbelasting of de benodigde rekentijd te verminderen. Daarnaast is een exacte reconstructie in veel gevallen niet mogelijk omdat een reconstructie wordt weergegeven op een raster bestaande uit pixels, vergelijkbaar met de pixels van een digitale fotocamera, terwijl de meeste objecten die worden gescand niet exact op zo'n raster kunnen worden weergegeven. Een voorbeeld hiervan is een object met gebogen lijnen. Ook zitten er vaak kleine verstoringen in de gemeten waarden op de detector en kunnen stralen onderweg worden afgebogen, ook wel *ruis* respectievelijk *verstrooiing* genoemd, waardoor de reconstructie niet exact overeenkomt met het gescande object. Hoe meer de reconstructie overeenkomt met het gescande object, hoe hoger de kwaliteit van de reconstructie is.

#### RECONSTRUCTIEMETHODEN

Er wordt veel onderzoek gedaan naar de meest optimale technieken voor het berekenen van een reconstructie, zodat de reconstructie het object zo goed mogelijk benadert. Hierbij zijn er twee hoofdrichtingen te onderscheiden. De eerste hoofdrichting maakt gebruik van een inversieformule via een analytische benadering met continue variabelen. Deze formule bevat een filter wat wordt toegepast op de data die met de detector is verzameld, de *input data* genoemd. Deze methode heet dan ook *Filtered Backprojection* (FBP). Deze methode levert een benadering op van het object en de kwaliteit van de reconstructie hangt sterk af van het gebruikte filter, het aantal hoeken waaronder gescand is, en de hoeveelheid ruis op de input data. Het grootste voordeel van deze methode is de korte tijd die nodig is om de reconstructie te berekenen. Een bekend nadeel van deze methode is de gevoeligheid voor ruis op de input data waardoor de kwaliteit van de reconstructie snel achteruit gaat als de ruis toeneemt. Daarnaast moeten de gebruikte hoeken bij het scannen gelijkmatig verdeeld zijn over  $180^\circ$  of  $360^\circ$ . In de praktijk is het soms niet mogelijk om  $180^\circ$  rond het object te kunnen draaien, bijvoorbeeld bij elektronenmicroscopie. Hier zit het object in een houder die rond kan draaien, waarbij de bron en detector stil staan. In deze gevallen met een beperkt hoekbereik zijn reconstructies met FBP onnauwkeurig.

De tweede hoofdrichting benadert het reconstructieprobleem als een stelsel vergelijkingen. Hierbij wordt al direct uitgegaan van een discrete situatie waarbij het object wordt gezien als een raster met onbekende grijswaarden. Deze methodes worden *algebraïsche reconstructiemethodes* (ARMs) genoemd. Vaak wordt de reconstructie berekend door een vast stappenplan meerdere keren (cycli) te doorlopen waarbij het resultaat van iedere cyclus steeds een (tussentijdse) reconstructie is. Door meerdere cycli uit te voeren wordt de reconstructie steeds aangepast met als doel om de kwaliteit van de reconstructie te verbeteren. Zo wordt bijvoorbeeld na iedere cyclus berekend wat de input data zou zijn geweest als de tussentijdse reconstructie zou zijn gescand. Deze fictieve data wordt vergeleken met de werkelijk gescande data. Het verschil tussen beide datasets wordt in de volgende cyclus gebruikt om de reconstructie te verbeteren. Dit noemen we een *iteratieve* methode. Dit proces kost vaak substantieel meer rekentijd dan FBP, wat tot problemen leidt wanneer er veel objecten in korte tijd worden gescand en de rekentijd groter is dan de tijd die nodig is om te scannen. Er ontstaat een wachttijd voordat de input data kan worden verwerkt, waardoor veel geheugen nodig is om deze datasets tijdelijk op te slaan. Grote voordelen van deze methode zijn de relatieve ongevoeligheid voor ruis op de input data, en de mogelijkheid om met een beperkt hoekbereik van de projecties relatief goede reconstructies te berekenen. Daarnaast kan al bekende informatie over het object worden meegenomen in de berekeningen. Een voorbeeld hiervan is als bij materiaalkundig onderzoek een object uit één of enkele materialen bestaat met bekende grijswaarden. Deze vooraf bekende informatie kan de kwaliteit van de reconstructie sterk positief beïnvloeden.

#### ALGEBRAÏSCHE FILTERS

Vanwege zijn relatief korte rekentijd is FBP een frequent gebruikte reconstructiemethode bij CT. Door de hierboven beschreven nadelen is FBP echter niet in alle situaties een geschikte methode om te gebruiken en wordt er gekozen voor een tragere ARM. Aangezien de kwaliteit van de reconstructies van FBP wordt beïnvloed door de keuze van het filter, is er al veel onderzoek gedaan om nieuwe filters te ontwikkelen die betere reconstructies opleveren. Bij aanvang van dit promotietraject is er echter nog weinig werk bekend waarin ARMs als

basis worden gebruikt om filters te creëren voor FBP. In dit proefschrift wordt een nieuwe methode gepresenteerd om zulke filters te berekenen, *Algebraic filters - Filtered Backprojection* (AF-FBP) genaamd. Met deze methode wordt, voor een van tevoren vastgesteld scanprotocol met onder andere het aantal projectiehoeken, de grootte van de detector en specificaties voor de bron, eenmalig een filter berekend op basis van informatie van een (aanvankelijk lineaire) ARM. Het zo verkregen filter wordt vervolgens toegepast in FBP. Deze AF-FBP reconstructies zijn een benadering van de reconstructies van de ARM die is gebruikt om het filter te berekenen. Het filter is niet afhankelijk van het object en kan dus hergebruikt worden bij verschillende objecten zolang hetzelfde scanprotocol wordt gebruikt. AF-FBP is dus een methode met de rekensnelheid van FBP die bij benadering reconstructies oplevert met dezelfde eigenschappen als de reconstructies van de corresponderende ARM.

Bij de berekening van het filter voor AF-FBP wordt specifiek het pixel gebruikt dat centraal in het reconstructiegebied ligt. In dit proefschrift is aangetoond dat de kwaliteit van een reconstructie afhankelijk is van onder andere de plaats van het object in het reconstructiegebied. Daarom is ook de toegevoegde waarde van het gebruik van meerdere pixels onderzocht voor de berekening van de filters. Hieruit blijkt dat het gebruik van negen filters voor subgebieden van het reconstructiegebied geen verbetering van de kwaliteit van de reconstructies oplevert. Wel is het zinvol gebleken om bij de berekening van het filter de zijden van het reconstructiegebied groter te kiezen dan de lengte van de detector, om zo het effect van randartefacten op het filter, en daarmee op de reconstructies, te reduceren.

De methode AF-FBP maakt gebruik van de lineariteit van een ARM, en is in zijn huidige vorm niet geschikt om toe te passen op niet-lineaire ARMs. Indien er echter objecten worden gebruikt die naar verwachting slechts kleine variaties zijn op een bekende blauwdruk, kan AF-FBP worden aangepast zodat deze ook voor een subklasse van de niet-lineaire ARMs toepasbaar is. Bij kleine variaties op een blauwdruk is ook het verschil in input data tussen het gescande object en de blauwdruk gering. De niet-lineaire ARMs waarvoor een aangepaste AF-FBP is ontwikkeld, kunnen gesplitst worden in een niet-lineaire transformatie op de input data van de blauwdruk, en een lineaire transformatie op het verschil in input data van de blauwdruk en het gescande object. Ze worden daarom in dit proefschrift aange-

duid als *lokaal* lineaire ARMs. AF-FBP kan zo worden aangepast dat deze wordt toegepast op dit verschil in input data en dus een reconstructie oplevert van dit verschil. Het resterende onderdeel van de reconstructie, namelijk de niet-lineaire transformatie van de input data van de blauwdruk, hoeft slechts eenmalig berekend te worden voor de gegeven blauwdruk. Voor alle variaties op de blauwdruk kan deze uitkomst worden overgenomen zonder deze opnieuw te berekenen. Hiermee kan ook voor deze lokaal lineaire ARMs met korte rekentijd een reconstructie worden berekend die de reconstructie van de corresponderende lokaal lineaire ARM benadert.

Dit proefschrift sluit af met een overzicht van de eigenschappen van verschillende recent ontwikkelde methoden om filters te creëren voor FBP. Hieruit blijkt dat de keuze voor een filter in belangrijke mate wordt bepaald door de tijd die beschikbaar is voor de berekeningen, het aantal hoeken waaronder gescand kan worden, en de hoeveelheid te verwachten ruis op de input data. Aangezien AF-FBP aanzienlijk meer tijd nodig heeft om de filters te berekenen, deze filters onafhankelijk zijn van het gescande object, en afhankelijk zijn van de scanprocedure, is deze methode met name geschikt wanneer een beperkt aantal scanprocedures wordt gebruikt. De prestaties van de verschillende filters onderling zijn erg afhankelijk van de gescande objecten, de gekozen scanprocedure, en de maatstaf die gebruikt wordt om de kwaliteit van een reconstructie te bepalen. Voor een meerderheid van de onderzochte gevallen is de kwaliteit van de reconstructies van AF-FBP bovengemiddeld vergeleken met die van de andere filters.





---

## CURRICULUM VITAE

---

Linda Plantagie was born in Nieuwegein on August 19, 1986. She attended the Christelijk Lyceum Zeist from 1998 until 2004, where she completed a gymnasium education. From 2004 she studied both Mathematics and Physics, followed by the master Mathematical Sciences at Utrecht University. She obtained both Bachelors of Science with honors in 2007 and the Master of Science with honors in 2009. For the master's degree she wrote a thesis entitled 'Minimizing the waiting time in a large-scale network of an advanced planning system' under the supervision of Prof. dr. R. H. Bisseling (Utrecht University) and dr. S. van Dijk (ORTEC).

In 2009, she started her PhD research at the Centrum Wiskunde & Informatica (CWI) under the supervision of Prof. dr. K. J. Batenburg (Leiden University). She presented her work at conferences in Salt Lake City and New York City. From 2012, she has been studying Medicine at Utrecht University parallel to her PhD research. She obtained her bachelor's degree in 2015 and subsequently started the master's program.



---

## ACKNOWLEDGEMENT

---

Foremost, I would like to express my gratitude towards my promotor Prof. dr. Kees Joost Batenburg, who has guided and supported me even after I started studying Medicine concurrently. His flexibility enabled me to complete my research.

Furthermore, I would like to thank my (former) colleagues at CWI. I have met too many people at the office to thank everyone individually here. I will remember the pleasant conversations over a nice cup of tea (or coffee), concerning life and work, with Xiaodong Zhuge, Bram van Es, Margreet Nool, Christoph Köhn and my office mates Marjon Ruijter, Folkert Bleichrodt, Wagner Fortis, and Svetlana Dubinkina. I also wish to acknowledge Daan Pelt for his contribution to Chapter 7. I also thank Rob Bisseling for his supervision and advice during my Master thesis, which ultimately led to this PhD position. I am very grateful to Willem Jan Palenstijn, on whom I could always rely when suffering computer problems (Astra, Matlab, Windows, Linux, network related, ...), who read and commented on some of my papers, and with whom I could always talk.

I also thank my superiors at CWI, Barry Koren, Kees Oosterlee, and Daan Crommelin, for giving me the opportunity to perform my research at CWI. The staff of CWI contributed significantly to the positive working atmosphere at the office. In particular, I would like to thank Nada Mitrovic, Duda Tepsic, Maarten Dijkema and Léon Ouwerkerk for their support.

I am grateful for the valuable comments I received from Jan Sijbers on some of my papers. I also thank him for the opportunity to visit the Vision Lab in Antwerp for several weeks during my PhD to intensify our collaboration.

I could not have completed this PhD without the support of my friends. In no particular order, Mischa, Stefan, Rob, Janneke, Ziv, Keith, Miriam, Lisanne, and Christiaan, each of you contributed in your own way to my success. I thank you for our conversations, mostly over dinner, for our laughing and sometimes crying, for your patience when

trying to find a date to get together, and for your never-ending belief in me completing my PhD. It meant the world to me.

Finally, I am indebted to my brother Thijs and my parents Angenieta and Wim for their love and unconditional support. I could not have completed my thesis without you. Also, you gave me the courage to pursue my dream of becoming a physician.

Linda Plantagie